EES Batteries

REVIEW

View Article Online
View Journal

Cite this: DOI: 10.1039/d5eb00220f

Research progress on molybdenum- and tungsten-based materials for sodium-ion batteries: fundamental mechanisms and optimization strategies

Bingrong Shen,[a] Chenhui Yan,[a] Hui Peng, *[a] Guofu Ma [a] and Yuxi Xu *[b]

Received 19th November 2025,
Accepted 2nd February 2026

DOI: 10.1039/d5eb00220f

rsc.li/EESBatteries

In sodium-ion battery (SIB) anode systems, molybdenum (Mo)- and tungsten (W)-based materials have shown great potential in the field of energy storage due to their high theoretical capacity, adjustable layered structure, and multi-electron characteristics. However, their practical applications are limited by challenges such as structural collapse caused by volume expansion, instability of the solid electrolyte interface (SEI) due to interface side reactions, and poor conductivity. To date, many reports have shown that through strategies such as structural design, compounding and hybridization, defect and interface engineering, their conductivity can be significantly improved, mechanical stress alleviated and ion transport paths optimized, achieving a breakthrough in cycling stability. In this review, we first analyze the challenges faced by Mo- and W-based materials in SIB anodes. Then, we systematically focus on the sodium storage mechanisms and performance optimization strategies for Mo- and W-based materials, as well as research progress on Mo- and W-based oxides/chalcogenides, carbon composites and polymetallic molybdenum/tungstate. Finally, we discuss the bottlenecks they face and provide an outlook for the future development of Mo- and W-based materials in the SIB field.

Broader context

With growing demand for sustainable energy storage, sodium-ion batteries (SIBs) are emerging as a promising alternative to lithium-ion batteries (LIBs) due to their abundant sodium resources, low cost, and environmental friendliness. However, the slow diffusion kinetics of Na^+ in traditional anode materials remains a major challenge limiting the development of high-performance SIBs. This is not only due to limitations of the anode material, but also closely related to its sodium storage capacity, structural stability, and interfacial dynamics. Molybdenum (Mo)- and tungsten (W)-based materials, with their unique layered structures and rich valence states, offer a high theoretical capacity, structural stability, and excellent rate performance in SIBs, demonstrating great application potential. Nevertheless, issues such as interfacial stability, volume effects, and conductivity still hinder their performance improvement. Therefore, improving the overall performance of SIBs requires some efficient and significant optimization strategies. Against this backdrop, we highlight the recent progress made in sodium storage mechanisms and optimization strategies for SIB anode materials. In addition, we also conducted an in-depth analysis of research progress on various Mo- and W-based materials. Therefore, continued progress in these directions is expected to accelerate the practical application of SIBs in next-generation energy storage applications.

1. Introduction

At a critical time in the global energy transition, efficient and low-cost energy storage technology has become a core element in supporting the large-scale deployment of renewable energy.[1,2] Although lithium-ion batteries (LIBs) dominate the current market, they face severe challenges due to the uneven distribution of lithium resources and sharp price fluctuations, which seriously restrict their application in the electrochemical energy storage area.[3,4] Sodium-ion batteries (SIBs) are widely regarded as an important representative of the next generation of energy storage systems due to the abundance of sodium resources in Earth's crust, low raw material costs, high intrinsic safety, outstanding fast charging capabilities, green sustainability, and a similar working mechanism to that of LIBs (Fig. 1).[5–7] However, the large radius and molar mass of sodium ions (Na^+) lead to sluggish diffusion kinetics in traditional anode materials, causing significant volume strain and capacity decay during charging and discharging, which

---

[a] Key Laboratory of Eco-functional Polymer Materials of the Ministry of Education, Key Laboratory of Polymer Materials of Gansu Province, College of Chemistry and Chemical Engineering, College of Engineering, Northwest Normal University, Lanzhou 730070, China. E-mail: penghui@nwnu.edu.cn
[b] School of Engineering, Westlake University, Hangzhou 310024, China. E-mail: xuyuxi@westlake.edu.cn

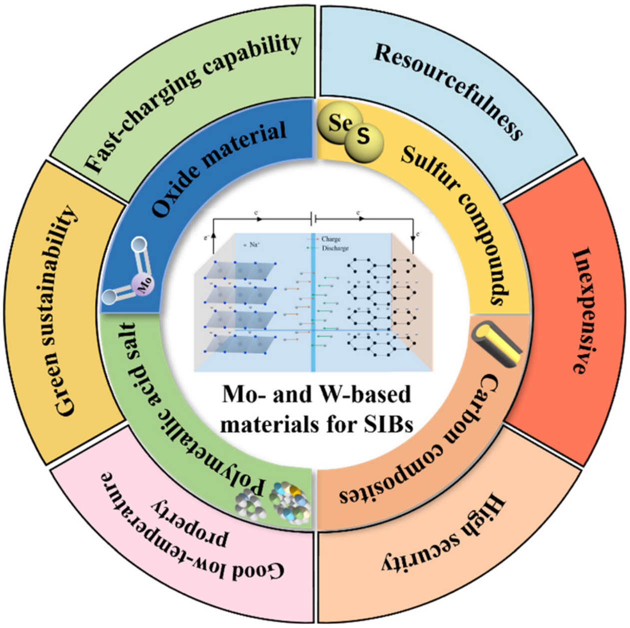

Fig. 1 Classifications and advantages of Mo- and W-based materials for SIBs.

has become the main bottleneck in the development of high-performance SIBs.[8–10]

As the core component of SIBs, the performance of anode materials directly affects the energy density, cycle life and rate capability of batteries.[11–13] The ideal anode needs to have a high specific capacity, excellent ionic/electronic conductivity and structural stability to achieve efficient and stable operation of the battery.[14–16] Although traditional hard carbon materials have a good cycling performance, their limited theoretical capacity makes it difficult to meet the needs of high energy density, and new materials are urgently needed to break through the performance bottleneck.[17–19] Among the many candidate materials, molybdenum (Mo)- and tungsten (W)-based materials stand out with their significant advantages and they have become the most promising candidate materials for anodes.[20–22] From the perspective of structural characteristics, Mo- and W-based materials mostly present a layered crystal structure with natural ion transport channels between layers, and their interlayer spacing can be flexibly controlled by means of intercalation and exfoliation.[23–25] Compared with other materials, this adjustable interlayer spacing not only provides a more suitable space for Na^+ insertion/de-insertion, effectively reducing the insertion energy barrier, but also buffers volume changes during charging and discharging, maintaining structural stability.[26–29] At the level of the Na^+ storage mechanism, the rich valence changes of Mo/W elements enable multiple redox reactions such as intercalation, conversion and alloying to occur, providing a high theoretical capacity, far exceeding that of traditional hard carbon anode materials (250–350 mAh g^{-1}).[30–33] In addition, Mo- and W-based materials also have good chemical stability and thermal stability, and can maintain their structural integrity under extreme conditions such as high temperature and high voltage, greatly improving the safety and environmental adaptability of the battery.[34–37] Meanwhile, its unique electronic structure endows the material with excellent intrinsic electronic conductivity, and the ion transport advantages brought by the layered structure can effectively improve the rate performance of the battery.[38–41] In 2025, Liu *et al.* thoroughly investigated the effect of W doping on the electrochemical performance of a manganese phosphate material with a NASICON structure (sodium superionic conductor type structure), analyzing the mechanism of W doping and proposing an optimization framework to improve its cycling stability and rate performance.[42] On the other hand, Khammuang *et al.* integrated the electrochemical mechanisms of Mo_2C, Mo_2CO_2, and MXenes through density functional theory (DFT) calculations, highlighting Na^+ adsorption, diffusion, and maximum capacity under different strains, and the Mo-based MXenes exhibited lower energy diffusion barriers and excellent dendrite suppression capabilities compared to existing materials.[43] These studies provide a theoretical basis for the performance optimization of Mo- and W-based materials and point the way for further improving the performance of SIBs. In recent years, research has focused on further unlocking the performance potential of Mo/W based materials through strategies such as nanostructure design and atomic-level regulation. By enhancing the exposure of active sites in materials and optimizing interfacial charge transfer efficiency, SIBs are being pushed toward the practical goal of high energy density and long cycle life.[44–47]

Mo- and W-based materials have shown multi-dimensional performance advantages and application potential in the field of SIB anodes, but there are still many technical difficulties to be overcome before large-scale commercial applications.[48–51] This review introduces research on Mo- and W-based materials in SIB anodes through the aspects of material classification, sodium storage mechanisms, performance optimization strategies, practical application challenges and future development directions, and provides a comprehensive overview and analysis of recent research strategies for high-performance SIB anode materials.[52–55] With continued in depth research and development, Mo- and W-based anode materials will become the core breakthrough to overcome the performance bottleneck of SIBs, help the global energy storage industry move toward a green, efficient, and sustainable direction, and inject new impetus into the energy transformation goals.[56–59]

2. Challenges of Mo- and W-based materials in SIB anodes

Mo-based materials have the advantages of high temperature stability, strong corrosion resistance, relatively excellent conductivity, good compatibility with carbon materials, and environmental protection and non-toxicity.[60,61] W-based materials have the advantages of high density, high strength, high hardness, high chemical stability, excellent thermal conductivity and good electrical conductivity.[62,63] However, both of them face multiple challenges when applied in SIB anodes: when storing sodium, multiple reactions such as intercalating–conversion–alloying will cause volume expansion, resulting in pulverization and shedding of electrode materials, structural instability, and shortened cycle life; although the intrinsic conductivity is better than some materials, the interlayer electron conduction resistance is large, and the conductivity is still lower than that of carbon-based materials; the abundant active sites on the surface react with the electrolyte to form an unstable SEI membrane, which continuously consumes sodium ions and electrolyte, exacerbating capacity decay and increased internal resistance.[64–66] The above features and challenges are described in Fig. 2.

Although both Mo-based and W-based materials show potential as anode materials for SIBs, significant differences exist between them that affect their performance. W has a higher atomic mass than Mo, leading to differences in specific capacity and mass energy density. At the atomic level, W-based materials generally exhibit higher theoretical capacity and energy density than Mo-based materials, but considering the actual material density, their volumetric efficiency is lower because the higher atomic mass of tungsten reduces the actual density of the material. Furthermore, due to stronger atomic bonds, W-based materials typically possess higher structural stability than Mo-based materials, which can mitigate volume expansion during cycling. However, this advantage often comes with higher synthesis complexity and higher material costs, making W-based materials less cost-effective than Mo-based materials for large-scale applications. When selecting the appropriate material for a specific application, the trade-offs between cost, capacity, and scalability are crucial, especially in balancing battery energy density and overall cost to enable the practical large-scale application of SIBs.[67,68]

2.1 Volume expansion and poor cycling stability

During the Na^+ insertion/de-insertion process, Mo- and W-based materials undergo significant volume changes. Taking MoS_2 as an example, because Na^+ has a relatively large radius, when it is intercalated into the layered structure of MoS_2, it will expand the interlayer distance and cause changes to the lattice parameters.[69] This volume expansion will cause serious damage to the crystal structure of the material. Upon charge and discharge cycling, the layered structure is gradually stretched and distorted, and even interlayer peeling occurs.[70] From a microscopic perspective, the bond lengths and bond angles between atoms will also change, causing the crystal structure of the material to gradually degenerate, which in turn affects the electrochemical properties of the material.[71] After multiple cycles, the layered structure of MoS_2 may transform into a disordered nanoparticle stacking structure, which will not only reduce the specific capacity of the material but also affect the diffusion path and kinetic process of Na^+.

Volume expansion will cause stress concentration inside the material. Since the expansion degree of different parts of the material may be different, stress gradients will form inside and between particles.[72] This stress concentration will accelerate the pulverization process of the material. When the stress exceeds the tolerance limit of materials, cracks will appear in the material. As the number of cycles increases, the cracks continue to expand, eventually causing the material to break into fine particles.[73] Taking WS_2 nanosheets as an example, during the sodification process, the stress distribution at the edges and inside of the nanosheets is uneven, and the edges are more susceptible to stress and curl and break. After the material is pulverized, the electrical contact between the active material and the current collector deteriorates, and electron transmission is hindered, resulting in increased internal resis-

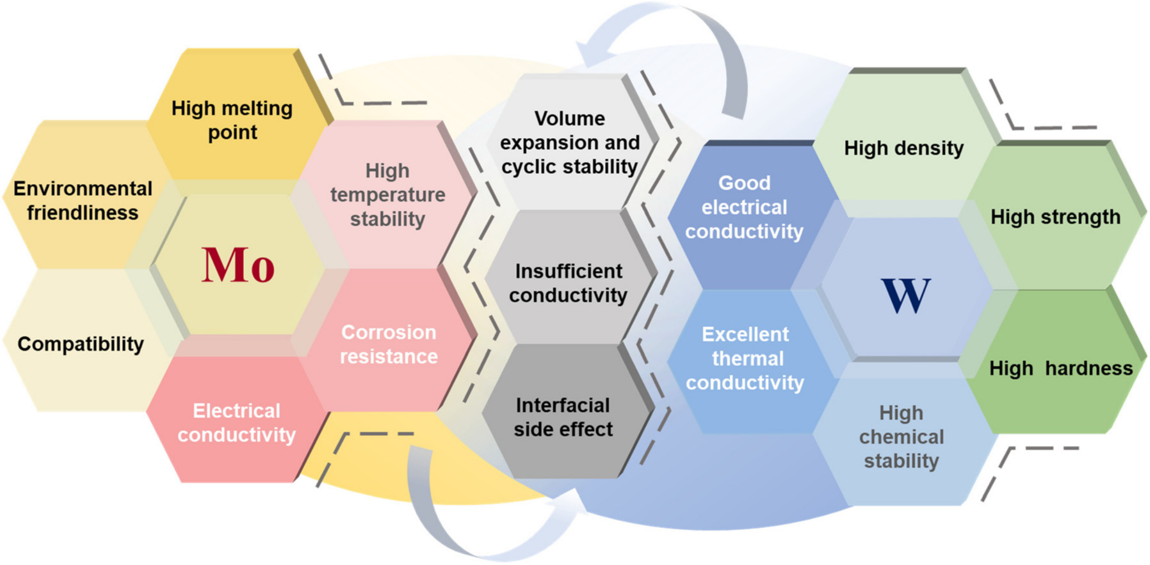

Fig. 2 Features and challenges of Mo- and W-based materials in SIB anodes.

tance of the battery and accelerated capacity decay. In addition, the pulverized particles may also fall off from the electrode surface, further reducing the active material loading of the electrode, seriously affecting the cycling stability and rate performance of the battery.[74]

Structural damage and pulverization will seriously weaken the cycling stability of the material. As the number of cycles increases, the structure of the material gradually deteriorates, resulting in the obstruction of Na^+ intercalation/deintercalation, reduced specific capacity, increased battery polarization, reduced energy efficiency, and even safety hazards.[75] The key to improving the cycling stability of Mo- and W-based materials lies in the synergy of "structural confinement" and "interface optimization", building physical support through nano-scaling and composite formation, combining doping and defect engineering to enhance chemical stability, and regulating the electrolyte to stabilize the interface reaction, balancing volume expansion and long life requirements, providing key technical support for the commercialization of SIBs.[76]

2.2 Insufficient conductivity

In the actual application of the SIB anodes, the insufficient conductivity of Mo- and W-based materials has a significant negative impact on battery performance. Firstly, the low conductivity will greatly increase the ohmic resistance inside the electrode, leading to severe overpotential during the charge and discharge process, which will reduce the energy efficiency of the battery, limit the power density, and make it difficult to meet the needs of high-power fast charging and discharging.[77] Secondly, the hysteresis of the electron conduction rate directly restricts the intercalation/deintercalation kinetics of Na^+. The active materials cannot fully participate in the electrochemical reaction, resulting in a decrease in the battery's specific capacity. Especially under high rate conditions, the capacity decay is more obvious.[78] Furthermore, uneven conductivity can cause imbalanced current distribution inside the electrode, resulting in local overheating and stress concentration, accelerating the structural destruction and pulverization of active materials, and significantly shortening the cycle life of the battery.[79]

The poor conductivity of Mo- and W-based materials is mainly restricted by the characteristics of electronic structure and crystal structure. From the perspective of electronic structure, Mo- and W-based materials are mostly semiconductors or insulators, all of which have relatively wide band gaps. The energy consumption of the electron transition is high, resulting in fewer free electrons and a weak electron conduction ability.[80] Taking MoS_2 as an example, the chemical bonds within its layers are mainly covalent bonds, while the interlayers are bound by weaker van der Waals forces. This structure greatly hinders the conduction of electrons between layers.[81] In terms of crystal structure, there are often problems with lattice defects, which scatter electrons and increase the resistance to electron transmission.[82,83] At the same time, Mo- and W-based materials will undergo phase changes (*i.e.* conversion reactions or alloying reactions) during the Na^+ intercalation/deintercalation process. The stress and structural changes generated during the phase change will further destroy the conductive network of the material, exacerbating the problem of insufficient conductivity.[84]

To address the aforementioned issues, researchers have conducted a lot of research on material structure design, composite modification, *etc*. In terms of structural optimization, nanofabrication can significantly shorten the electron transmission path, and the introduction of porous structures can improve the transmission efficiency of electrons and ions. Heterogeneous structure design utilizes interface effects to regulate the distribution of electron clouds, thereby improving the overall conductivity of the material.[85–87] In terms of the composite strategy, constructing a continuous conductive network by combining it with highly conductive carbon materials can not only effectively improve the conductivity of the electrode, but also buffer the volume change during charging and discharging. These methods provide theoretical guidance for the design of high-performance Mo- and W-based anode materials in SIBs.[88,89]

2.3 Interfacial side reactions

In the anode system of SIBs, Mo- and W-based materials have become research hotspots due to their high theoretical capacity and unique layered structure, but interfacial side reactions seriously hinder improving their performance.[90,91] The interface side reaction will first lead to irreversible capacity loss, consume limited Na^+ and electrolyte resources, greatly reduce the initial coulombic efficiency of the battery, and continuously consume active materials during the cycling process, accelerating capacity decay.[92,93] Meanwhile, the side reaction products will form an unstable SEI layer on the electrode surface. The repeated rupture and regeneration of the membrane will not only increase the internal resistance of the battery, but also cause the electron transfer efficiency to decrease, thus deteriorating the rate performance of the battery.[94,95]

In addition to the issue of interfacial side reactions, the instability of the SEI layer remains a significant challenge for Mo- and W-based anodes. The chemical composition of the SEI on Mo- and W-based materials is still not fully understood. Studies have shown that, in carbonate-based electrolytes, the SEI consists of both inorganic components such as Na_2CO_3 and organic fragments derived from solvent decomposition, such as alkyl carbonates and ester compounds. In ether-based electrolytes, the SEI may contain more organic components, with the presence of compounds like Na_2O and ether-derived organic salts.[96] The differences in the SEI composition between these two types of electrolytes highlight a major issue for Mo- and W-based materials, namely electrolyte compatibility. This issue is less pronounced in more widely used anode materials like hard carbon or titanium-based oxides, where the SEI layer tends to be more stable. Additionally, high-concentration electrolytes can further complicate SEI formation due to their different interactions with the surface of Mo- and W-based materials. In these systems, the SEI tends to be thicker and less stable, leading to increased internal resistance and reduced overall performance. These differences underscore the need for further research into the stability and composition of the SEI layer on Mo- and W-based anodes, as well as strategies for improving electrolyte compatibility and interface stability.[97]

The root cause lies in the thermodynamic and kinetic incompatibility between Mo- and W-based materials and the electrolyte. In terms of thermodynamics, there are a large number of unsaturated coordinated atoms and active sites on the surface of Mo- and W-based materials, which have high reactivity with organic solvents and electrolyte salts in the electrolyte and are prone to reduction and decomposition.[98,99] For example, after the carbonate solvent in the electrolyte gains electrons on the electrode surface, it decomposes to produce gases such as CO_2 and CO as well as organic fragments. These fragments combine with Na^+ to form SEI membrane components.[100] Kinetically, during the Na^+ intercalation/deintercalation process, the material structure changes significantly, exposing new active surfaces, resulting in continuous electrolyte infiltration and side reactions.[101] In addition, surface defects and grain boundary regions of the material will further reduce the activation energy of the reaction.

The problem of interface byproducts needs to be solved through aspects such as material structure optimization and interface modification. In terms of material structure optimization, nano-scaling can be used to reduce the material size, shorten ion diffusion paths, reduce local concentration gradients, and reduce side reactions caused by uneven ion migration.[102,103] In terms of interface modification, atomic layer deposition (ALD) technology is used to coat the material surface with inert oxide layers such as Al_2O_3 and TiO_2, or conductive polymers are coated by chemical deposition. This can not only inhibit electrolyte penetration, but also optimize electron conduction and reduce interfacial charge accumulation. Element doping can also be used to regulate the surface electron cloud density and weaken the reaction activity of active sites with the electrolyte.[104,105]

3. Sodium storage mechanisms in Mo- and W-based materials

In research on SIBs, Mo- and W-based materials have attracted much attention due to their diverse crystal structures and rich redox chemistry.[106] Their sodium storage mechanism is not dominated by a single mode, but is a complex and synergistic system composed of intercalation/deintercalation, conversion reactions, and pseudocapacitive behavior.[107] Among them, the intercalation/deintercalation mechanism lays the foundation for reversible cycling, relying on the reversible diffusion of Na^+ in the material interlayer or tunnel; the conversion reaction mechanism contributes a high specific capacity through violent phase transitions, but is also accompanied by structural reconstruction and challenges; and pseudocapacitive behavior, as a surface-controlled rapid process, significantly improves the rate performance of the material (Fig. 3).[108–110] A deep understanding of the interaction and balance of these three mechanisms, and the ability to artificially control them through nanostructure design, composite formation and defect engineering of materials, is key to unlocking the high-performance sodium storage capacity of Mo- and W-based materials.

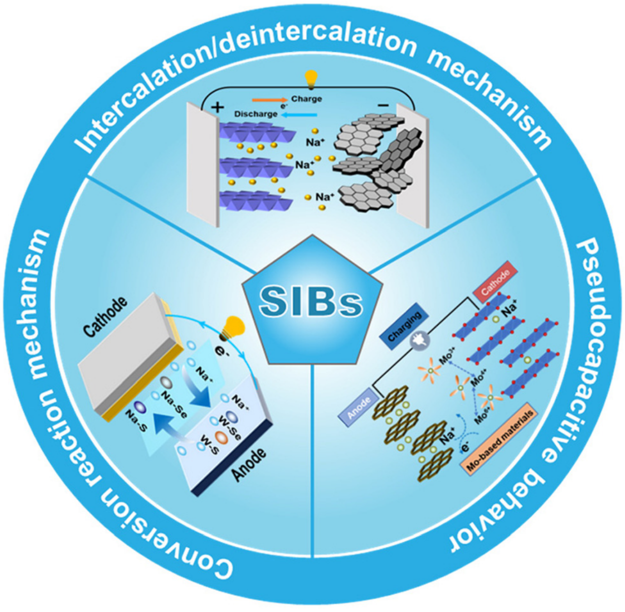

Fig. 3 Sodium storage mechanism of Mo- and W-based materials in SIBs.

3.1 Intercalation/deintercalation mechanism

In the SIB system, Mo- and W-based materials exhibit unique sodium storage properties, and their intercalation/deintercalation mechanism is the key to understanding their energy storage performance. (1) Some Mo-based oxides have layered or tunnel-like structures. For example, in layered MoO_3, there are certain gaps between the layers, which provide channels for the insertion of Na^+. When the battery is charged, electrons in the external circuit flow into the material and combine with incoming Na^+. Na^+ is gradually intercalated in the MoO_3 interlayer, resulting in an increase in the interlayer spacing. This process is accompanied by a change in the oxidation state of the Mo ions, from a high valence state to a low valence state, to maintain the electrical neutrality of the material.[111] During the discharge process, Na^+ is deintercalated from the interlayer and returns to the electrolyte, while electrons flow out through the external circuit, and the oxidation state of Mo ions returns to a higher valence state, completing a complete intercalation/deintercalation cycle. Mo sulfide also has a special structure for sodium storage.[112] (2) Taking Mo-based sulfides as an example, MoS_2 has a sandwich-like structure consisting of a Mo atomic layer sandwiched between two S atomic layers.[113] When storing sodium, Na^+ tends to embed into the interlayer van der Waals gap of MoS_2. As Na^+ is intercalated, the crystal structure of MoS_2 expands to a certain extent, and the electron cloud distribution of Mo atoms and S atoms changes, causing slight changes in the Mo–S bond length and bond angle.[114] This structural change affects the intercalation/deintercalation dynamics of Na^+ to a certain extent. In the subsequent extraction and insertion process, the structure gradually recovers. After multiple cycles, the repeated structural changes may cause partial structural damage to the material, affecting the cycling stability of the battery.[115] (3) For some Mo-based composites, the sodium storage mechanism is more complicated. When Mo-based materials are composited with carbon materials, the carbon materials can improve the conductivity of the materials. In addition, their porous structures or functional groups can provide additional adsorption sites for Na^+.[116] During the charge and discharge process, in addition to the Na^+ intercalation/deintercalation reaction of the Mo-based material, the carbon material may also participate in sodium storage, storing a certain amount of Na^+ through surface adsorption or the formation of weak chemical bonds. This synergistic effect helps to improve the overall sodium storage capacity and rate performance of the material.[117] Moreover, W-based materials (such as WO_x) undergo similar redox reactions and accompanying crystal phase transitions to those of Mo-based materials when storing sodium. When Na^+ is embedded, the original crystal structure may transform from one crystal phase to another crystal phase that is more conducive to the accommodation of Na^+. This process is also accompanied by a change in the oxidation state of W ions to balance the charge. During the deintercalation process, the crystal phase undergoes a reverse transformation. At the same time, some defects or amorphous areas on the surface of the material may also play an important role in the rapid adsorption and desorption of Na^+, affecting the overall sodium storage kinetics.[118]

The sodium storage mechanism of Mo- and W-based materials involves many factors, such as changes to the material structure, changes to the ion oxidation state, and synergistic effects with other composite components. Understanding these mechanisms is of great significance for further optimizing the sodium storage performance of materials.

3.2 Conversion reaction mechanism

The conversion reaction mechanism of Mo- and W-based sulfide compounds in the SIB system is the core path for sodium storage, which is characterized by "chemical bond breakage and recombination–product phase change–reversible redox". At the beginning of discharging, Na^+ is intercalated in the layered structure, triggering the dissociation of Mo/W–X (X = S/Se) bonds, and generating metallic Mo/W nanoparticles and Na_2X (such as Na_2S, Na_2Se) through electrochemical reactions. This process is accompanied by the influx of electrons and the collapse of the crystal structure to form a nanocomposite phase. The reverse reaction theoretically restores the original material during the charging process, but in reality, it is affected by product agglomeration, side reactions and kinetic hysteresis, resulting in capacity decay.[119–121] Structural differences in the materials will affect the conversion process. Compared with MoS_2, the high oxidation state of W in WS_2 results in a higher reaction potential and stronger W–S bond energy, leading to slower initial intercalating kinetics. $MoSe_2$ and WSe_2 have a large Se atomic radius, wide interlayer spacing and ion diffusion channels, but the difference in Se electronegativity changes the electron cloud distribution, resulting in different Mo/W–Se bond dissociation energies.[122] It is worth noting that although W-based materials follow a similar transformation path, the high oxidation state of W makes the reaction potential higher, the interlayer van der Waals force weaker, and the ion diffusion energy barrier lower; this increases the risk of structural collapse during cycling.[123,124]

To overcome the problems in the conversion reaction faced by Mo- and W-based materials when applied to SIBs, various strategies have been adopted.[125] On one hand, by carefully designing the microstructure of the material, such as constructing nanostructures and porous structures, the influence of volume changes can be mitigated, the structural stability of the material can be increased, and the transmission and diffusion of Na^+ can be facilitated. On the other hand, by adopting the strategy of forming composites with other materials, such as composites with highly conductive carbon materials, the overall conductivity and rate performance of the Mo- and W-based materials can be improved, which will indicate the direction for designing high specific energy and long-life anode materials for SIBs.[126,127]

3.3 Pseudocapacitive behavior

The pseudocapacitive behavior of Mo- and W-based materials and the sodium storage mechanism originate from the rapid and reversible redox reaction and ion adsorption process on the surface.[128] This mechanism uses the atomic layer (edge sites or defect areas) on the surface of the material as the active center. Na^+ diffuses to the surface of the material through the electrolyte, and rapid electron transfer occurs with the surface active site, triggering a change in the valence state of the Mo/W ions. At the same time, it is accompanied by surface adsorption or short-range embedding of Na^+, forming a pseudocapacitive response.[129,130] This process is different from traditional diffusion-controlled intercalation/deintercalation, in that its kinetics only depends on the surface ion adsorption–electron transfer rate.[131] Specifically, during the Na^+ intercalation/deintercalation process, Mo-based oxides and sulfides can achieve multi-electron transfer through the valence change of the Mo element (such as $Mo^{6+} \rightarrow Mo^{4+} \rightarrow Mo^0$), and the rapid adsorption and desorption reaction of surface ions produces pseudocapacitive behavior.[132] For example, MoO_3 nanosheets construct a high specific surface area structure, allowing Na^+ to undergo rapid redox reactions on the surface, significantly improving the rate performance, while the layered structure of MoS_2 not only enables Na^+ intercalation, but also accelerates ion storage dynamics through pseudocapacitive reactions at the edge active sites.[133] W-based materials also exhibit excellent pseudocapacitive properties.

Table 1 Analysis of the storage mechanisms of Mo- and W-based materials in SIBs

Representative substances	Sodium storage mechanisms	Sodium storage principle	Main causes of failure	Ref.
Mo-based sulfides (MoS_2)	Intercalation/deintercalation	Reversible diffusion and intercalation of Na^+ between the layers; the Mo valence state reversibly changes in conjunction with electron/Na^+ coupling to maintain electrical neutrality	Interlayer spacing changes/unstable SEI layer	118
Mo-based materials/carbon composites (MoS_2/C)	Intercalation/deintercalation	Carbon enhances electronic conductivity, and the porous structure/functional groups provide additional Na^+ adsorption sites	Volume change	115
W/Mo-based selenides (WSe_2/$MoSe_2$)	Conversion reaction	This is a "bond breaking–product phase transition–reversible redox" reaction pathway; Se influences the bond energy and reaction kinetics	Structural collapse	119
Mo-based sulfides (MoS_2)	Conversion reaction	The reaction involves a transformation from interlayer intercalation to Mo–S bond breaking; the charging reversibility is limited by kinetics	Phase transition or volume change	120
Mo-based sulfides (MoS_2)	Pseudocapacitive behavior	Na^+ undergoes rapid and reversible redox reactions at surface defects; its kinetics depend on the surface reaction rate, not bulk diffusion	Structural collapse	135

The high valence state and stable lattice structure of the W element help maintain the reversibility of the pseudocapacitive reaction. After nano-scaling or composite modification, the active sites can be further exposed.[134,135] However, the structure and defect engineering of materials have a significant impact on pseudocapacitive behavior. Nanosizing can significantly increase the specific surface area and expose more edge active sites, while the introduction of defects such as oxygen vacancies and sulfur vacancies can optimize the electronic structure and reduce the reaction energy barrier.[136,137]

However, the pseudocapacitive behavior of Mo- and W-based materials still faces challenges in practical applications. On one hand, the surface structure is easily destroyed by repeated intercalation/deintercalation of ions during long-term cycling, resulting in pseudocapacitive capacity decay. On the other hand, insufficient intrinsic conductivity limits the surface reaction rate.[138] Current research optimizes the electron transmission pathways and surface activity of materials through defect engineering, nanostructure design and carbon-based composite strategies, synergistically improving the pseudocapacitance contribution and cycling stability, which will provide important theoretical support for the development of high-performance sodium-ion battery electrode materials.[139] Table 1 summarizes the analysis of sodium storage mechanisms for some representative molybdenum and tungsten materials. Generally, a thorough understanding of the three sodium storage mechanisms (intercalation/deintercalation, conversion reactions and pseudocapacitive behavior) is key to unlocking the high-performance sodium storage capabilities of W- and Mo-based materials.

4. Performance optimization strategy for Mo- and W-based materials

4.1 Structural design

4.1.1 Nanoscale design. The preparation of nanostructured Mo- and W-based materials by different methods has a significant effect on improving the performance of materials. Nanostructured Mo- and W-based materials have a high specific surface area and can provide more active sites to promote the adsorption and reaction of Na^+.[140–142] Studies have shown that for layered MoS_2/WS_2 materials, the optimal interlayer spacing for optimizing Na^+ diffusion pathways and improving the performance is in the range of 0.8–1.2 nm. This range facilitates efficient Na^+ intercalation and minimizes the negative effects of volume expansion, while excessively large or small interlayer spacings can adversely affect cycling stability. During the charge and discharge process, more active sites allow sodium ions to embed and extract from the material more quickly, thereby improving the rate performance of the battery.[143] Nanostructures can shorten the diffusion path of Na^+. Due to their small size, the diffusion distance of Na^+ ions inside the material is significantly shortened, allowing them to reach active sites faster and participate in electrochemical reactions. This enables the battery to respond to current changes more quickly during the charging and discharging process, reduces electrode polarization, and improves the charging and discharging efficiency of the battery. The nanostructure can also effectively alleviate the volume change problem during the charging and discharging process. Due to the small size of nanoparticles, the internal stress generated during volume expansion and contraction is relatively small.[144] Furthermore, nanoscale design strategies also have a significant impact on the initial coulombic efficiency (ICE). While a larger specific surface area provides abundant reaction sites, it also means that a larger amount of SEI film will form during the first charge–discharge cycle, consuming more sodium ions and typically leading to a lower ICE. To mitigate this problem, research often employs surface engineering (such as carbon coating) or pre-sodiation to guide the formation of a thinner and more stable SEI on the surface of the nanostructure, thereby reducing irreversible sodium loss and improving the first-cycle efficiency while still leveraging the kinetic advantages of the nanostructure.[145]

The design of Mo-based nanostructured materials can be achieved through a variety of methods, each with its own characteristics and advantages. The hydrothermal method is a commonly used method for preparing nanostructured Mo-based materials. Taking the preparation of nano-MoS_2 as an example, the molybdenum source and the sulfur source react chemically in a high-temperature and high-pressure aqueous solution environment in the hydrothermal reaction system. The sulfur source decomposes to produce sulfur ions, which combine with molybdenum ions to gradually form MoS_2 nanostructures. As shown in Fig. 4a, Nabilah Al-Ansi *et al.* prepared carbonized polymer dots (CPDs) by a hydrothermal method and annealing treatment using citric acid and ethylenediamine as raw materials. After hydrothermal treatment with Na_2MoO_4, thioacetamide and CPDs at 180 °C for 24 h and annealing at 700 °C under a H_2/Ar atmosphere for 2 h, a MoS_2@CPD material with a uniform 3D nanoflower-like microsphere structure was prepared (Fig. 4b). Its large specific surface area and rich pore structure enable it to maintain a practical capacity of 302.8 mAh g^{-1} after 500 cycles at a current density of 0.5 A g^{-1} (Fig. 4c).[146] By precisely controlling the reaction conditions, the size and morphology of nano-MoS_2 can be regulated. Specifically, MoS_2 with a relatively uniform nanosheet structure can be obtained when the concentration ratio of the molybdenum source and the sulfur source is appropriate.

Similarly, Bai *et al.* used Na_2MoO_4 and thiourea as raw materials with multi-walled carbon nanotubes (MWCNTs)

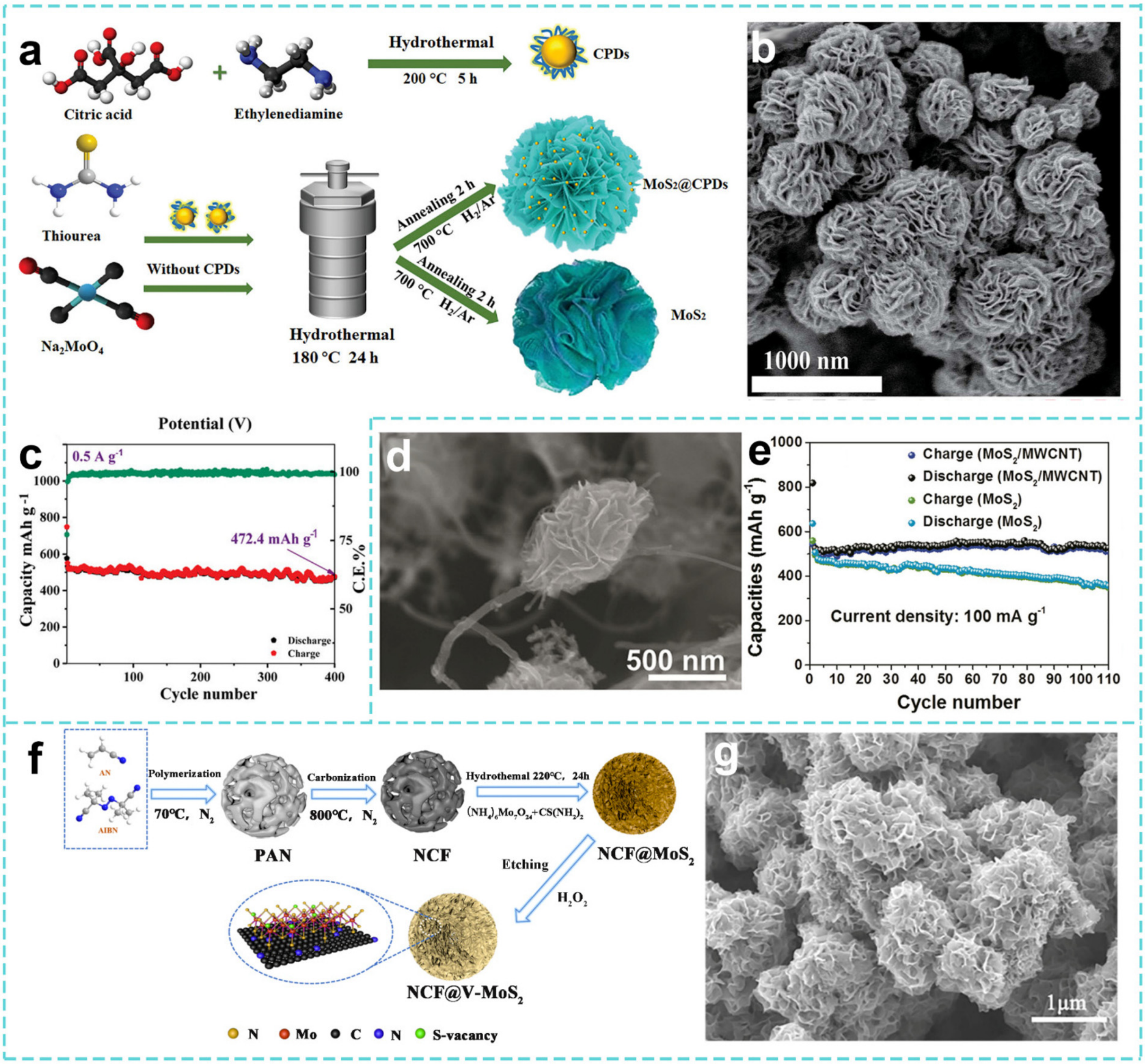

Fig. 4 (a) Schematic demonstration of the synthesis of CPDs, MoS_2, and MoS_2@CPDs. (b) SEM image and (c) cycling performance of MoS_2@CPDs-2 at 0.5 A g^{-1}. Reproduced with permission from ref. 146. Copyright 2023, Wiley. (d) SEM image of the MoS_2/MWCNT composite. (e) Cycling of the MoS_2/MWCNT and MoS_2 electrodes. Reproduced with permission from ref. 147. Copyright 2018, American Chemical Society. (f) Schematic of the synthesis process and (g) SEM image of NCF@V-MoS_2. Reproduced with permission from ref. 148. Copyright 2022, Elsevier.

through a hydrothermal reaction at 190 °C for 36 h to synthesize a nanoflower-shaped neuron-like MoS_2/MWCNT composite material in one step (Fig. 4d). As shown in Fig. 4e, the nanoflower microspheres are connected by carbon nanotubes, which have both a large specific surface area and high conductivity. The discharge capacity is maintained at 527.7 mAh g^{-1} after 110 cycles at 100 mA g^{-1}, and the capacity retention rate is about 100%.[147] Hu *et al.* anchored MoS_2 nanosheets with S vacancies on a 3D flower-shaped nitrogen-doped carbon framework (NCF@V-MoS_2) by a similar hydrothermal method to prepare a nanoflower-shaped microsphere structure (Fig. 4f and g).[148] In the experiment, ammonium molybdate was used as a molybdenum source and thiourea as a sulfur source, and the pre-prepared N-doped carbon flower was used as the supporting framework for a hydrothermal reaction at 220 °C for 24 h. The practical capacity of NCF@V-MoS_2 remained at 413 mAh g^{-1} after 300 stable cycles at a current density of 1 A g^{-1}.

In the study of the sodium storage mechanism and structural design of W-based sulfide compounds, Yang *et al.* adopted a solvothermal strategy to prepare a 3D hollow microflower-like WS_2-based hybrid material (H-WS_2@NC) by *in situ* interlayer modification of a nitrogen-doped carbon matrix using 2D WS_2 nanosheets with extended interlayers as building blocks for bottom-up self-assembly (Fig. 5a). As shown in Fig. 5b, a 3D nano/micro-hollow structure was constructed with WS_2 nanosheets with extended interlayers as building blocks, which provided mass transfer and electron transfer channels, an internal space to adapt to volume changes, and reduced ion diffusion energy barriers, so that the SIBs performed better (Fig. 5c).[149] With continued improvement of the performance requirements for transition-metal dichalcogenide (TMD)-based electrode materials, Wang *et al.* made new attempts to expand the application scenarios and optimize the performance of WS_2 materials. As shown in Fig. 5d and e, they developed a hybrid nanostructure of nitrogen-doped graphene

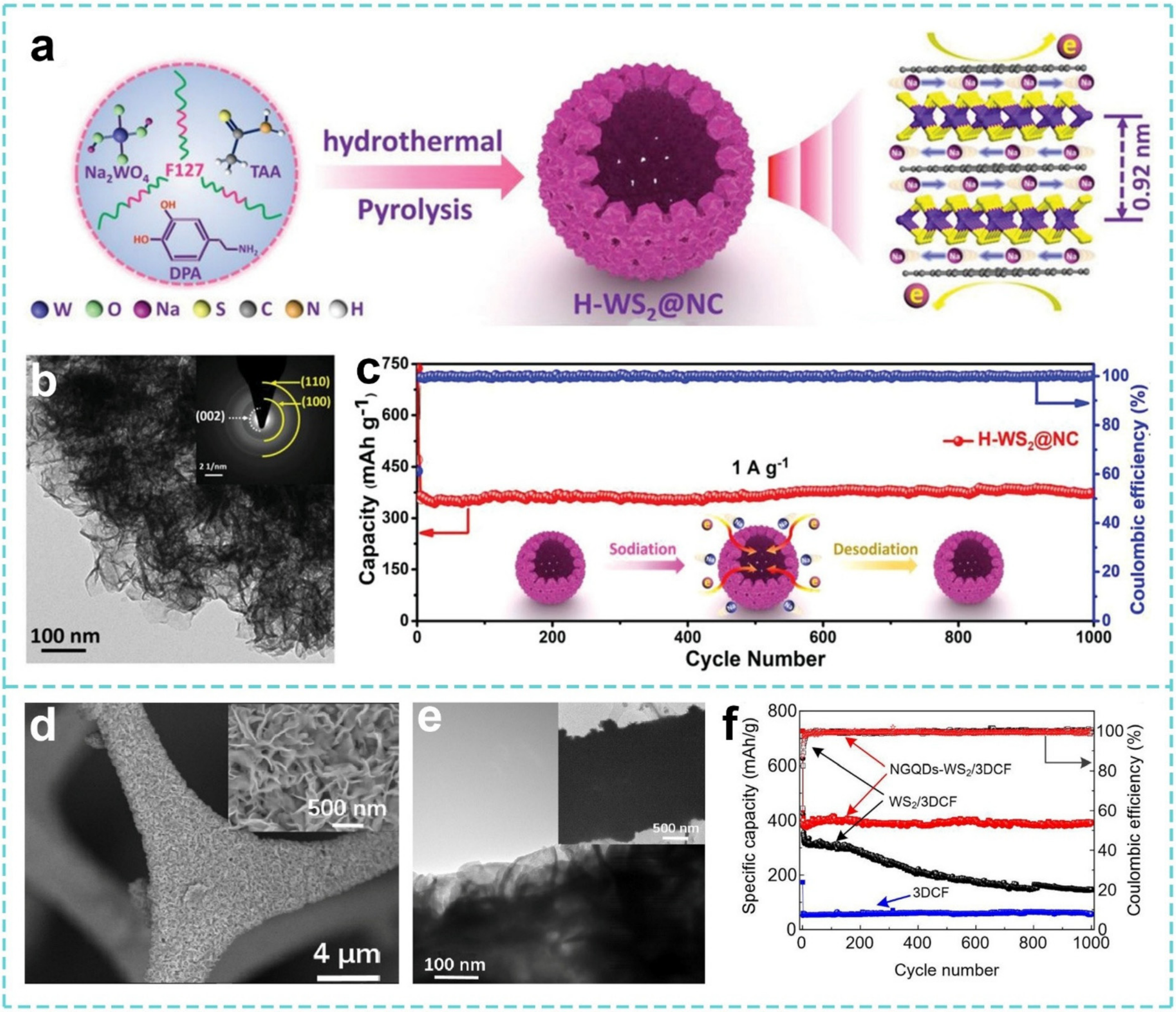

Fig. 5 (a) Illustration of the synthesis process for H-WS_2@NC. (b) TEM images of H-WS_2@NC. (c) Long-term cycling performance of the H-WS_2@NC electrode. Reproduced with permission from ref. 149. Copyright 2019, Wiley. (d) SEM image and (e) TEM image of the NGQD WS_2/3DCF nanoarchitecture. (f) Cycling performance of the 3DCF, WS_2/3DCF and NGQDs WS_2/3DCF. Reproduced with permission from ref. 150. Copyright 2013, RSC.

quantum dots decorated with WS_2 nanosheets and anchored with porous 3D carbon foam (NGQDs-WS_2/3DCF). The porous structure of carbon foam is used to provide mechanical support and shorten the ion diffusion path. The strong interface effect of NGQDs is used to anchor the WS_2 nanosheets to inhibit stacking and volume expansion, so that the material has a practical capacity of 268.4 mAh g^{-1} at 2000 mA g^{-1} and a capacity retention rate of 97.1% after 1000 cycles (Fig. 5f).[150]

The aforementioned research systematically demonstrates the results of exploring Mo- and W-based nanomaterials in SIBs, covering various aspects from material structure design to innovative preparation methods. From the high number of active sites and short diffusion paths given by the nanostructure to the precise control of material morphology such as by means of a hydrothermal method and breakthroughs in structural design and mechanistic analysis of W-based materials, researchers continue to explore the potential for improving material performance through multi-dimensional exploration. Overall, nanoengineering has significantly improved the rate performance and cycling stability of Mo- and W-based anode materials, endowing them with more active sites, shorter Na^+ diffusion pathways, and greater tolerance to volume changes. However, as research transitions from the laboratory to practical applications, the engineering feasibility urgently needs to be evaluated. Hydrothermal/solvothermal synthesis methods offer advantages in controlling material morphology and size, but large-scale preparation faces challenges such as uneven heat and mass transfer, long reaction times, and energy consumption and cost issues associated with high-temperature processing.[151] Therefore, future nanostructure design should focus on scalable synthesis routes, simplified post-processing techniques, and compatibility with high-loading electrode manufacturing to achieve an effective transition from fundamental research to engineering applications.

4.1.2 Porous and hollow structure design. The design of porous and hollow structures is an effective optimization strategy for constructing electrode materials with structural features.[152] From the perspective of structural characteristics, the porous structure increases the specific surface area, provides more active sites, and accelerates ion diffusion through the pore network, and the hollow structure buffers the volume expansion stress and improves the cycling stability through the internal hollow space.[153] In terms of design and preparation, researchers have achieved precise control of the porous-hollow structure through templating methods, self-assembly methods, and hydrothermal methods.[154] For example, the hard template method can control the size and shape of the pores, the soft template method can self-assemble the material through intermolecular forces, and the combination of a hydrothermal method and a self-assembly method can prepare multi-level pore structures, which will lay the foundation for performance optimization and the large-scale preparation of materials. Similarly, the design of porous and hollow structures has a dual impact on the ICE of the material. On one hand, their high specific surface areas and abundant pores provide more active sites while also intensifying the contact between the electrode and the electrolyte, potentially leading to more significant SEI formation and irreversible sodium consumption, thus reducing the ICE. On the other hand, by precisely controlling the pore structure (such as pore size) and surface chemical properties, and combining strategies such as carbon coating or pre-sodiation, it is possible to effectively guide the formation of a stable and dense SEI, utilizing its structural advantages to buffer volume expansion while reducing irreversible loss of active sodium. Therefore, fine-tuning of the surface and interface engineering of porous/hollow structures is a key research direction for balancing their kinetic advantages and first-cycle efficiency.[155,156]

In research on anode materials for SIBs, although the mesoporous structure is effective at improving the exposure of active sites, further enhancing the interfacial bonding between the active components and the carbon matrix to inhibit structural instability during the cycle remains an urgent problem to be solved. In response to this challenge, Wei *et al.* used a SiO_2 template-assisted solvothermal reaction and subsequent high-temperature pyrolysis to synthesize a composite material that grew ultra-thin metal-phase MoS_2 nanosheets on the inner surface of mesoporous hollow carbon spheres (M-MoS_2@HCS) (Fig. 6a–c).[157] The mesoporous hollow carbon spheres provide flexible support and ion diffusion channels to inhibit MoS_2 aggregation and volume expansion, thus M-MoS_2@HCS has a practical capacity of 401.3 mAh g^{-1} at 0.1 A g^{-1} for 100 cycles (Fig. 6d). Its composite structure significantly improves the reversibility of the sodium storage conversion reaction by synergistically accelerating electron transport, optimizing ion paths and buffering volume changes. On this basis, in view of the problems of poor conductivity, large volume changes and particle agglomeration of MoS_2 as the anode of SIBs, Ma *et al.* adopted a template-free two-step dissolution thermal synthesis strategy to prepare a MoS_2/C composite material of ultrathin nanosheets assembled on lignite-based carbon (Fig. 6e). As shown in Fig. 6f and g, the hollow structure alleviates volume expansion and shortens the Na^+ diffusion path, and the strong interface between lignite-based carbon and MoS_2 improves the conductivity and inhibits agglomeration. Thus, the practical capacity of the MoS_2/C composite material is still 431 mAh g^{-1} after 2000 cycles at 20 A g^{-1} (Fig. 6h), and the sodium storage performance is optimized through the synergistic mechanism of "hollow structure buffering–carbon-based enhanced conductive dispersion".[158] With an in-depth understanding of the structure–performance relationship, researchers have further expanded the design of porous-hollow structures from single materials to multi-component composite systems. Cui *et al.* used a hard template method to synthesize a composite material of hollow porous double-shell N/S-doped carbon@WS_2 nanospheres (NSC@WS_2) (Fig. 6i and j).[159] The constructed hollow porous double-shell structure effectively buffers the volume expansion during the cycle and shortens the Na^+ diffusion path. The N/S-doped carbon inner shell improves the conductivity of the composite material and accelerates electron transfer. As shown in Fig. 6k, the reversible

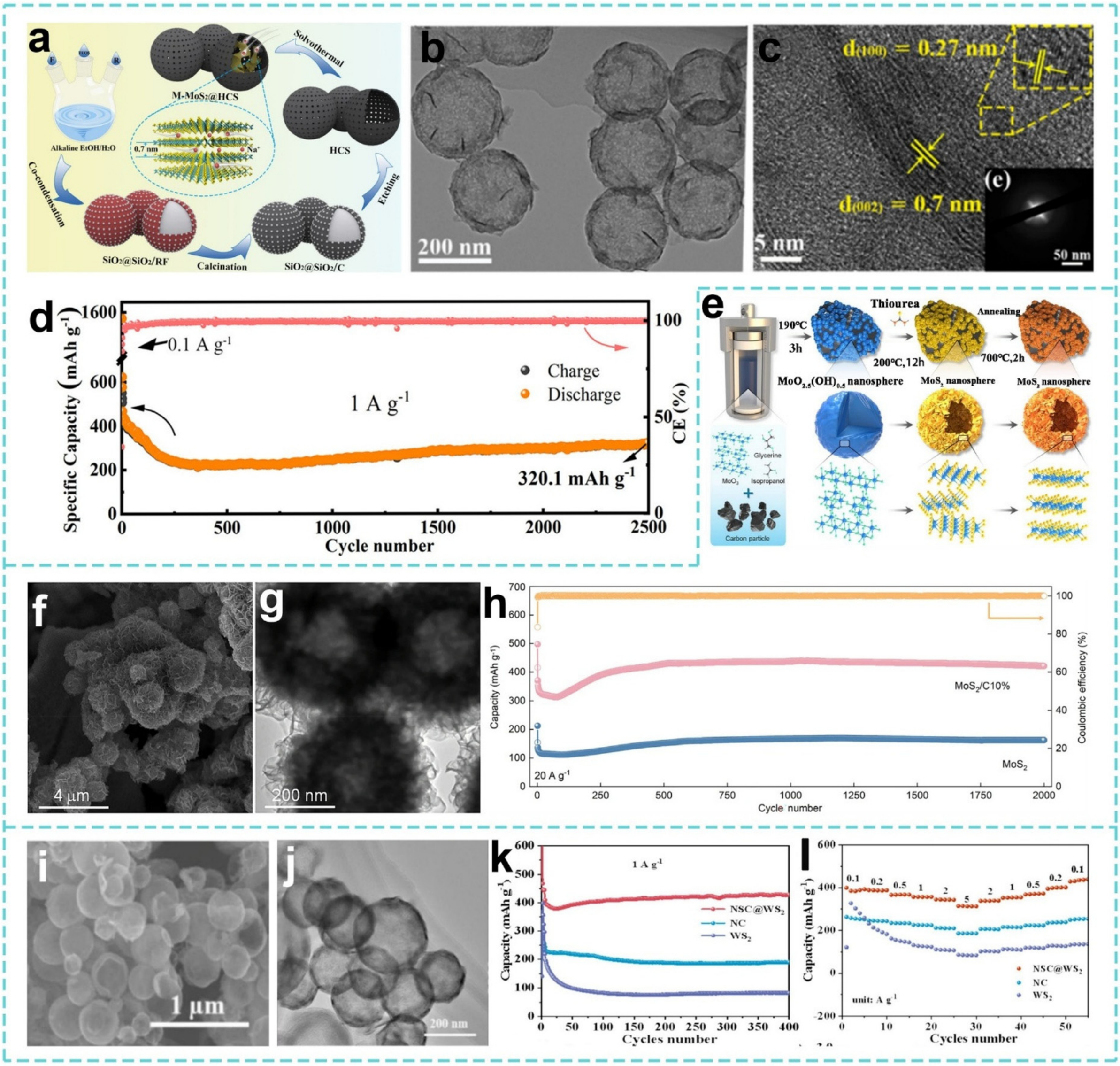

Fig. 6 (a) Illustration of the synthesis process, (b) TEM image, and (c) HRTEM image of M-MoS_2@HCS. (d) Cycling performance of the M-MoS_2@HCS electrode at 1.0 A g^{-1}. Reproduced with permission from ref. 157. Copyright 2021, American Chemical Society. (e) Illustration of the synthesis process, (f) SEM image, and (g) TEM image of MoS_2/C. (h) Long cycle life of the MoS_2 and MoS_2/C electrodes at 20.0 A g^{-1}. Reproduced with permission from ref. 158. Copyright 2025, Springer Nature. (i) SEM image and (j) TEM image of NSC@WS_2. (k) Cycling performances and (l) rate performances of the NC, WS_2, and NSC@WS_2 electrodes. Reproduced with permission from ref. 159. Copyright 2025, Elsevier.

capacity of the material remains at 428 mAh g^{-1} after 400 cycles at 1 A g^{-1}. The material improves the rate performance through the collaborative design of "hollow structure to buffer volume changes–doping carbon to improve conductivity–ultra-thin double shell to optimize ion transport", overcoming the application bottleneck of WS_2 (Fig. 6l).

4.2 Composite and hybrid design

A carbon coating, as a core composite strategy for SIB electrode materials, constructs a conductive network–mechanical barrier–interface regulation synergistic system by regulating the structure, composition and thickness of the carbon layer.[160,161] Research has shown that when Mo- and W-based materials are hybridized with carbon, a carbon content of 5–10% can significantly enhance conductivity while maintaining a high specific capacity and good cycling stability. However, if the carbon content exceeds 15%, the specific capacity may decrease because the carbon layer occupies too many active sites. It is worth noting that rational composite and hybridization designs are also crucial for controlling the ICE. While the introduction of a carbon layer can improve conductivity and buffer volume changes, it may also consume a certain amount of sodium ions during the first cycle due to the formation of the SEI, thus affecting the ICE. By precisely controlling the thickness, crystallinity, and surface chemistry of the carbon layer, high ICE can be achieved. For example, by constructing a uniform and dense thin carbon coating, introducing appropriate surface functional groups, or performing pre-sodiation treatment, it is possible to promote the formation of a more stable and thinner SEI without significantly sacrificing active sites. This allows for the synergistic optimization of ICE by effectively reducing irreversible sodium loss while simultaneously leveraging the structural protection and conductivity enhancement effects of the carbon layer.[162] In the study of structural–functional synergistic optimization of anode materials for SIBs, Tan *et al.* developed a 2D heterostructure composite material of carbon-coated $MoSe_2$/MXene ($MoSe_2/Mo_2CT_x/C$). From the unique structure of MXene-coated $MoSe_2$ particles with loose carbon connections, the MXene layer enhances the surface activity of $MoSe_2$, and the carbon layer provides rich pores, which synergistically improve the ion diffusion efficiency (Fig. 7a and b). As shown in Fig. 7c, there is a good specific capacity at different current densities after 2200 cycles. This heterostructure effectively inhibits $MoSe_2$ agglomeration and enhances structural stability and ion conductivity through the synergistic effect of MXene interface activation and carbon layer pore optimization, as well as charge transfer regulation.[163] Lu *et al.* further deepened the "interface-component" synergistic strategy and proposed an innovative path for strengthening the N-rich nitride substrate (Fig. 7d–f), which used the Mo–aniline skeleton as a precursor to prepare a composite material of carbon-coated N-rich Mo_xN modified few-layer $MoSe_2$ nanosheets ($MoSe_2@Mo_xN$/C-I) through calcination, selenization and nitridation processes. The carbon layer effectively enhances the structural stability and conductivity of Mo_xN, and nitrogen-rich Mo_xN and few-layer $MoSe_2$ form a rich heterogeneous interface, providing a large number of active sites to accelerate Na^+ diffusion and charge transfer. As shown in Fig. 7g, the reversible capacity is 178.6 mAh g^{-1} after 10 000 cycles at 20 A g^{-1}, and the capacity retention rate is 98.8%.[164]

In the study of W-based carbon composites, Wang *et al.* prepared a carbon–uniformly encapsulated WS_x precursor by a one-pot method combined with a high chloride hydrolysis method (Fig. 7h). Then selenization–co-carbonization were carried out to finally obtain a $WSSe_2$/C composite material (Fig. 7i and j), which significantly enlarged the lattice spacing by constructing a built-in electric field, thereby ensuring fast and stable Na^+ transport. The $WSSe_2$/C-1 anode showed a high specific capacity of 715.3 mAh g^{-1} after completing 200 cycles at 1 A g^{-1} (Fig. 7k).[165] This strategy of combining carbon encapsulation and a dual anion effect provides a reference for the development of high-power density W-based SIB anode materials.

In summary, the carbon coating strategy has built a multifunctional composite system for Mo- and W-based anode materials that integrates conductivity enhancement, structural stability, and interface optimization by precisely controlling the structure, composition, and dimensions of the carbon layer. From a single carbon layer coating to the multi-heterogeneous structure design, this strategy not only systematically solves the intrinsic electronic insulation, volume expansion, and interface instability problems of the material, but also achieves a cross-dimensional improvement in the sodium storage performance through the synergistic mechanism of conductive network construction, mechanical stress buffering and ion transport acceleration.

4.3 Defect and interface engineering

4.3.1 Heteroatom doping. Heteroatom doping (such as N, P, and Sn) is an effective modification strategy in Mo- and W-based anode materials for SIBs.[166] N doping adjusts the electron cloud density and reduces the ion diffusion energy by introducing lone pairs of electrons. At the same time, N atoms form strong chemical bonds with Mo and W atoms, enhance the structural stability of the material, and inhibit volume changes and structural collapse during charging and discharging.[167] P doping changes the reaction mechanism of the material by forming a highly active phosphide phase, which can reduce the charge transfer resistance of the material, enhance electronic conductivity, and provide additional sodium storage sites. In addition, P doping can also improve the interface properties of the material, inhibit electrolyte decomposition, reduce side reactions, and improve the coulombic efficiency and long-term cycling stability of the electrode. Sn doping mainly improves the performance by changing the crystal structure and electronic properties of the material. The atomic radius of Sn is similar to those of Mo and W, and it is easy to replace Mo and W atoms in the lattice, causing lattice distortion, expanding the interlayer spacing, and shortening the Na^+ diffusion path.[168] Therefore, doping with elements such as N, P, and Sn synergistically improves the conductivity, ion diffusion rate, and structural stability of Mo- and W-based anode materials through multiple mechanisms such as regulating the electronic structure, optimizing the crystal structure, and improving the interface properties. Furthermore, element doping plays a crucial role in regulating the ICE of materials. By introducing heteroatoms such as N and P, the surface chemical state and electronic structure of the material can be adjusted, promoting the formation of a more stable and denser SEI, thereby reducing the irreversible consumption of active sodium during the first cycle. For example, N doping leads to an electron-rich surface that facilitates the formation of a uniform SEI, while P doping forms a stable interface layer that suppresses electrolyte side reactions. By rationally selecting doping elements and controlling their concentration and distribution, targeted regulation of the SEI composition and structure can be achieved without sacrificing Na^+ transport kinetics, thus synergistically improving the material's initial efficiency and long-term cycling stability, further promoting its practical application.[169,170]

In the study of the structure–function synergistic design of anode materials for SIBs, MXene is an "all-around" two-dimensional material that combines high conductivity, hydrophilicity, excellent mechanical strength, and tunable surface chemistry. Therefore, Yu *et al.* synthesized a composite material (MoO_3/MoS_2/NC/MXene) with a N-doped carbon (NC) coating on MoO_3/MoS_2 modified on MXene nanosheets through gas-phase sulfidation and NC coating processes (Fig. 8a).[171] As

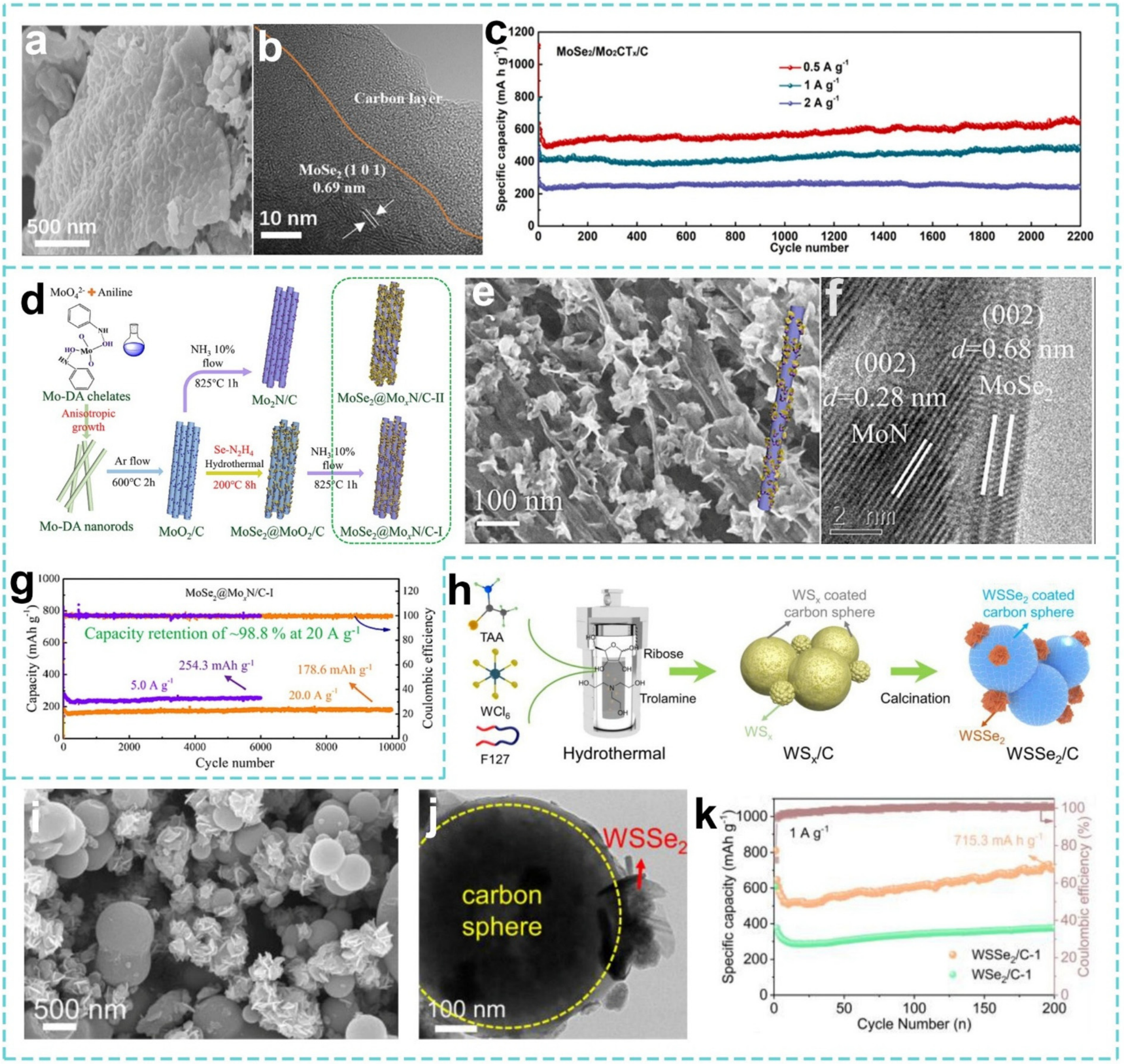

Fig. 7 (a) SEM image and (b) HRTEM image of the $MoSe_2/Mo_2CT_x/C$ material. (c) Cycling performance at 0.5, 1, and 2 A g^{-1} of the $MoSe_2/Mo_2CT_x/C$-containing cell. Reproduced with permission from ref. 163. Copyright 2022, Elsevier. (d) Illustration of the synthesis process for $MoSe_2@Mo_xN/C$. (e) SEM image and (f) HRTEM image of $MoSe_2@Mo_xN/C$-I. (g) Long cycling stabilities at 5.0 and 20.0 A g^{-1} of the $MoSe_2@Mo_xN/C$-I electrode. Reproduced with permission from ref. 164. Copyright 2022, Elsevier. (h) Illustration of the synthesis process for $WSSe_2/C$. (i) SEM image and (j) TEM image of $WSSe_2/C$-1. (k) Short cycling performance at 1 A g^{-1} of the $WSSe_2/C$-1 and WSe_2/C-1 electrodes. Reproduced with permission from ref. 165. Copyright 2024, Elsevier.

shown in Fig. 8b and c, the sulfurization treatment retains the MoO_3 nanobelt structure to improve conductivity, the construction of the MoO_3/MoS_2 heterostructure accelerates ion/electron diffusion, while the introduction of NC and MXene enhances the conductivity and inhibits volume expansion. Thus, the composite material has a high discharge capacity of 464 mAh g^{-1} at a current density of 0.1 A g^{-1} and still maintains 202 mAh g^{-1} capacity at a high current density of 5 A g^{-1} (Fig. 8d). This work laid the foundation for subsequent interface defect regulation.

Gao *et al.* converted the original MoO_3 into heterogeneous MoO_3/MoO_2 and proposed a heterogeneous $MoO_3/MoO_2@NC$ (Fig. 8e).[172] As shown in Fig. 8f and g, the MoO_3/MoO_2 composite structure was successfully synthesized. The hybrid MoO_3/MoO_2 structure significantly improved the electronic conductivity and introduced oxygen defects, and the external N-doped carbon layer enhanced the structural stability. The $MoO_3/MoO_2@NC$ material has a capacity of 190 mAh g^{-1} at 0.5 A g^{-1} after 5000 cycles, and shows an outstanding pseudocapacitive effect and wide temperature adaptability. Dong *et al.* proposed a spherical MoS_2 block coated with a polydopamine-derived N-doped carbon sphere ($MoS_2@NC$) material for SIBs.[173] As shown in Fig. 8i and j, the $MoS_2@NC$ core–shell structure spontaneously reorganizes into ultrafine nanosheets during

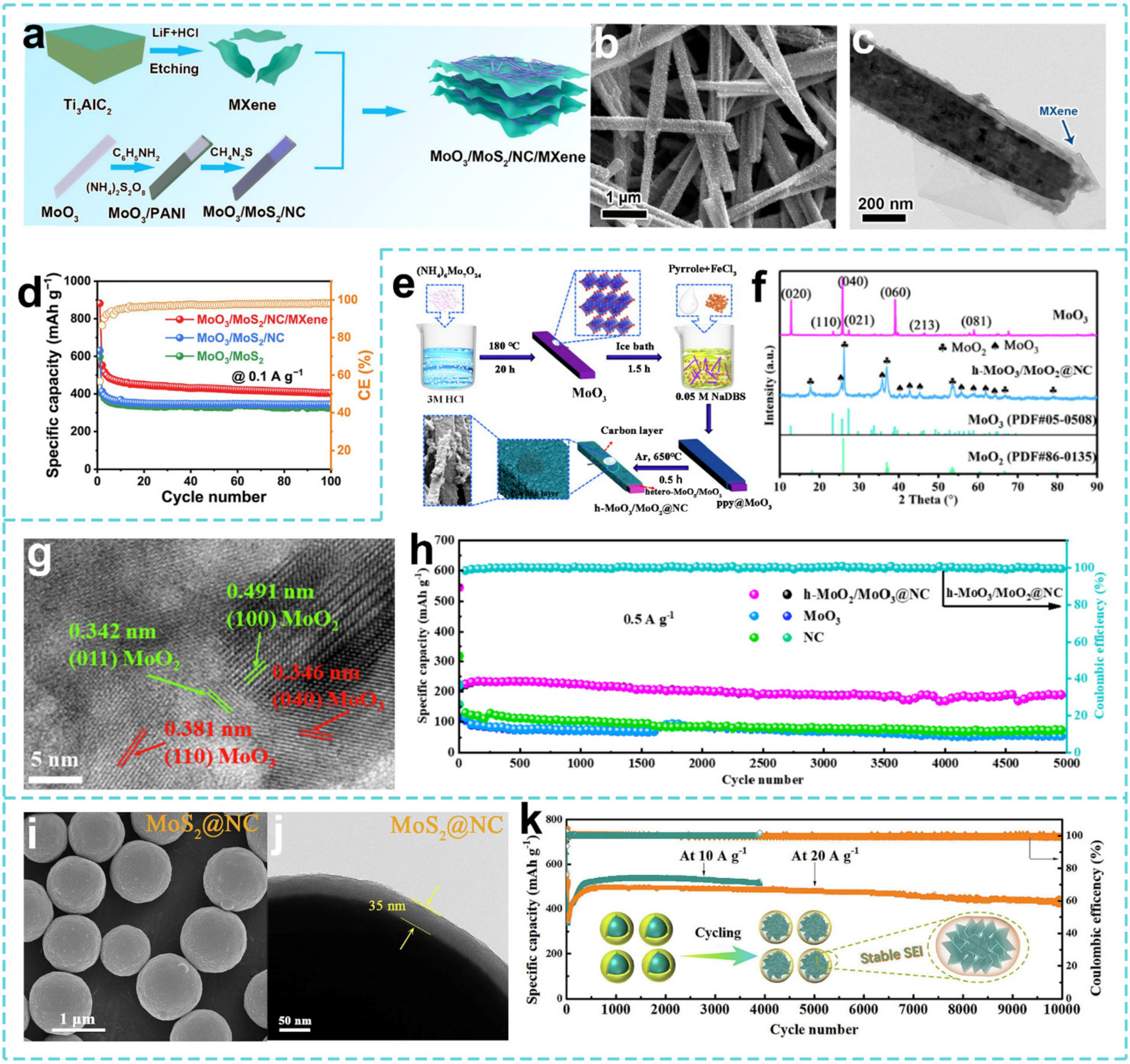

Fig. 8 (a) Illustration of the synthesis process, (b) SEM image, (c) TEM image of MoO_3/MoS_2/NC/MXene. (d) Cycling performance of the MoO_3/MoS_2/NC/MXene electrodes. Reproduced with permission from ref. 171. Copyright 2024, Elsevier. (e) Illustration of the synthesis process for h-MoO_3/MoO_2@NC. (f) XRD patterns of MoO_3 and the h-MoO_3/MoO_2@NC nanocomposite. (g) HRTEM image of h-MoO_3/MoO_2@NC. (h) Cycling performances of the h-MoO_3/MoO_2@NC, MoO_3 and NC electrodes. Reproduced with permission from ref. 172. Copyright 2021, Elsevier. (i) SEM image and (j) TEM image of MoS_2@NC. (k) Long-term cycling performance of the MoS_2@NC electrodes. Reproduced with permission from ref. 173. Copyright 2023, Elsevier.

the cycle, improving material utilization and shortening the ion transmission distance. The outer flexible NC shell maintains the spherical structure of the electrode, inhibits agglomeration, and promotes the formation of a stable SEI layer. As shown in Fig. 8k, the material has been cycled for more than 10 000 cycles at a high current density of 20 A g^{-1}, and the capacity still reaches 428 mAh g^{-1}. The core–shell structure enhances the structural integrity and electronic conductivity and reduces the ion diffusion resistance through the synergistic mechanism of core structure reorganization and shell stability protection.

Research on W-based materials presents a dual-track breakthrough of component innovation and bio-templating. For example, Fu *et al.* used a step-by-step method to prepare laurel leaf-shaped Co_9S_8/WS_2@N doped carbon bimetallic sulfide (Co_9S_8/WS_2@NC) materials (Fig. 9a).[174] As shown in Fig. 9b and c, one can see the laurel leaf-shaped morphology of the Co_9S_8/WS_2@NC material and the corresponding crystalline phase. The synergistic structure of large interlayer spacing WS_2 and Co_9S_8 and the van der Waals force interface are used to inhibit WS_2 aggregation, buffer volume changes and improve the electron transfer efficiency. The charge and discharge capacities of the Co_9S_8/WS_2@NC anode are 510 and 406 mAh g^{-1}, respectively, and the initial coulombic efficiency is 79.6% (Fig. 9d). As the current density increases from 0.1 A g^{-1} to 5.0

A g^{-1}, it provides a practical capacity of 359 mAh g^{-1}, and the capacity retention rate is 78.0% (Fig. 9e). Kang *et al.* took advantage of the bio-template and confined a small amount of layered WSe_2 nanosheets in a composite material of N,P co-doped carbon (WSe_2/N,P-C-2) derived from *Chlorella* (Fig. 9f and g).[175] With the help of the bio-templating effect of *Chlorella*, the ultra-thin WSe_2 nanosheets were uniformly dispersed in N,P co-doped biochar (Fig. 9h), forming a high activity carbon matrix confined nanosheet structure, which effectively inhibited the agglomeration and volume expansion of WSe_2. As shown in Fig. 9i, the material has a good rate performance at different current densities, and has both wide applicability and ultra-stability. Besides, Liu *et al.* prepared Sn/N co-doped metallic phase tungsten selenide (1T-WSe_2-Sn) materials using chitosan as a precursor and nanoreactor through a simple calcination technique.[176] Sn doping induces WSe_2 to transform from the 2H phase into the highly conductive 1T phase, while expanding the interlayer spacing and promoting electron/ion transport (Fig. 9j). N doping and chitosan-derived carbon layers improve the structural stability and form a conductive active phase stable carbon matrix synergistic structure.

In summary, the heteroatom doping strategy provides a systematic solution to the sodium storage problem of Mo- and W-based anode materials through atomic-level electronic structure regulation and multi-scale performance optimization.

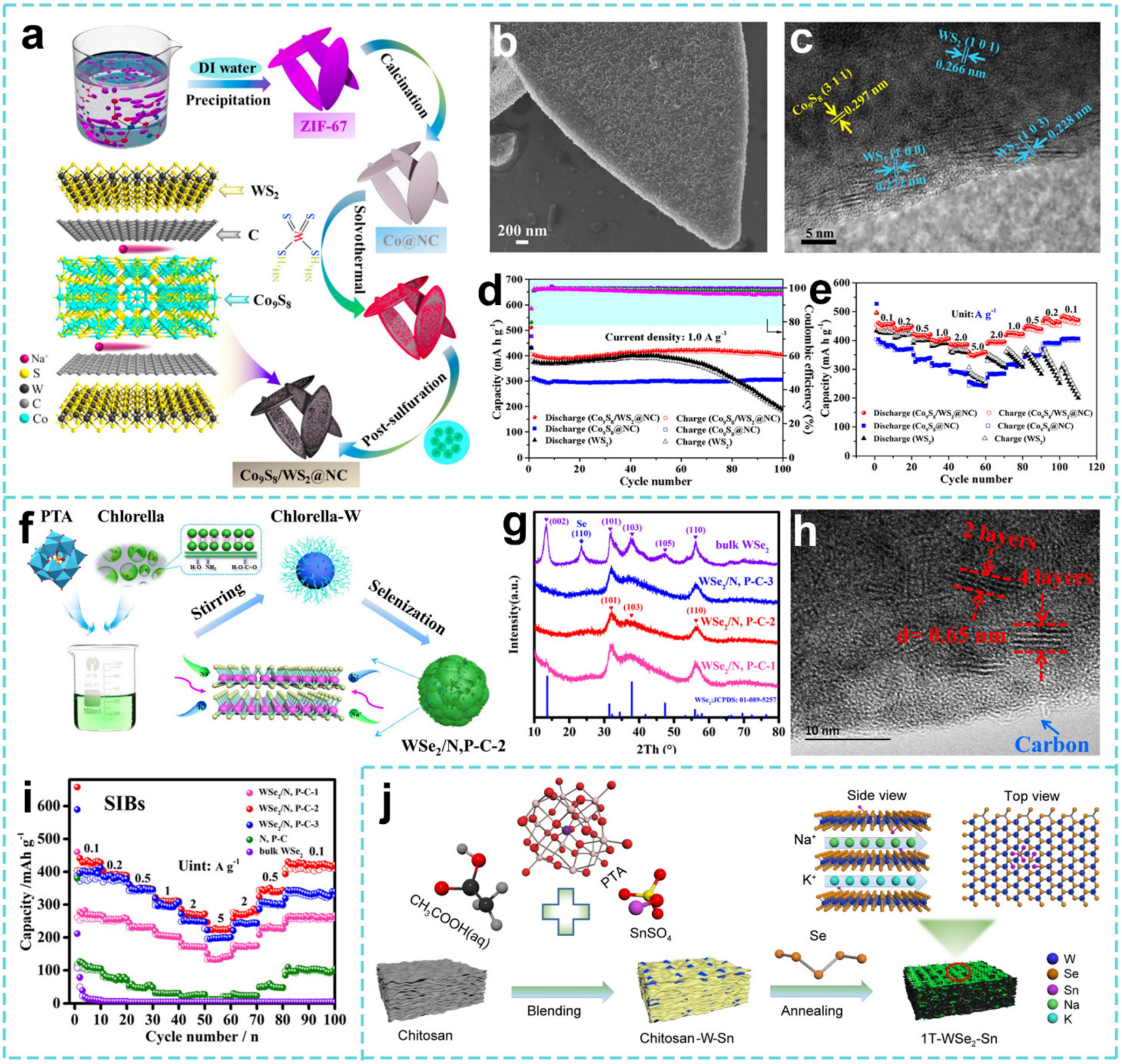

Fig. 9 (a) Illustration of the synthesis process, (b) SEM image and (c) HRTEM image of Co_9S_8/WS_2@N. (d) Cycling performance and (e) rate capability of the WS_2, Co_9S_8@NC, Co_9S_8/WS_2@NC electrodes. Reproduced with permission from ref. 174. Copyright 2021, Elsevier. (f) Schematic synthesis of the WSe_2/N,P-C-2 composite. (g) XRD patterns of WSe_2/N,P-C-1, WSe_2/N,P-C-2, WSe_2/N,P-C-3, bulk WSe_2. (h) HRTEM image of the WSe_2/N,P-C-2 composite. (i) The rate capability of electrodes at different current densities. Reproduced with permission from ref. 175. Copyright 2020, Elsevier. (j) Schematic illustration of the synthesis of the 1T-WSe_2-Sn composite. Reproduced with permission from ref. 176. Copyright 2023, Springer Nature.

From the dual improvement of electron conduction and interface stability by N doping, to the phase structure transformation and interlayer spacing expansion induced by Sn doping and the reaction mechanism innovation brought about by P doping, researchers have gradually constructed a synergistic modification system of electronic structure optimization, ion transport acceleration, and mechanical stress buffering through single heteroatom doping, multi-heteroatom co-doping and bio-template integration. These studies not only reveal the structure–activity relationship between doping elements and material properties, but also achieve a leap from basic performance optimization to the practical application potential of materials through the combination of green synthesis processes and structural engineering.

4.3.2 Heterojunction interface design. In the study of defect engineering, it has been explicitly stated that "lower defect densities help to improve the cycling stability and structural integrity of the battery, reducing structural breakdown caused by volume expansion". A moderately higher defect density (such as 10^6 defects per cm^2) can effectively facilitate charge transfer, improve the diffusion rate of electrons and ions, and enhance the power performance and rate capability of the battery.[177] However, when the defect density becomes too high, particularly above 10^7 defects per cm^2, it may lead to structural instability, increase the brittleness and decomposition risks of the material, and subsequently affect the long-term cycling stability and reliability of the battery. As a key optimization strategy, the heterojunction interface design constructs a composite interface between different components or phases to synergistically improve the material performance through three aspects: electronic structure regulation, ion transport acceleration and structural stability enhancement.[178] (1) At the electronic structure regulation level, the heterojunction can induce charge redistribution and optimize the band structure.[179] (2) Ion transport acceleration is another core advantage of heterojunction design. Lattice mismatch and interface defects between different materials can form abundant ion adsorption sites and shorten the Na^+ diffusion path.[180] (3) In terms of structural stability enhancement, the heterojunction uses physical confinement and chemical synergy to alleviate volume changes.[181] Furthermore, the design of the heterojunction interface plays a crucial role in controlling the ICE of the material. By constructing an internal electric field at the interface and optimizing charge distribution, the heterojunction can guide Na^+ to intercalate/deintercalate more uniformly and promote the formation of a more stable and thinner SEI. For example, in heterostructures such as MoS_2/WS_2, the electron redistribution at the interface can reduce the initial sodium ion intercalation barrier while suppressing excessive electrolyte decomposition on the active surface, thereby reducing irreversible sodium loss. By rationally selecting components, controlling the interface coupling strength, and combining surface modification, it is possible to effectively balance the first-cycle efficiency while leveraging the synergistic effect of the heterojunction, further improving the overall electrochemical performance of the material.[182]

Compared with 2H-MoS_2, 1T-MoS_2 is an attractive energy storage material due to its large interlayer spacing and excellent conductivity. The electron filling engineering of the Mo 4d orbital is the core idea to induce the efficient transformation of the 2H phase into the 1T phase. Based on this theory, Peng *et al.* successfully constructed uniform heterogeneous nanosheets (CuS@MoS_2) by coprecipitation and a hydrothermal method (Fig. 10a–c).[183] Electron-rich CuS acts as an electron donor, and part of the electrons at the heterogeneous interface are transferred from Cu to Mo, triggering rearrangement of the Mo 4d orbital and the formation of a strong built-in electric field at the interface, and causing the irreversible phase transition of MoS_2 from 2H to 1T (Fig. 10d). The practical capacity of CuS@MoS_2 remains at 464.18 mAh g^{-1} after 2700 cycles at a current density of 10 A g^{-1} (Fig. 10e). This work provides a new perspective for developing high-performance sodium storage anode materials based on 1T-rich MoS_2. On this basis, She *et al.* focused on the structural design of anode materials for SIBs and constructed a 3D porous hollow heterostructure (MXene@MoS_2) (Fig. 10f).[184] The 3D flower-like structure promotes electrolyte penetration by virtue of its high specific surface area and porous channels (Fig. 10g), effectively inhibits the self-aggregation of MoS_2 and buffers the volume expansion, while the solid heterogeneous interface formed by MXene and MoS_2 accelerates electron transfer (Fig. 10h). Thus, the practical capacity of MXene@MoS_2 remains at 494.4 mAh g^{-1} after 1000 cycles at 5 A g^{-1} (Fig. 10i). This study reveals the influence of the electrode material structure on the sodium storage mechanism through the strategy of template construction of the 3D structure and heterogeneous composite formation. Following the research context of structural optimization and interface regulation, Zhao *et al.* designed and prepared a composite material of layered MoS_2/WS_2 heterostructure nanostructures (HC@MoS_2/WS_2@NC) coated with double carbon layers to address the challenges of insufficient reaction kinetics and large volume changes (Fig. 10j).[185] The double carbon constrained structure of the internal hard carbon core and the external nitrogen-doped carbon shell is used to anchor MoS_2/WS_2 to inhibit volume expansion, while the high conductivity of the double carbon layer is used to accelerate electron transport (Fig. 10k). Therefore, the HC@MoS_2/WS_2@NC material maintains a practical capacity of 333 mAh g^{-1} after 1000 cycles at 2 A g^{-1} (Fig. 10l and m).

In summary, heterogeneous interface design has established a 3D performance improvement path of electronic structure optimization, ion transport acceleration, and structural stability enhancement for Mo- and W-based anode materials through a multi-dimensional synergistic mechanism across components and scales (Table 2). From the charge transfer regulation of two-component heterojunctions to the interface engineering innovation of 3D porous structures and core–shell composite systems, this strategy not only reveals the intrinsic relationship between interface effects and sodium storage performance, but also achieves precise control from atomic-level interface regulation to macroscopic structural design through preparation techniques such as the template method and

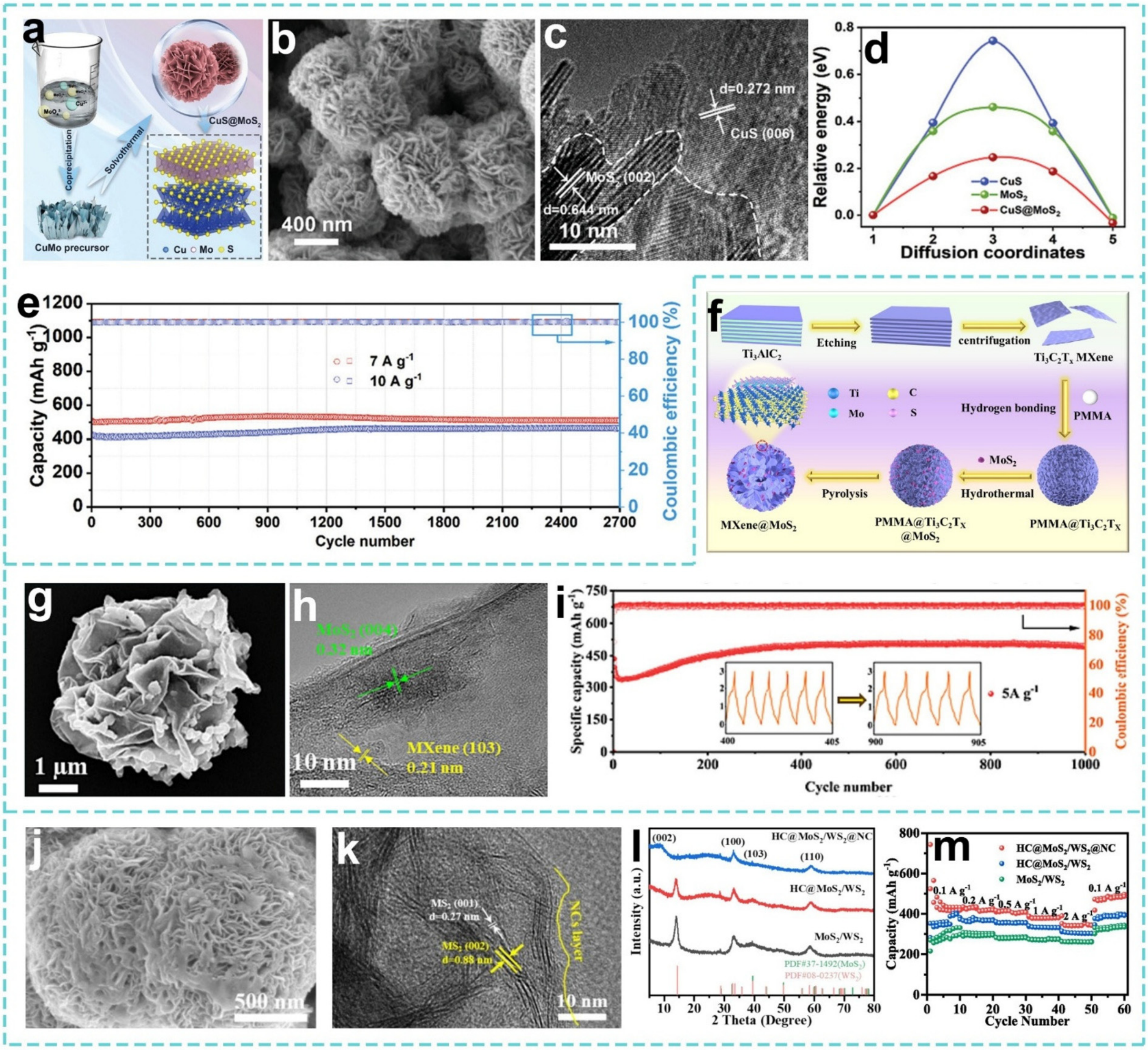

Fig. 10 (a) Preparation process for the CuS@MoS$_2$ heterostructure. (b) SEM image and (c) HRTEM image of CuS@MoS$_2$. (d) Diffusion energy barriers of Na$^+$ in CuS, MoS$_2$, and CuS@MoS$_2$. (e) Long-term cycling performance of CuS@MoS$_2$. Reproduced with permission from ref. 183. Copyright 2025, Wiley. (f) Illustration of the synthesis process, (g) SEM image and (h) HRTEM image of MXene@MoS$_2$. (i) Long cycling performance of the MXene@MoS$_2$ electrode. Reproduced with permission from ref. 184. Copyright 2024, Elsevier. (j) SEM image and (k) HRTEM image of HC@MoS$_2$/WS$_2$@NC. (l) XRD patterns of MoS$_2$/WS$_2$, HC@MoS$_2$/WS$_2$, and HC@MoS$_2$/WS$_2$@NC. (m) Rate capability of MoS$_2$/WS$_2$, HC@MoS$_2$/WS$_2$, and HC@MoS$_2$/WS$_2$@NC at different current densities. Reproduced with permission from ref. 185. Copyright 2024, Elsevier.

in situ growth. In general, heterojunction interface engineering provides an effective approach to simultaneously tune the electronic structure, accelerate Na$^+$ transport, and enhance the structural stability of Mo- and W-based anode materials. However, the complexity of their structure and composition also poses challenges for engineering feasibility. Multi-component heterostructures typically require precise control over the phase composition, interfacial contact, and spatial distribution of active regions, making their synthesis conditions sensitive and difficult to scale up.[186] Furthermore, long-term interfacial stability under repeated sodiation/desodiation cycles remains a critical issue, especially when different components exhibit mismatched mechanical or electrochemical behavior. Therefore, future heterojunction engineering should focus on the systematic evaluation of simplified structures and scalable synthesis methods to ensure that the inherent advantages of interface tuning can be effectively translated into practically viable anode materials for SIBs.

5. Research progress on Mo- and W-based materials in SIB anodes

5.1 Mo-/W-based oxides

Metal oxides have attracted much attention in research on anode materials for SIBs due to their high theoretical specific

Table 2 Comparison of the electrochemical performance of Mo- and W-based materials in SIBs

Materials	Cathode material	Current density (A g^{-1})	Capacity retention (mAh g^{-1})	ICE (half/full)	Capacity retention (%)/cycles	Ref.
MoS_2@CPDs-2	$Na_3V_2(PO_4)_3F_3$	0.5	472.4	82.3% (full)	62.5/500	146
MoS_2/MWCNT	—	0.1	527.7	67.5% (half)	100.0/110	147
NCF@V-MoS_2	—	1.0	413.0	64.8% (half)	—/300	148
NGQDs-WS_2/3DCF	$Na_{0.44}MnO_2$	2.0	268.4	65.1% (half)	97.1/1000	150
M-MoS_2@HCS	—	0.1	401.3	34.6% (half)	—/100	157
MoS_2/C	$Na_3Fe_2(PO_4)_3$	1.0	515.8	88.7% (full)	94.3/1000	158
NSC@WS_2	—	5.0	234.8	71.2% (half)	51.2/900	159
$MoSe_2/Mo_2CT_x$/C	—	2.0	238.4	47.3% (half)	86.3/2200	163
$MoSe_2$@Mo_xN/C-I	—	20.0	178.6	42.9% (half)	98.8/10 000	164
$WSSe_2$/C-1	AC	1.0	715.3	56.4% (full)	70.1/200	165
H-MoO_3/MoO_2@NC	—	0.5	190.0	38.9% (half)	38.9/5000	172
MoS_2@NC	$Na_3V_2(PO_4)_3$	20.0	428.0	64% (full)	98.7/10 000	173
Co_9S_8/WS_2@N	—	5.0	359.0	81.7% (half)	78.0/120	174
WSe_2/N,P-C-2	$Na_3V_2(PO_4)_3$	1.0	155.0	59% (full)	—/5300	175
CuS@MoS_2	$Na_3V_2(PO_4)_3$	5.0	506.0	78% (full)	98.2/3200	183
MXene@MoS_2	$Na_3V_2(PO_4)_3$/C	5.0	494.4	78.2% (full)	79.9/1000	184
HC@MoS_2/WS_2@C	$Na_3V_2(PO_4)_3$	2.0	333.0	64% (full)	39.8/1000	185

capacity. Among them, Mo- and W-based oxides, as potential anode materials, exhibit unique physical and chemical properties and are expected to provide new solutions for improving the performance of SIBs.[187] Mo-based oxide has a variety of oxidation states, such as MoO_2, MoO_3, *etc*. Its crystal structure and electronic structure enable it to undergo reversible redox reactions during the insertion and de-insertion of Na^+, thereby achieving charge storage.[188] W-based oxides, such as WO_3, WO_2, *etc*., also have rich crystal structures and chemical properties and show potential application value in the field of energy storage. Through the structural design, morphology control and compounding of Mo/W oxides with other materials, their electrochemical properties can be further optimized to improve the energy density, cycle life and rate performance of SIBs.

5.1.1 **MoO_2 and WO_2.** MoO_2 and WO_2 have attracted much attention as anode materials for SIBs in recent years, showing a high theoretical specific capacity and rich sodium storage mechanisms. Their redox properties and unique crystal structures provide abundant active sites for the reversible insertion/extraction of sodium ions. For example, Zhang *et al.* synthesized MoO_2 nanoparticles by a simple hydrothermal reaction and further applied them to SIB anode materials (Fig. 11a).[189] This study verified that the vinyl acetate (VC) additive could affect the film formation mechanism of the MoO_2 anode in SIBs and improve its cycling stability. Specifically, the capacity retention rate increased from 20.1% to 96.5% after 1000 cycles at 0.3 A g^{-1} (Fig. 11b and c). The average mass loading of MoO_2 in the electrode was 1.02 mg cm^{-2}, and $NaPF_6$ was used as the electrolyte, which provided some reference for the ratio of electrode active material to conductive agent (E : C). Similarly, Li *et al.* constructed amorphous/crystalline MoO_2 (a/c-MoO_2) homojunction materials with multiple interfaces and defects in the a/c-MoO_2 nanoclusters by a one-pot solvothermal method.[190] Theoretical simulations show that electrons are redistributed at the uniform interface of a/c-MoO_2 to form a built-in electric field effect, which can significantly improve the adsorption capacity of Na^+ and reduce the diffusion energy barrier, promote the intercalation/deintercalation of Na^+ in the material and improve the cycling stability. As a result, a/c-MoO_2 achieves a practical capacity of 307 mAh g^{-1} at 0.1 A g^{-1}, and can achieve 3000 stable cycles (Fig. 11d and e). At the same time, the *in situ* X-ray diffraction (XRD) test reveals its "adsorption–embedding–conversion" sodium storage mechanism (Fig. 11f). Based on the improvement in the performance of SIBs by interface defects, Zhou *et al.* designed a heterojunction material with a carbon-free layered structure (MoS_2/MoO_2).[191] The HRTEM image confirms that the hybridization between MoS_2 and MoO_2 forms a large amount of heterogeneous interfaces (Fig. 11g). In addition, the heterojunction enhances the Na^+ adsorption energy and reduces the Na^+ diffusion energy barrier, promoting efficient ion transport (Fig. 11h). Thus, the capacity of MoS_2/MoO_2 is maintained at almost 100% after 100 cycles at 1 A g^{-1} (Fig. 11i).

Compared with MoO_2 materials, WO_2 also has good application potential in SIB anode materials. For example, Xu *et al.* constructed a porous WO_2/WS_2-reduced graphene oxide (WO_2/WS_2–rGO) hetero-composite anode and P-doped biomass carbon cathode by a hydrothermal method combined with freeze drying and calcination processes.[192] They also optimized the Na^+ diffusion kinetics through heterogeneous interface synergy and 3D porous design, providing new ideas for low-cost, high-performance energy storage devices. As anode materials for SIBs, MoO_2 and WO_2 have made significant progress in structural design, interface engineering and electrolyte optimization. Through strategies such as nanostructuring, heterostructure construction, element doping and crystal surface regulation, the electron transport, ion diffusion and structural stability of the materials have been effectively improved. This will provide an important theoretical basis and technical inspiration for the development of high energy density and long life SIBs.

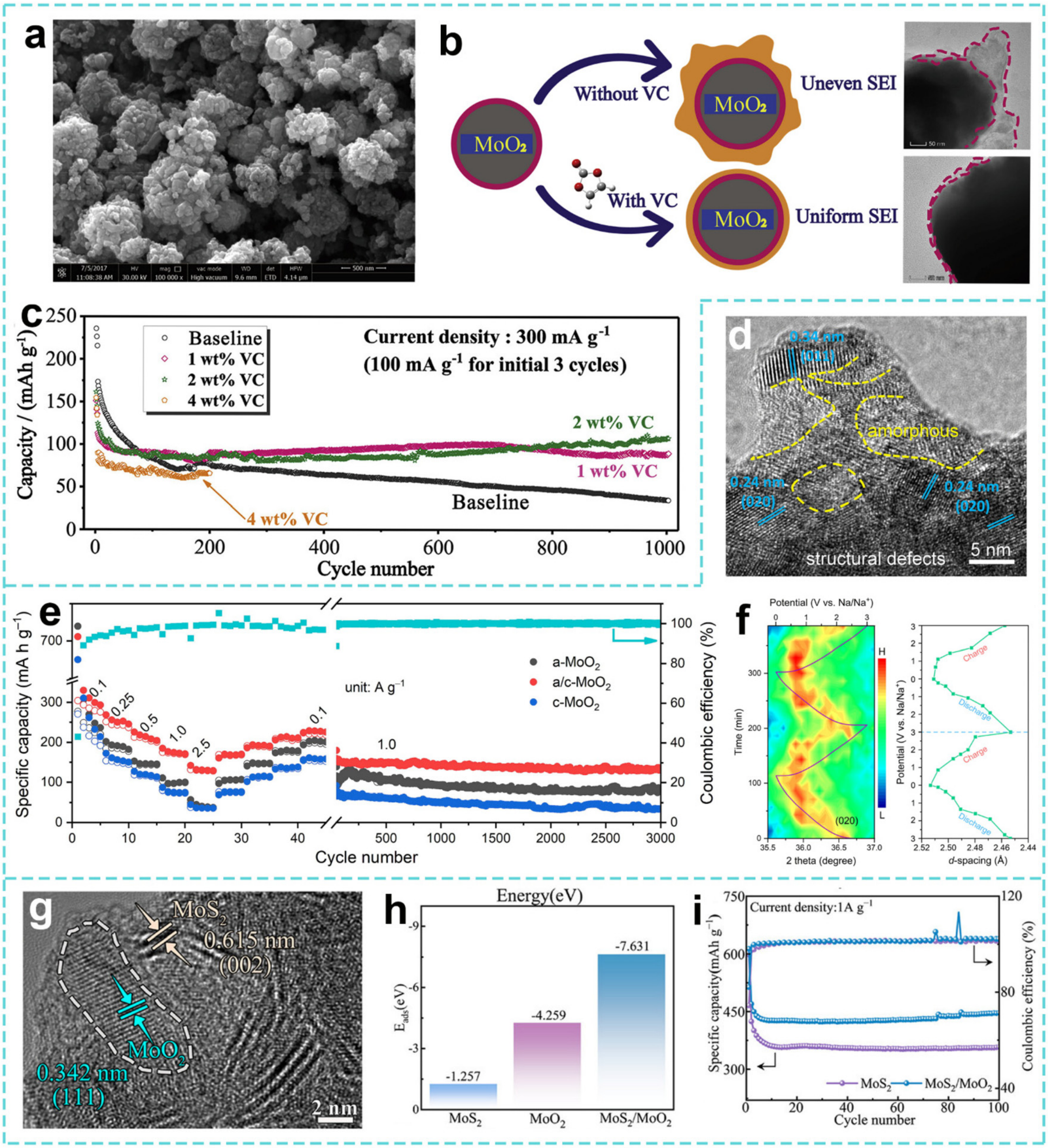

Fig. 11 (a) SEM image of MoO_2 powders. (b) Corresponding schematic illustration and TEM images of the MoO_2 electrodes after 1000 cycles with baseline electrolyte and 2 wt% VC-containing electrolyte. (c) Comparison of the cycling stability of the MoO_2 electrodes without and with VC additive. Reproduced with permission from ref. 189. Copyright 2020, Elsevier. (d) HRTEM image of a/c-MoO_2. (e) Rate and cycling performance of the MoO_2 electrodes. (f) Contour plot of the (020) peak evolution with the corresponding discharge–charge profiles in the initial two cycles and $d_{(020)}$-spacing change as a function of applied potential. Reproduced with permission from ref. 190. Copyright 2023, Elsevier. (g) HRTEM image of MoS_2/MoO_2. (h) Calculated Na^+ ion adsorption energy of MoO_2, MoS_2, and MoS_2/MoO_2. (i) Cycling performance of MoS_2/MoO_2. Reproduced with permission from ref. 191. Copyright 2025, Wiley.

5.1.2 MoO_3 and WO_3.

MoO_3 and WO_3 have become the research focus in the field of anode materials due to their unique crystal structures and redox properties.[193] MoO_3 is an environmentally friendly and low-cost anode material that can provide a high capacity through insertion and conversion reactions.[194] More importantly, the layered structure of MoO_3 provides insertion sites and Na^+ diffusion channels, which significantly improve the electrochemical performance.[195] Meanwhile, WO_3 enhances the Na^+ storage capacity and cycling stability through porous structure design and defect regulation.

As an anode material for SIBs, MoO_3 has made significant progress in recent years through multidimensional structural engineering strategies. Different researchers have collaboratively solved bottleneck problems such as poor conductivity, severe volume expansion and insufficient cycling stability from different angles. From the perspective of interlayer engineering, Wang *et al.* developed a two-step synthesis strategy based on partial reduction and organic molecular intercalation.[196] By introducing bismuth thiol (DMcT) molecular intercalation, the interlayer spacing of MoO_3 was extended from 6.92 Å to 10.40 Å (Fig. 12a), significantly improving the diffusion kinetics of Na^+. This DMcT-MoO_3 structure not only reduces the charge transfer resistance, but also enhances the interlayer stability through intermolecular forces (Fig. 12b and c), thereby improving the Na^+ insertion–extraction kinetics. Furthermore, it has a long cycling stability and high rate performance (Fig. 12d). On this basis, Yang *et al.* further optimized the material structure through a nano-sizing strategy. As shown in Fig. 12e, the layered MoO_3 nanoplates (MoO_3 NPs) were prepared by pyrolysis of Mo-based metal organic frameworks, the unique 2D nanostructure of which effectively alleviated volume expansion during the charging and discharging process. Thanks to the shortened ion diffusion path and exposed active sites, the material maintained a practical capacity of 154 mAh g^{-1} after 1200 cycles at 50 mA g^{-1} (Fig. 12f).[197] This nano-design approach complements interlayer engineering and jointly solves the problem of structural stability. In terms of mass loading, the MoO_3 electrode in the assembled coin cell reportedly had a mass loading of 1–2 mg cm^{-2}, and the electrolyte was $NaClO_4$ in a 1 : 1 mixture of ethylene carbonate (EC) and diethyl carbonate (DEC). To further improve the electrochemical kinetics, Yu *et al.* synthesized a nanorod-shaped MoO_3–MoS_2 heterostructure by a two-step method (Fig. 12g). The built-in electric field of the heterojunction formed by interface engineering significantly accelerated charge transfer, allowing the material to maintain a practical capacity of 316 mAh g^{-1} at an ultra-high current density of 10 A g^{-1}, and still maintain a practical capacity of 286 mAh g^{-1} after 2300 cycles at 5 A g^{-1}. *In situ* XRD revealed that the high specific capacity of MoO_3–MoS_2 was attributed to the synergistic energy storage mechanism between the intercalation reaction of MoO_3 and the conversion reaction of MoS_2 (Fig. 12h and i). Additionally, the study reported a mass loading of 5.47 mg cm^{-2} for the MoO_3–MoS_2 electrodes prepared *via* 3D printing technology, demonstrating that the areal capacity increased with the mass loading, reaching up to 5.47 mg cm^{-2}.[198]

These studies have systematically improved the sodium storage performance of MoO_3-based anode materials through multi-dimensional innovations such as interlayer regulation, nanostructure design, heterogeneous interface engineering, morphology optimization and composite strategies. From the basic interlayer expansion to macroscopic structure design, and from single material optimization to multi-component synergy, it demonstrates the strong vitality of material engineering strategies in solving key material problems of SIBs, and provides an important technical route for the subsequent development of high-performance energy storage devices.

Unlike the rich layered structure of MoO_3, WO_3 has great application potential in the anode materials of SIBs because of its controllable porous structure and defects. García-García *et al.* prepared a WO_3 film with a porous nanocolumn structure, the unique pores and surface properties of which significantly improved the Na^+ diffusion efficiency and storage capacity. The separated nanocolumns and large number of pores allow Na^+ to penetrate deeply and evenly into the film, improving the cycling stability of the material.[199] Inspired by this, Zimmer *et al.* tried to make further breakthroughs from the structural dimension. They synthesized hollow WO_3 microspheres constructed by self-assembling interconnected nanosheets through a hydrothermal method. Their unique interconnected hollow structure provided abundant active sites and volume expansion buffer space, achieving a high reversible capacity of 431 mAh g^{-1} at 100 mA g^{-1}. The practical capacity recovered to 220 mAh g^{-1} after cycling, significantly optimizing the sodium ion diffusion kinetics and cycling stability.[200]

MoO_3- and WO_3-based materials have significantly optimized the sodium storage kinetics and cycling stability through interlayer engineering, heterogeneous structure design (such as MoO_3–MoS_2 interface electric field) and multidimensional composite systems (such as vertical nanosheet arrays and 3D hollow microspheres). This will be key in structural innovation and mechanistic exploration, providing theoretical support and technical pathways for the development of the next generation of low-cost, high-safety SIBs.

5.2 Mo-/W-based chalcogenides

Mo- and W-based chalcogenides typically possess a layered structure, with weak van der Waals forces between the layers, facilitating the intercalation and deintercalation of Na^+, thereby enabling charge storage and release. Furthermore, Mo- and W-based chalcogenides exhibit multi-electron reaction activity, offering higher theoretical specific capacities. For example, MoS_2 boasts a theoretical capacity of up to 670 mAh g^{-1}, significantly higher than that of traditional graphite anode materials. Moreover, their electronic structure can be optimized by tuning their structure and composition, thereby improving the electrochemical performance and cycle life. Introducing defects, doping with other heteroatoms, or compositing with carbon-based materials can further enhance the conductivity and structural stability of these materials.[201] In SIBs, the electrolyte plays a crucial role in the stability and performance of Mo- and W-based anodes. Compared to carbonate-based electrolytes, ether-based electrolytes generally exhibit better compatibility with Mo- and W-based layered sulfides and selenides. Ether solvents can form a more stable SEI layer on the surface of Mo- and W-based materials, protecting the anode during cycling and minimizing side reactions. However, the oxidative stability of ether-based electrolytes at high voltages remains a concern, as they are prone to decomposition under extreme conditions, potentially leading to undesirable side reactions. On the other hand, commonly used carbonate-based electrolytes also have limitations when paired with Mo- and W-based materials. While they tend to form a more stable and robust SEI layer, the high reactivity of unsaturated active sites on the Mo- and W-based surface with carbonate solvents

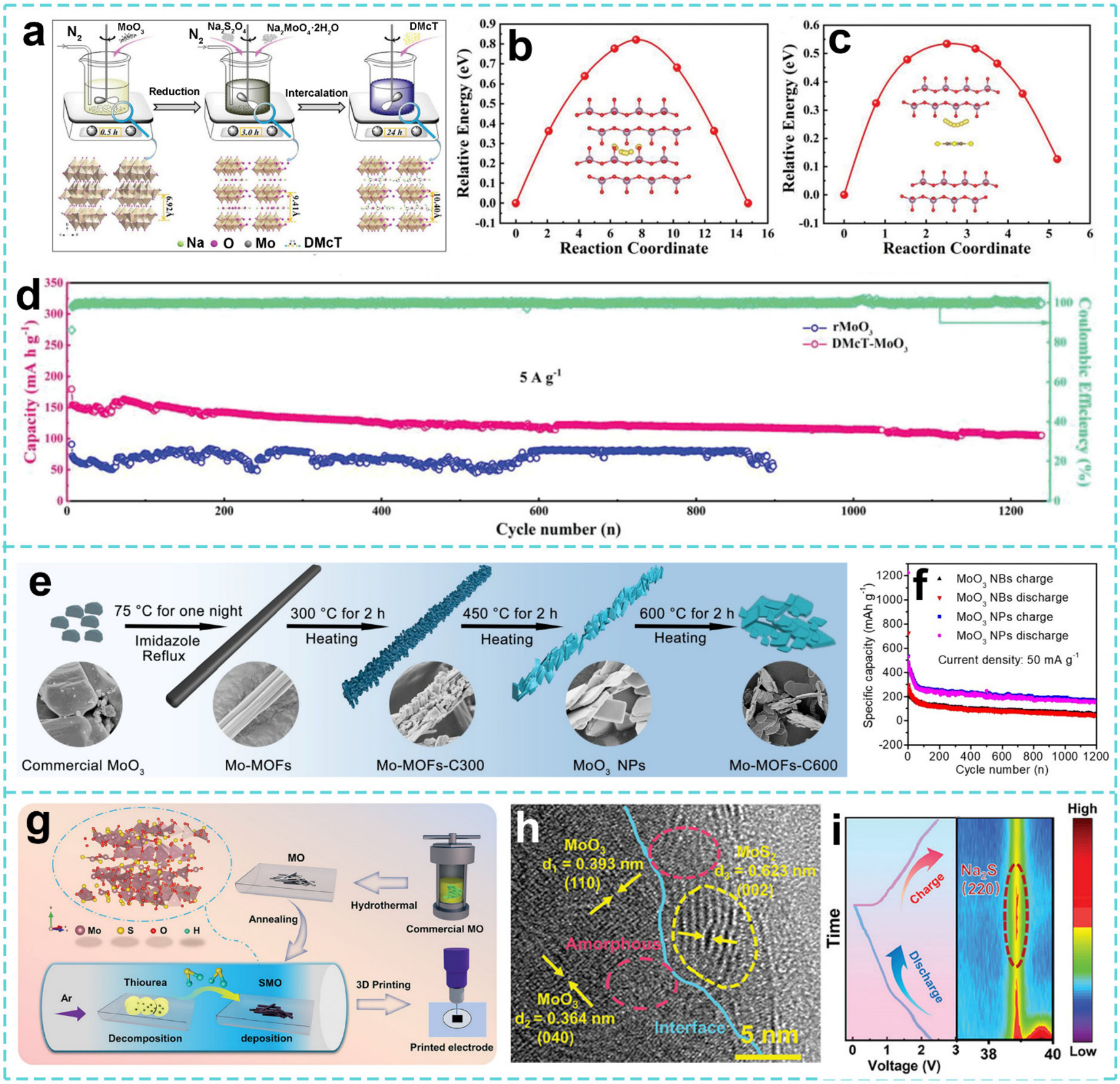

Fig. 12 (a) Illustration of the synthesis process for DMcT-MoO_3. Diffusion pathways and diffusion barriers of Na shuttles between (b) MoO_3 and (c) DMcT-MoO_3. (d) Long cycling performances of the rMoO_3 and DMcT-MoO_3 electrodes. Reproduced with permission from ref. 196. Copyright 2020, Wiley. (e) Diagram of the MoO_3 NP synthesis process with increasing temperature. (f) Cycling performance of MoO_3 NBs and MoO_3 NPs at 50 mA g^{-1}. Reproduced with permission from ref. 197. Copyright 2020, Springer Nature. (g) Illustration of the synthesis process, (h) HRTEM image of MoO_3–MoS_2. (i) *In situ* XRD evolution profiles of the MoO_3–MoS_2 electrode for the 1st discharge–charge process at 0.1 A g^{-1}. Reproduced with permission from ref. 198. Copyright 2024, Wiley.

leads to significant decomposition and the formation of gaseous byproducts, such as CO_2 and CO. These byproducts not only increase internal resistance but also degrade the SEI layer, exacerbating capacity fading and shortening the cycle life.[202] To improve the compatibility of electrolytes with Mo- and W-based anodes, future research should focus on developing electrolyte systems that are better matched to the unique surface chemistry and structural characteristics of these materials. This may include exploring novel high-concentration electrolytes to reduce side reactions and enhance SEI stability, as well as optimizing solvent selection to improve their oxidative stability at high voltages. Furthermore, solid-state electrolytes possess excellent chemical stability and minimal side reactions, offering a promising solution to address electrolyte compatibility issues. They can provide a stable interface, thereby improving the overall performance and lifespan of Mo- and W-based anodes in SIBs.

5.2.1 MoS_2 and WS_2.

As 2D layered transition metal sulfides, MoS_2 and WS_2 have great potential in the field of anode materials for SIBs due to their unique crystal structures and physicochemical properties.[203] Their layered structure is conducive to the intercalation/deintercalation of Na^+, and the rich surface sites provide conditions for sodium storage.[204] In phase engineering, MoS_2 has two typical phase structures, 1T and 2H. The 2H phase is semiconducting in nature, with a stable structure but low conductivity, while the 1T phase is metallic and has excellent electronic conductivity.[106,205] The characteristic differences between the 1T and 2H phases and the heterogeneous structure design can optimize electron transport and sodium storage activity, and interlayer spacing regulation can improve the sodium storage efficiency and enhance structural stability through ion intercalation and other means.[206]

Interlayer spacing regulation provides the basic conditions for Na^+ transport and storage. Therefore, Tao *et al.* focused on optimizing the interlayer spacing of MoS_2 by ion intercalation, and used density functional theory simulations to determine the ideal spacing range of 0.80 to 1.01 nm (Fig. 13a). At the same time, by regulating the mass ratio of 1-butyl-3-methylimidazolium acetate ([BMIm]Ac) ionic liquid to cellulose, the controllable intercalation of cellulose oligomers was achieved, and then porous carbon-supported interlayer expanded MoS_2 was synthesized. As shown in Fig. 13b and c, this structure not only reduces the diffusion barrier of Na^+ and shortens the Na^+ diffusion path, but also limits the loss of sulfur in the cycle through the carbon matrix, thereby improving the cycle life, so that the material still maintains a practical capacity of 517.79 mAh g^{-1} after 250 cycles at 0.1 A g^{-1}, highlighting the

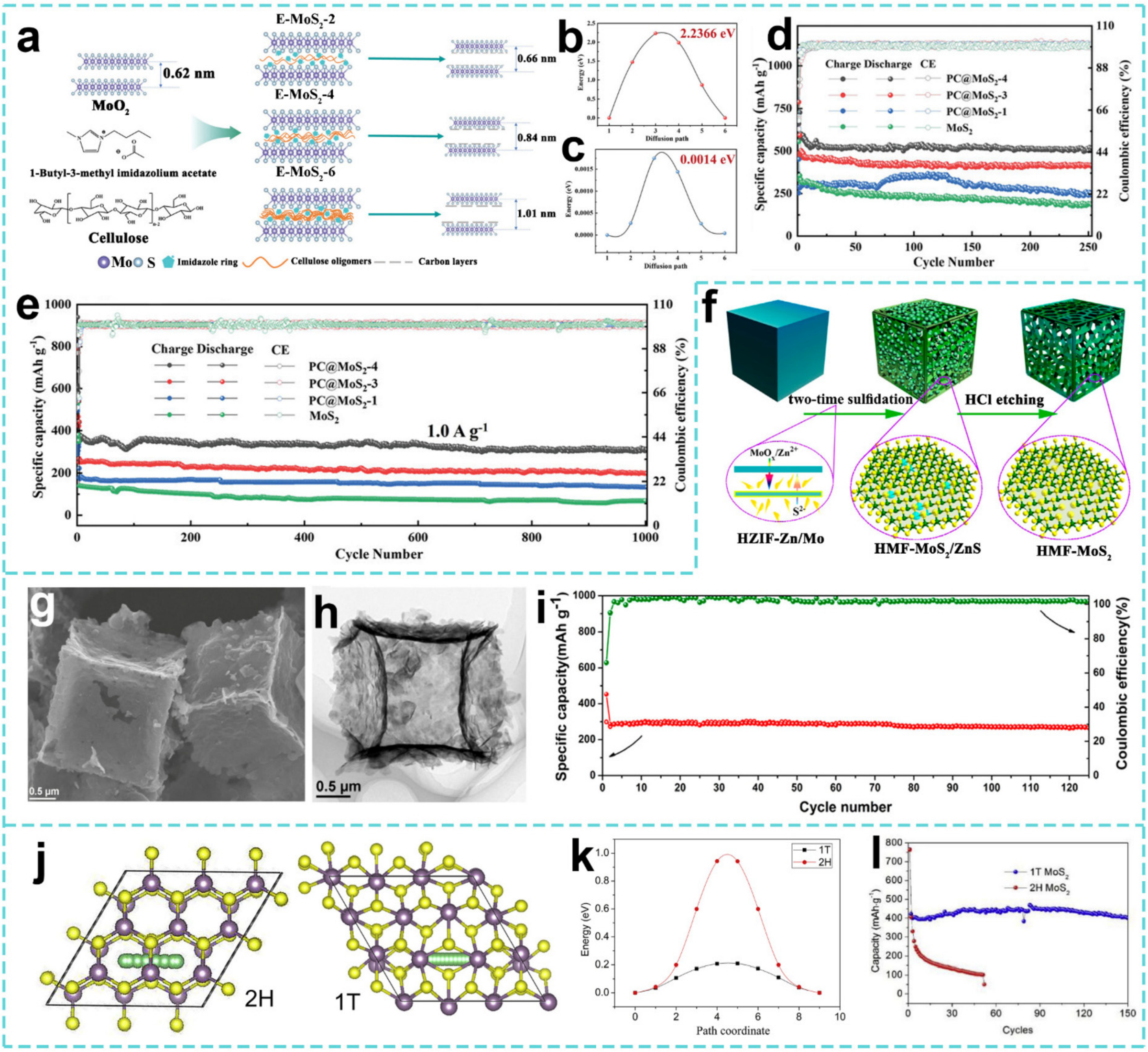

Fig. 13 (a) Schematic illustration of the formation of different MoS_2 interlayer distances. Migration energy barrier of (b) 0.62 nm and (c) 1.01 nm interlayer distances of MoS_2. Cycling performances of PC@MoS_2-4, PC@MoS_2-3, PC@MoS_2-1, and MoS_2 at (d) 0.1 A g^{-1} and (e) 1 A g^{-1}. Reproduced with permission from ref. 207. Copyright 2023, Wiley. (f) Schematic illustration of the formation of HMF-MoS_2. (g) SEM image and (h) TEM image of HMF-MoS_2. (i) Cycling performance of HMF-MoS_2 at 1 A g^{-1}. Reproduced with permission from ref. 209. Copyright 2019, American Chemical Society. (j) Corresponding crystal structures and (k) Na atom diffusion barriers of 2H and 1T MoS_2. (l) Cycling performance of 2H and 1T MoS_2 at 0.1 A g^{-1}. Reproduced with permission from ref. 210. Copyright 2019, Elsevier.

dual improvement of interlayer spacing optimization on sodium storage efficiency and structural stability (Fig. 13d and e).[207] Based on the regulation of interlayer spacing, electronic structure optimization has become a key extension to improve the sodium storage activity. Fan *et al.* optimized the electronic structure by replacing atomic elements within the MoS_2 layer, thereby changing its inherent physical properties. By reducing the band gap, the surface Na^+ adsorption energy and electronic conductivity were enhanced, thereby effectively optimizing the electrochemical performance of sodium storage.[208] Defect engineering breaks through the performance bottleneck of traditional structures at the atomic scale. As shown in Fig. 13f, Li *et al.* developed a hollow micro-cubic framework constructed of ultra-thin MoS_2 nanosheets (HMF-MoS_2) rich in molybdenum defects through a zeolite-like framework-driven strategy. The hollow micro-cubic framework can be clearly seen from the SEM and TEM images in Fig. 13g and h. This structure has a good practical capacity of 267 mAh g^{-1} after 125 cycles at a current density of 1 A g^{-1} (Fig. 13i).[209] The abundant Mo vacancies in MoS_2 can accelerate charge transfer and enhance the interaction between MoS_2 and Na^+, thereby promoting sodium storage. Sun *et al.* successfully prepared 1T phase ultrathin MoS_2 nanosheets (1T MoS_2) from 2H MoS_2 by thermally driven sodium ion insertion assisted exfoliation. Compared with 2H MoS_2, 1T MoS_2 has a lower Na^+ diffusion barrier, higher electronic conductivity, atomic mobility, and sodium affinity, as well as inhibiting the release of sulfur species and reducing phase changes during sodiation (Fig. 13j and k). Its capacity retention rate after 200 cycles at 1 A g^{-1} is as high as 94%, and it has good cycling stability (Fig. 13l).[210]

Similarly, in order to optimize the structural stability and electrochemical performance of WS_2 in the anode material of SIBs, researchers have made important progress through innovative material design strategies. They conducted research from the dimensions of structural regulation, interface engineering and composite system construction, and gradually formed a technical path of multi-dimensional synergistic strengthening. Choi *et al.* prepared 3D reduced graphene oxide microspheres modified with layered WS_2 nanosheets (WS_2-3D rGO) by a two-step method of spray pyrolysis combined with sulfurization. In this design, the 3D rGO skeleton not only effectively inhibits the stacking of WS_2 nanosheets, but also provides a buffer space for volume expansion during the intercalation/deintercalation of Na^+, giving full play to the synergistic advantages of the high theoretical capacity of WS_2 and the high conductivity of graphene.[211] However, WS_2 obtained by traditional chemical stripping still faced the problem of limited interlayer stripping efficiency, which prompted researchers to explore more efficient stripping techniques. Zhang *et al.* developed a molten salt electrolytic stripping method (Fig. 14a), using Na^+ to uniformly intercalate WS_2 under an electric field, and they successfully prepared a material with a few-layer lamellar structure (WS_2–NaCl) (Fig. 14b). By optimizing the molten salt system and electrolysis parameters, the obtained WS_2–NaCl-25 mA electrode still maintained a reversible capacity of 373 mAh g^{-1} after 100 cycles at 0.1 A g^{-1}, and also showed a good cycling performance and rate performance. The mass loading of the WS_2 material used as the anode in the SIB was 1.5 mg cm^{-2}, and the electrolyte used was a $NaClO_4$ solution dissolved in propylene carbonate (PC) with the addition of 5% fluoroethylene carbonate (FEC) (Fig. 14c).[212] In terms of structural engineering, Lin *et al.* developed a different approach for constructing a hollow bimetallic heterojunction WS_2@MnS material. Fig. 14d shows different views of the simulation model before and after Na^+ insertion into the structure. WS_2@MnS has a much lower Na^+ diffusion energy than pure WS_2 due to its unique heterostructure preparation; this successfully demonstrates that the construction of a functional heterostructure is beneficial for Na^+ diffusion kinetics. The designed hollow structure both relieves cycling stress and increases the specific surface area (Fig. 14e). As shown in Fig. 14f, this synergistic effect enables the material to achieve 2000 ultra-long cycles at 0.1 A g^{-1}.[213] It is worth noting that the above-mentioned powder electrode materials still face the cumulative effect of volume expansion. For this reason, the Dey team pioneered the embedding of WS_2 nanotubes (WS_2NTs) into the (SiOC) ceramic fiber matrix. The 3D ceramic fiber network prepared by electrospinning combined with high-temperature pyrolysis not only effectively inhibited volume change to the WS_2 nanotubes, but also blocked the dissolution of polysulfides through the chemical stability of the carbon oxide carbide matrix.[214]

From the above research, although MoS_2 and WS_2 materials have application potential in SIBs, there are problems such as structural degradation, kinetic sluggishness and side reactions. Researchers achieved performance breakthroughs through in multi-scale modification strategies: (1) at the microscopic level, the interlayer spacing was precisely controlled with the help of DFT calculations, and the diffusion kinetics and electronic structure were optimized by combining ionic liquid intercalation technology and element substitution. (2) At the mesoscopic and macroscopic scales, hollow microcubic frameworks containing molybdenum vacancies and 1T/2H heterogeneous phase coral reef-like structures were constructed, and defect engineering and special structural design were used to provide sodium storage sites and alleviate volume expansion. At the same time, 3D graphene was composited and a conductive network was constructed by molten salt stripping to improve the conductivity and structural stability. These studies have solved material application problems from different angles and provided important technical references for the development of high-performance SIBs.

5.2.2 $MoSe_2$ and WSe_2.

As a typical type of transition metal selenide, $MoSe_2$ and WSe_2 have shown significant advantages in the field of anode materials for SIBs due to their unique layered crystal structures and adjustable electronic properties. The weaker van der Waals forces between the layers provide a natural channel for the reversible intercalation/deintercalation of Na^+, and the larger interlayer spacing is more conducive to the diffusion of Na^+ than sulfides, reducing the embedding energy barrier.[215] $MoSe_2$ and WSe_2 have multiple crystal phases, among which the metallic 1T phase has excellent elec-

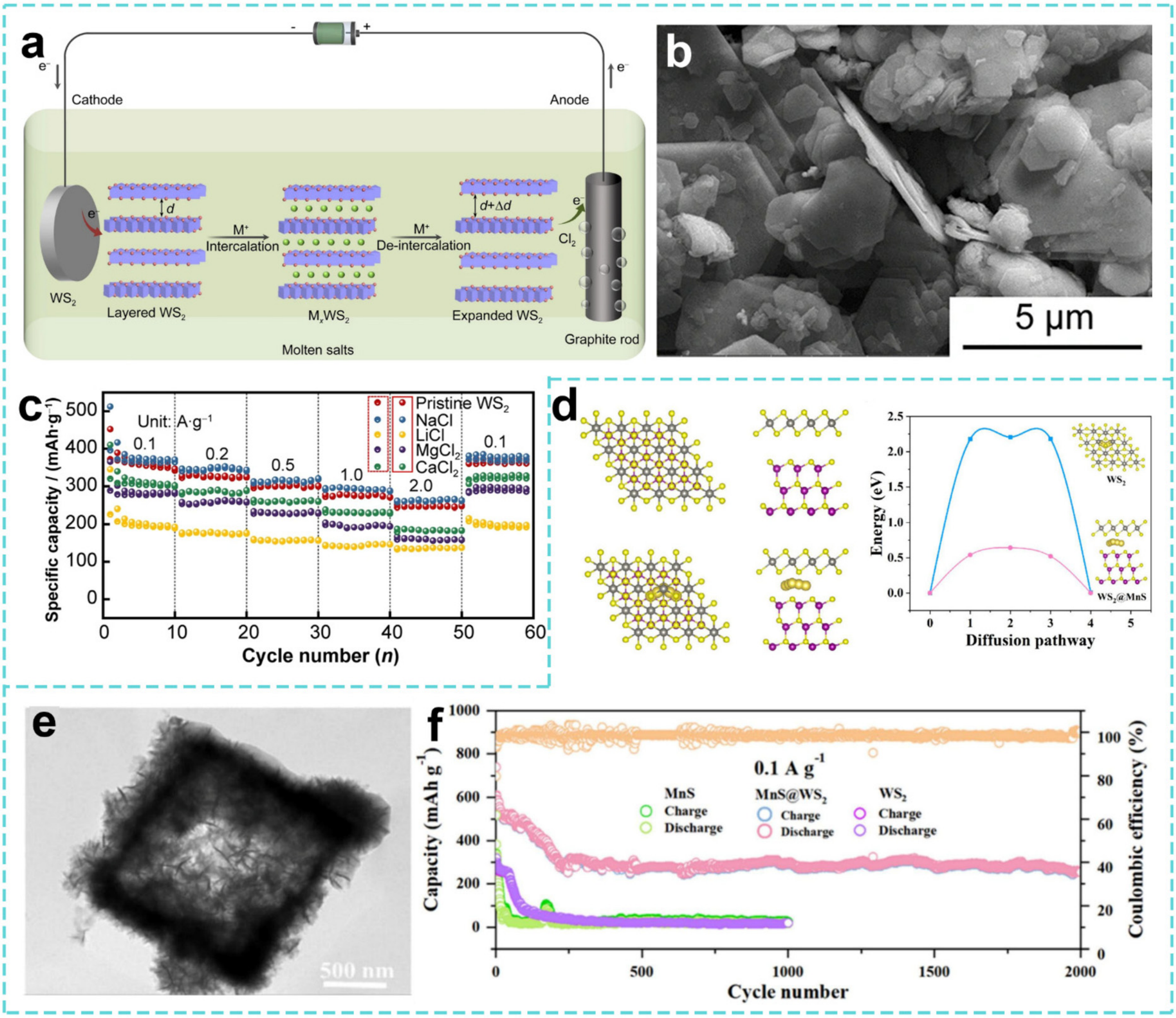

Fig. 14 (a) Illustration of the electrochemical exfoliation process for WS_2 in molten salt. (b) SEM image of WS_2–NaCl-25 mA. (c) Rate performance at various current densities of pristine WS_2 and WS_2 treated with different molten salts. Reproduced with permission from ref. 212. Copyright 2023, Springer Nature. (d) Optimized model of WS_2@MnS heterostructures before or after Na^+ insertion and energy barriers of the diffusion behavior of Na^+ in pure WS_2 and WS_2@MnS heterostructures. (e) TEM image of WS_2@MnS heterostructures. (f) Cycling performances of pure WS_2, pure MnS and WS_2@MnS electrodes. Reproduced with permission from ref. 213. Copyright 2024, Elsevier.

tronic conductivity, while the semiconducting 2H phase has a stable structure. By regulating the ratio of the two phases through phase engineering or constructing a heterostructure, the conductivity and structural stability of the material can be synergistically optimized.[216] In addition, the abundant active sites on its surface can promote the adsorption and storage of Na^+, and the lower electronegativity of selenium atoms makes the material more susceptible to redox reactions during the charging and discharging process, thereby improving the theoretical specific capacity.

In the study of anode materials for SIBs, different research teams have conducted multi-faceted explorations of the key bottlenecks of layered transition metal disulfides. In response to the problem of selenium dissolution and kinetic limitations on the surface of layered transition metal sulfides (TMDs), Kang *et al.* proposed a heterogeneous $MoSe_2$ nanoflower structure modified with surface amorphous MoO_3 ($MoSe_2/MoO_3$) (Fig. 15a). Through a solvothermal reaction combined with a controllable oxidation strategy, a uniform amorphous MoO_3 protective layer was constructed on the surface of the flower-like $MoSe_2$ to form a unique heterogeneous interface (Fig. 15b and c). As shown in Fig. 15d and e, the material has a first-cycle discharge capacity of 729 mAh g^{-1} at a current density of 50 mA g^{-1}, reaching 89% of the theoretical capacity, and has a good rate performance.[217] The breakthrough in interface engineering laid the foundation for subsequent structural design. Liu *et al.* proposed the concept of 2D nanosheets combined with 3D porous carbon for collaborative design, and developed a composite material of 3D ordered macroporous carbon loaded with ultra-thin 2D $MoSe_2$ nanosheets. This system shortens the Na^+ diffusion path through the 0.76 nm ultra-large interlayer spacing of 2D $MoSe_2$ and alleviates

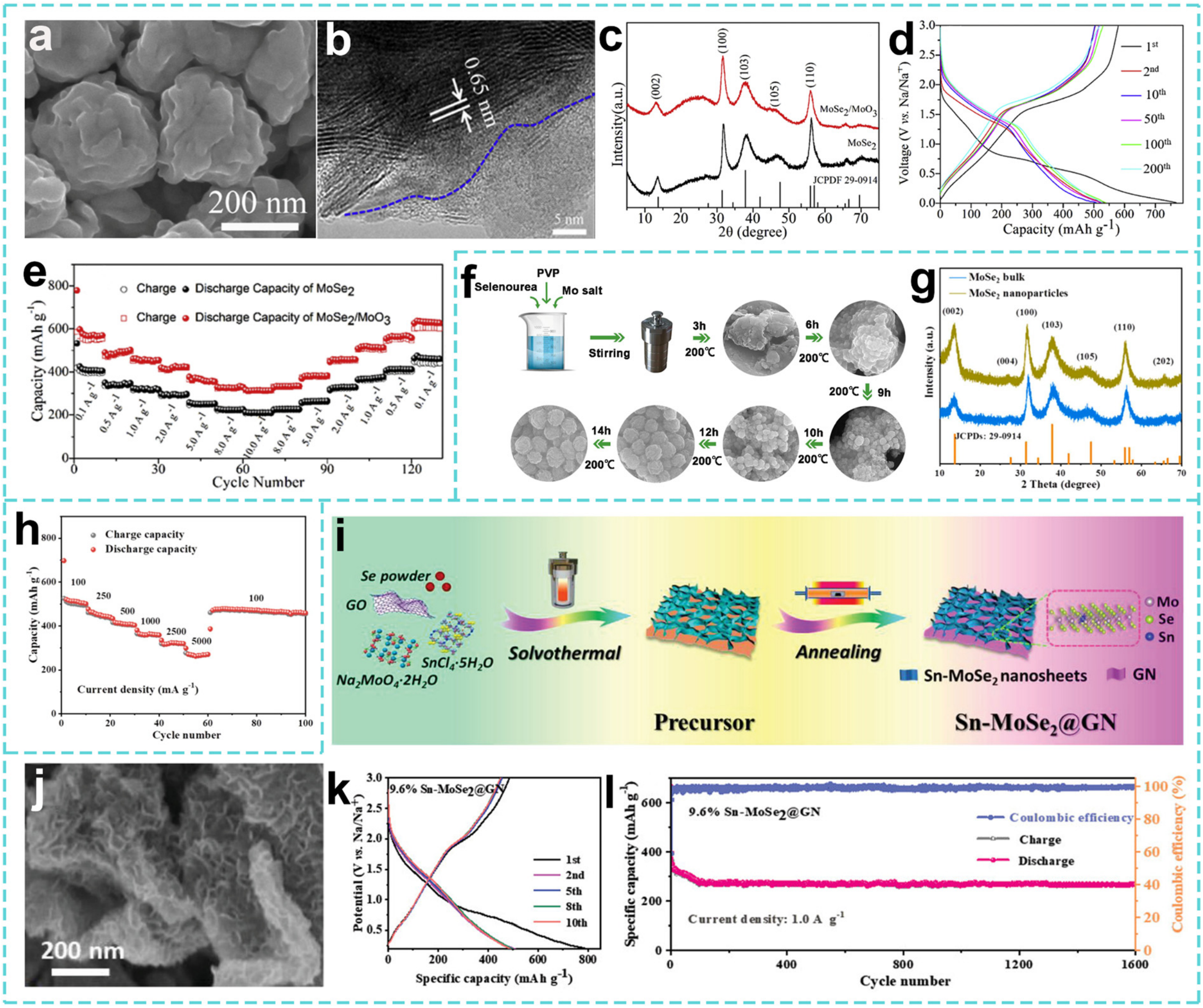

Fig. 15 (a) SEM image and (b) HRTEM image of $MoSe_2/MoO_3$ composite. (c) XRD patterns of $MoSe_2$ nanostructure and $MoSe_2/MoO_3$ composite. (d) Typical discharge/charge profiles of $MoSe_2/MoO_3$ composite anode. (e) Rate capability for $MoSe_2$ and $MoSe_2/MoO_3$ composite. Reproduced with permission from ref. 217. Copyright 2018, Elsevier. (f) The detailed formation mechanism of the $MoSe_2$ nanoparticles. (g) XRD patterns of $MoSe_2$ nanoparticles and $MoSe_2$ bulk. (h) Rate performance of the $MoSe_2$ nanoparticles electrode. Reproduced with permission from ref. 219. Copyright 2022, Elsevier. (i) Schematic and the synthesis process, (j) SEM image of Sn-$MoSe_2$@GN. (k) GCD profiles, (l) Long-term cycling performance of the Sn-$MoSe_2$@GN electrode. Reproduced with permission from ref. 220. Copyright 2022, Wiley.

volume expansion with the ordered cavities of 3D ordered macroporous (3DOM) carbon.[218] As the 3D structure design gradually matured, Li *et al.* shifted the focus of their research from macroscopic structure to microscopic synthesis mechanisms, exploring the regulatory effect of polymers on the growth of nanoparticles.

As shown in Fig. 15f and g, by introducing polyvinyl pyrrolidone into a hydrothermal method, the excessive aggregation of $MoSe_2$ nanosheets was suppressed by its steric hindrance effect, and the orderly assembly of $MoSe_2$ nanosheets was guided to form uniform nanoparticles. The hierarchical structure formed optimized the electron transmission path and exposed more active sites. The reversible capacity of the material reached 374.9 mAh g^{-1} after 100 cycles at 500 mA g^{-1}, and it also had a good rate performance. For the SIB application, the material loading of $MoSe_2$ nanoparticles was 2.0 mg cm^{-2}, and the standard electrolyte for SIBs was used (Fig. 15h).[219] While the structural design and synthesis process are being continuously optimized, Hu *et al.* shifted their focus to the regulation of the intrinsic properties of the material. By doping tin into $MoSe_2$ nanosheets grown *in situ* on a graphene (GN) substrate, they prepared an anode material (Sn-$MoSe_2$@GN) (Fig. 15i and j).[220] As shown in Fig. 15k, due to the formation of the SEI layer, the initial discharge/charge specific capacity of the material is 786.2/506.8 mAh g^{-1}, and the initial coulombic efficiency is 64.46%. In addition, the practical capacity remains at 268.5 mAh g^{-1} after 1600 cycles at 1 A g^{-1} (Fig. 15l), providing a new paradigm for the combined application of chemical doping and electrochemical regulation.

Based on the optimization of a single energy storage function, Cho *et al.* prepared a mesoporous WSe_2 reduced graphene oxide (WSe_2–rGO) composite material by spray pyrolysis (Fig. 16a). As seen from Fig. 16b and c, the WSe_2–rGO composite particles have both well-dispersed rGO nanosheets and many well-faceted WSe_2 nanocrystals with folded edges. The discharge capacities of the WSe_2–rGO composite particles and the bare WSe_2 particles in the 100th cycle under Na^+ storage at a current density of 0.5 A g^{-1} are 238 and 36 mAh g^{-1}, respectively (Fig. 16d). Due to the synergistic effect of rGO and WSe_2, the rGO network improves the electronic conductivity, the mesoporous structure shortens the ion diffusion path, and the wrinkled WSe_2 nanocrystals expose abundant active sites, thereby improving its electrochemical performance.[221] As the research deepened, Shinde *et al.* proposed an atomically thin (WO_3/WSe_2) heterostructure (Fig. 16e) to address the challenge of slow Na^+ diffusion kinetics in aqueous sodium storage. As shown in Fig. 16f, an atomically thin WO_3/WSe_3 heterostructure was constructed by a hydrothermal method combined with chemical vapor deposition (CVD) and anchored on a carbon fiber substrate. The WO_3/WSe_3 electrode has a specific capacitance of 378.1 F g^{-1} at 1 A g^{-1}, and its performance is stable over more than 10 000 cycles (Fig. 16g), providing theoretical and experimental dual verification for the interface electronic regulation of 2D heterojunctions (Fig. 16h).[222]

These studies revolve around the core bottleneck of layered TMDs in the anode application of SIBs, and innovations have been made at multiple levels, including surface engineering, 3D architecture, synthesis regulation, chemical bonding, doping optimization, and heterogeneous interfaces. They have constructed a theoretical system for the coordinated optimization of “structure–interface–function”, and formed a com-

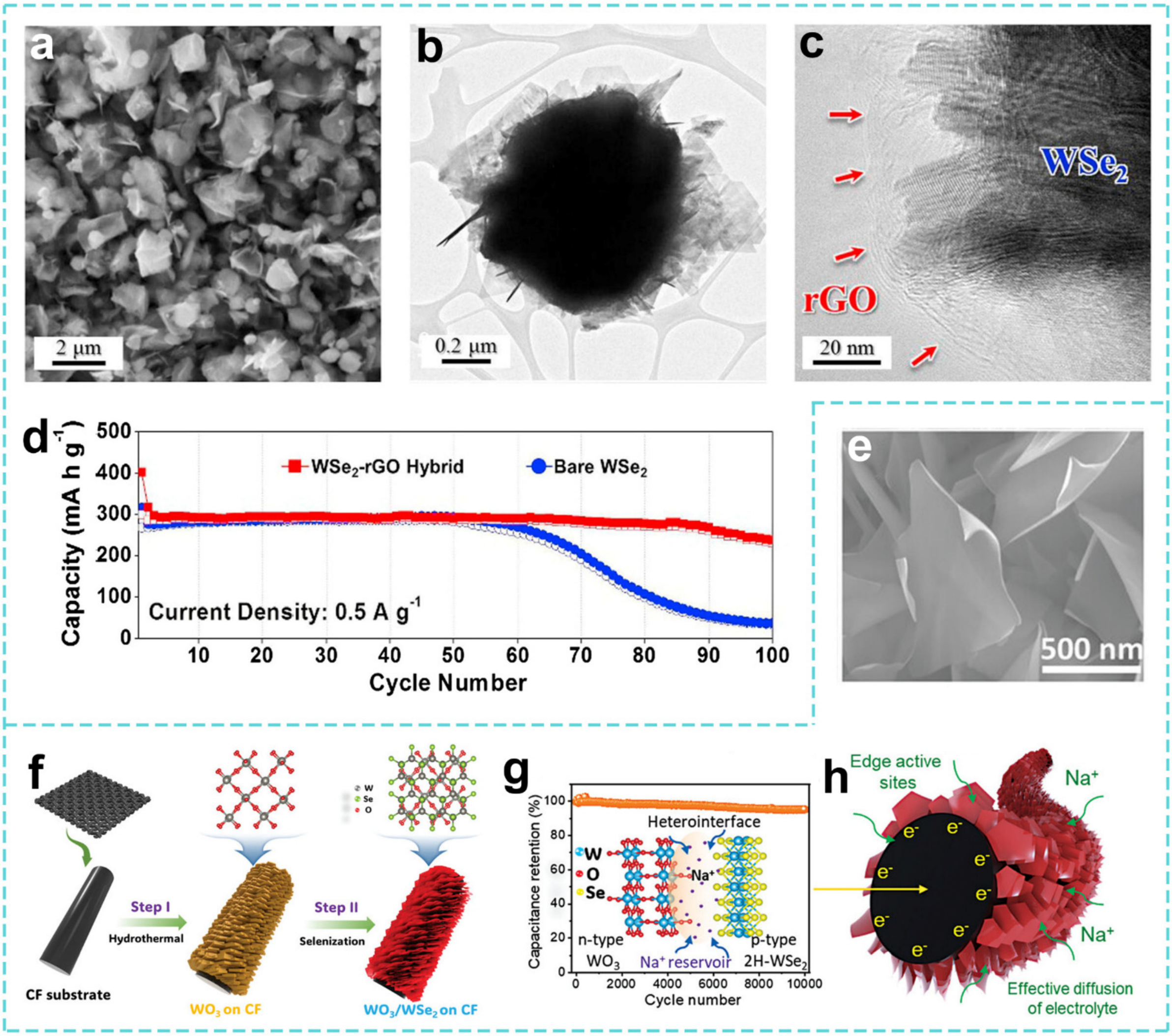

Fig. 16 (a) SEM image, (b) TEM image, and (c) HRTEM image of the WSe_2–rGO composite. (d) Cycling performances of the WSe_2–rGO electrode. Reproduced with permission from ref. 221. Copyright 2018, Elsevier. (e) SEM image of the WO_3/WSe_2 heterostructures. (f) Two-step synthesis protocol for the WO_3/WSe_2 heterostructures on CF. (g) Cycling stability measured for 10 000 cycles at 10 A g^{-1}. The inset displays the schematics for the improved electrochemical performance of WO_3/WSe_2. (h) Schematic illustration of Na^+ ion storage in the WO_3/WSe_2 heterostructure. Reproduced with permission from ref. 222. Copyright 2024, Wiley.

plete research chain from macroscopic design to microscopic mechanistic analysis. From the synergistic effect of flower-like nanostructures and surface amorphous layers to the spatial coupling of 3D porous carbon substrates and 2D nanosheets and the charge transfer optimization of heterogeneous interfaces, researchers have successfully achieved breakthroughs in the sodium storage dynamics of materials, structural stability, and versatility.

5.3 Mo- and W-based carbon composites

Mo- and W-based carbon composites combine the unique sodium storage mechanism of Mo- and W-based materials with the excellent conductivity and structural stability of carbon materials, showing great research value in the field of SIB anodes. In terms of sodium storage performance, Mo- and W-based materials combined with carbon materials provide adsorption sites and promote electron transfer to achieve a high specific capacity. In terms of cycling stability, carbon materials buffer the volume changes of Mo- and W-based materials, reduce structural damage, and improve cycling stability. In terms of conductivity, carbon materials construct electron transfer networks, make up for the conductivity defects of Mo- and W-based materials, and improve the rate performance.[223] In terms of electrode density and volumetric energy density, Mo- and W-based carbon composite materials generally exhibit a higher packing density than that of traditional hard carbon materials, which helps to improve the volumetric energy density of batteries. Typical MoS_2/WS_2–carbon composites have a higher packing density than traditional hard carbon. This higher packing density not only increases the amount of active material per unit volume but also reduces the loss in volumetric energy density, thereby improving the overall energy density of the battery. By optimizing the carbon content and material structure, Mo- and W-based carbon composites can significantly increase the electrode density while maintaining the specific capacity, reducing the volume loss caused by low-density materials.[224,225] In terms of electrolyte compatibility, carbon materials improve the interface compatibility, form a stable SEI membrane, and improve the coulombic efficiency and overall performance; this provides strong support for the development of SIBs.

In the study of Mo-based carbon composite material systems, researchers have continuously broken through the performance limits of traditional materials through multi-dimensional structural design strategies. Based on this problem of slow interlayer diffusion and insufficient cycling stability of 2D MoS_2-based SIB anode materials, Wang *et al.* constructed vertically oriented MoS_2/C nanosheet array (MoS_2/C NSA) materials on the surface of 3D carbon cloth through micro-area etching and functionalization strategies (Fig. 17a and b). The MoS_2 interlayer spacing was expanded to 0.99 nm through heterogeneous interface engineering, and the Na^+ diffusion coefficient was increased by 3 times by combining the surface contact advantages of the carbon cloth substrate, achieving a high sodium storage capacity and fast charge and discharge capabilities. The material maintained a practical capacity of 271 mAh g^{-1} after 10 000 cycles at 3 A g^{-1}. The material consists of MoS_2/C heterostructures on carbon cloth, with a mass loading of 1.1 mg cm^{-2}. The electrolyte used in this study was $NaClO_4$ in a typical PC solution, with the addition of 5 wt% FEC as an electrolyte additive (Fig. 17c and d). This 3D heterogeneous interface system solves the bottleneck of interlayer diffusion kinetics.[226]

With the in-depth development of the concept of interface engineering, researchers began to explore the synergistic optimization of multi-composite systems and reaction mechanisms. Luo *et al.* fabricated a new type of hierarchical ZnS/MoS_2 bimetallic sulfide through a sulfurization reaction, in which ZnS/MoS_2 nanoparticles were encapsulated in a nitrogen-doped carbon framework derived from a Zn/Mo bimetallic imidazole framework (Zn/Mo BIFs) and covered with reduced graphene oxide (ZnS@MoS_2/NC@rGO) (Fig. 17e and f). The nitrogen-doped carbon and rGO nanosheets obtained could improve the conductivity and accommodate the volume changes of ZnS and MoS_2. At the same time, the ZnS–MoS_2 heterostructure accelerates the diffusion kinetics in the interface and increases the charge transfer rate. The material consists of ZnS–MoS_2 nanocomposites, with a mass loading of approximately 1.0 mg cm^{-2}. The electrolyte used in this study is a mixture of $NaClO_4$ in a carbonate solution of PC and EC, with 5 wt% FEC added (Fig. 17g).[227]

Zhao *et al.* developed a different approach, using biomass-derived carbon fibers and MoO_2 composites, and designed a feasible core–shell structure C@MoO_2 sunflower seed shell cellulose carbon sphere (C@MoO_2 SSCCM) by coating MoO_2 nanoparticles on the surface of biomass carbon spheres (Fig. 17h–j). This structure effectively inhibits volume changes during Na^+ charging and discharging, making up for the low theoretical specific capacity of biomass carbon. Compared with pure MoO_2 materials, the composite material has a better rate performance, with a practical capacity of 345.6 mAh g^{-1} after 180 cycles at 0.2C (Fig. 17k and l).[228] To solve the common problem of high rate and long cycle life, Liu *et al.* prepared encapsulated $MoSe_2$@hollow carbon nanosphere ($MoSe_2$@HCNS) materials, that is, encapsulated multilayer $MoSe_2$ nanosheets with an interlayer spacing extended to 1.02 nm in hollow carbon spheres using a spatial confinement strategy to construct a core–shell confinement and interlayer expansion synergistic system.[229] The $MoSe_2$@HCNS material has a practical capacity of 382 mAh g^{-1} at 10 A g^{-1} ultrafast charge and discharge, and a coulombic efficiency of over 99.5%. Innovations in preparation processes are also driving breakthroughs in material systems. The $MoSe_2$ nanosheets used in this study had a loading of 1.1 mg cm^{-2}, which was below the typical range of 2–3 mg cm^{-2}. Zhang *et al.* synthesized self-supporting MoO_2 nanosheets embedded in carbon nanofibers through electrospinning and sintering. The high specific capacity and cycling stability of MoO_2 nanosheets are due to changes in the release volume of carbon nanofibers, which provide a 3D conductive diffusion network. The self-supporting structure can prevent particle shedding caused by polarization and improve the electrode stability. In this study,

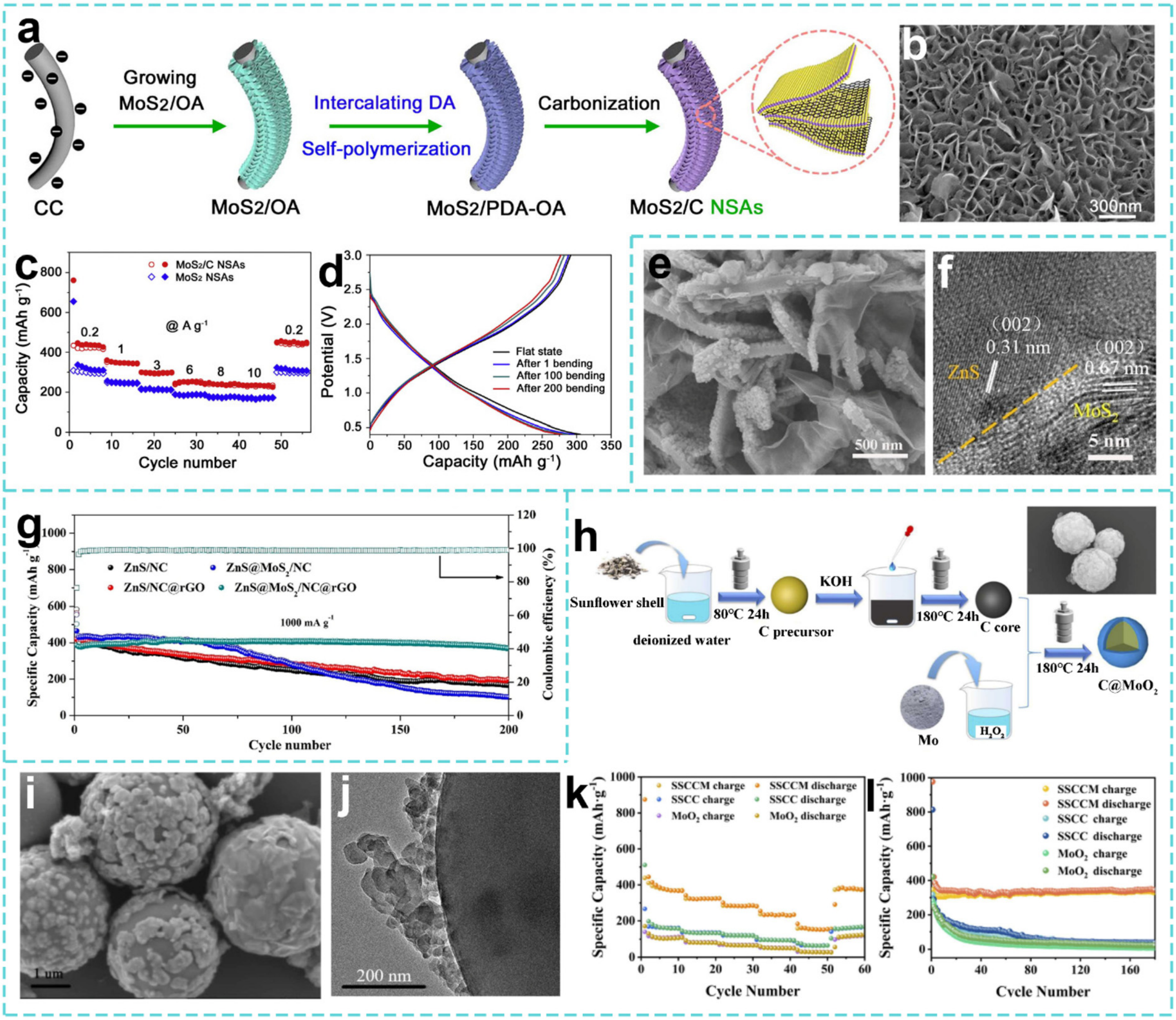

Fig. 17 (a) Schematic illustration of the fabrication process and (b) SEM image of MoS_2/C NSAs. (c) Rate performances of the MoS_2/C NSAs and MoS_2 NSAs electrodes. (d) The charge/discharge curves of the assembled MoS_2/C NSAs flexible battery. Reproduced with permission from ref. 226. Copyright 2017, Elsevier. (e) SEM image and (f) HRTEM image of ZnS@MoS_2/NC@rGO. (g) Cycling performance of different samples. Reproduced with permission from ref. 227. Copyright 2023, Elsevier. (h) Schematic description of the preparation of SSCCM. (i) SEM image and (j) HRTEM image of the SSCCM composite. (k) Rate behaviors and (l) cycling performances of SSCC, MoO_2 and the SSCCM composite at 0.2C. Reproduced with permission from ref. 228. Copyright 2022, Elsevier.

the MoO_2 and carbon fiber material had a loading of 1.5 mg cm^{-2}, which was below the 2–3 mg cm^{-2} range. The electrolyte used was a mixture of carbonates (PC and EC) with $NaClO_4$, and 5% FEC was added.[230]

In the study of composite systems of tungsten-based sulfide and carbon materials, researchers have continuously broken through the limits of material performance through multi-dimensional structural design and interface engineering strategies. Liu *et al.* prepared a double-layer WS_2/hollow carbon composite material by an *in situ* hydrothermal method, which involved growing WS_2 on the surface of nanoscale hollow carbon spheres. The high specific surface area, excellent conductivity and unique structure of hollow carbon spheres provide a growth substrate for WS_2, enhancing the conductivity and provide abundant active sites.[231] Based on this structural advantage, Li *et al.* further innovated the interface design strategy and constructed a flower-like WS_2/multi-walled carbon nanotube (WS_2/MWCNT) hybrid structure. Through an *in situ* growth process, the petal-shaped WS_2 nanosheets are tightly wrapped around the surface of 1D multi-walled carbon nanotubes to form a core–shell structure with strong interface bonding. This heterogeneous design makes the specific capacity of the composite material more than three times that of pure WS_2 due to the synergistic effect of the 3D electron high-speed channels constructed by MWCNTs and the fast ion diffusion path of WS_2 nanosheets. The material has a loading of 1.0 mg cm^{-2}, which is below the 2–3 mg cm^{-2} threshold. The electrolyte used is based on $NaClO_4$, with 5% FEC added.[232] In response to the interface optimization problem of multi-component composite materials, Wang *et al.* proposed a partial selenization strategy and designed a composite material with a core–shell structure ($MoWSe_2/WO_3/C$) by a solvent-assisted method (Fig. 18a–c). This material forms a WSe_2 heterojunction through controllable selenization of the WO_3 surface, expanding the interlayer spacing between $MoSe_2$ and WSe_2 to 0.677 nm, and the carbon coating layer effectively improves the overall conductivity. As shown in Fig. 18d, the material still maintains a practical capacity of 384.3 mAh g^{-1} after 950 cycles at an ultra-high rate of 10 A g^{-1}. Its performance advantage stems from the low diffusion barrier brought by the expanded layer structure and the fast charge transfer characteristics of the heterogeneous interface (Fig. 18e).[233] In the in-depth exploration of the energy storage mechanism of 2D materials, Wei *et al.* constructed a 3D multi-level porous foam WS_2/graphene (WS_2/RGO) composite material by *in situ* anchoring of WS_2 on the reduced graphene oxide skeleton (Fig. 18f and g).[234] Its unique 3D interpenetrating porous structure effectively inhibits the stacking of WS_2 layers and enhances the exposure of active sites. Combined with the high conductivity and flexible support of RGO, it exhibits a high reversible capacity of 419 mAh g^{-1} and excellent rate performance as an anode for SIBs at a current density of 100 mA g^{-1}. The mass loading of WS_2 in the composite material was less than 2–3 mg cm^{-2}. The electrolyte used was a 1.0 M $NaPF_6$ solution in EC/DMC, with the addition of 5% FEC (Fig. 18h). This material provides a reference for the multi-level pore and reversible transformation synergistic strategy for application in 2D metal sulfide-based energy storage materials and SIB anode designs.

Through multi-composite strategies and innovative preparation processes, Mo- and W-based carbon composites have made significant progress in the application of anodes in SIBs. Techniques such as the hydrothermal method and *in situ* growth method effectively utilize the excellent conductivity and buffering properties of carbon materials, and cooperate with the sodium storage advantages of Mo- and W-based materials, to achieve a comprehensive improvement in cycling stability and rate performance. From expanding the interlayer spacing to promote ion embedding, to constructing a 3D porous structure to optimize the transmission path and from

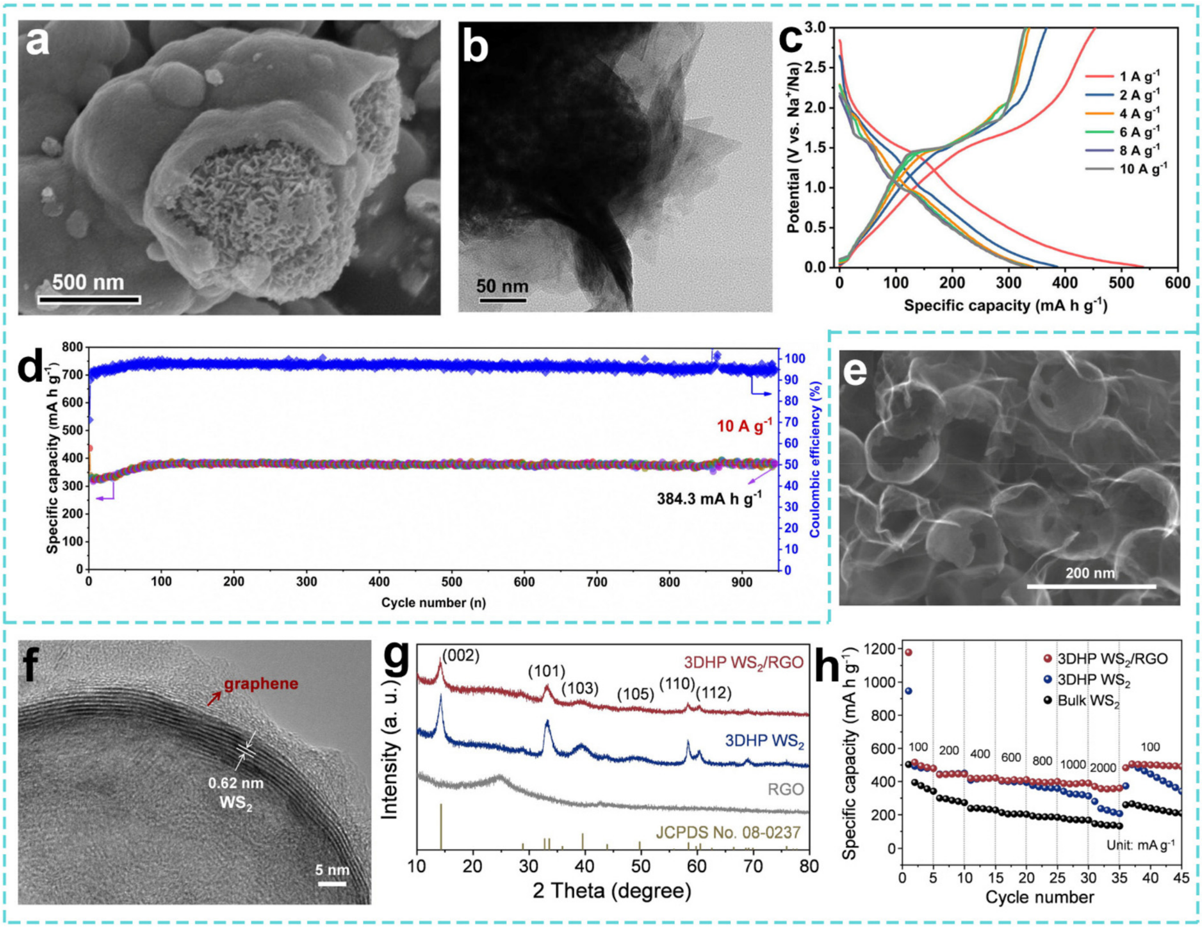

Fig. 18 (a) SEM image and (b) TEM image of $MoWSe_2/WO_3/C$. (c) Charge–discharge voltage profiles, (d) long cycling performance and coulombic efficiency of $MoWSe_2/WO_3/C$ at 10 A g^{-1}. Reproduced with permission from ref. 233. Copyright 2023, Elsevier. (e) SEM image and (f) HRTEM image of 3DHP WS_2/RGO. (g) XRD patterns of 3DHP WS_2/RGO, 3DHP WS_2 and RGO. (h) Rate capability of the 3DHP WS_2/RGO, 3DHP WS_2 and bulk WS_2 electrodes at various current densities. Reproduced with permission from ref. 234. Copyright 2024, Elsevier.

anchoring nanomaterials to enhance structural stability, to using heterogeneous interfaces to accelerate charge transfer, different studies explore the paths to improve the material performance from multiple dimensions.

5.4 Polymetallic molybdenum/tungstate

In the exploration of anode materials for SIBs, transition metal molybdates and tungstates stand out due to their unique structural advantages and electrochemical properties, while also facing some limitations. Polymetallic molybdate/tungstate exhibit significant advantages in Na^+ storage, particularly due to their inherent structural buffering characteristics. The strong covalent bond network of the metal–oxygen polyhedra (MoO_4^{2-}/WO_4^{2-}) provides a stable framework structure, which helps mitigate volume expansion during cycling, thereby improving cycling stability. Furthermore, the synergistic effect of multiple cations in these materials can improve the electrochemical kinetics and overall Na^+ storage performance. These materials typically possess layered or tunnel-like crystal structures, providing fast migration channels for Na^+, resulting in an excellent rate performance. Their multi-electron reaction characteristics allow for theoretical capacities of 300–600 mAh g^{-1}, significantly higher than those of traditional carbon-based anode materials. In addition, the strong covalent bond network of the metal–oxygen polyhedra (MoO_4^{2-}/WO_4^{2-}) effectively suppresses structural collapse during cycling, ensuring long-term stability.[235] However, the use of polymetallic molybdate/tungstate also presents some limitations. Synthesis complexity is a major challenge, as the multi-metallic nature of these compounds requires more complex synthesis routes, leading to increased production costs and greater synthesis difficulty. Furthermore, the mass fraction of inactive components in these materials may be relatively high, which can reduce the overall efficiency of sodium-ion storage. For example, some phases in the multi-metallic system may not directly participate in Na^+ storage, or their electrochemical activity may be lower than that of simpler MoO_2 or MoS_2 systems. Despite these challenges, the structural stability and multi-cation synergistic effects offered by polymetallic molybdate/tungstate make them promising candidates for future anode materials.[236]

To solve the problem of volume expansion of antimony-based anodes caused by alloying reactions, Lu *et al.* constructed hierarchical Sb_2MoO_6 microspheres by a surfactant-free microwave-assisted hydrothermal method. The material is self-assembled from 1D nanobelts to form a 3D porous structure (Fig. 19a and b). The material has a good cycling performance at different current densities (Fig. 19c). The mass loading of the Sb_2MoO_6 material in this study was 1.0 mg cm^{-2}, and the electrolyte used was a mixed solution of $NaClO_4$ in PC and EC, with the addition of 5% FEC. The unique sodium storage mechanism originates from the *in situ* generated Na–Mo–O conductive buffer matrix ($NaMo_3O_2$ constructs an electronic network and $Na_yMoVIOX$ inhibits volume expansion). This unique design offers a new direction for high-energy-density self-buffered anodes.[237] In the field of cathode material development, to solve the bottleneck of kinetic performance optimization, Huu *et al.* innovatively used a low-temperature steam-assisted solid-phase method to synthesize orthogonal $Fe_2(MoO_4)_3$ nanosheets. As a cathode material for SIBs, the $Fe_2(MoO_4)_3$ nanosheets were subjected to electrochemical testing under a mass loading of approximately 1.1 mg cm^{-2}, using a 1 M $NaClO_4$ solution in PC as the electrolyte, with the addition of 5 wt% FEC. Through the synergistic effect of the 3D stacking morphology and surface pseudocapacitance effect, the capacity decay rate of this material after 1000 cycles at 1C is only 0.012%/time, and the capacity retention rate at 5C at −20–60 °C is 78%. This combination of a low-temperature green synthesis strategy and amorphous/crystalline phase interface regulation provides a new paradigm for the design of sodium superionic conductor cathodes suitable for all climates.[238] In response to the structural stability challenge of molybdate anodes, Ali *et al.* developed a different approach and synthesized a nanocomposite material (Na_2MoO_4/C) by ball milling. This Na_2MoO_4/C nanocomposite was evaluated as an anode material for SIBs under a loading of approximately 3.5–3.8 mg cm^{-2}, using a 1 M $NaClO_4$ electrolyte dissolved in a mixed solvent of DEC, EC, and PC (volume ratio 1 : 1 : 1). This process nanoscales the micron-sized particles to 50 nm and uniformly composites them with the carbon matrix to form a "nano-confinement–carbon coating" synergistic system (Fig. 19d and e). As shown in Fig. 19f, the capacity retention rate of the material after 1000 cycles is as high as 96%, and the volume strain is only 0.68%. *In situ* synchrotron radiation characterization confirmed the reversible coordination change mechanism of the Mo–O tetrahedron and the role of the rigid crystal framework in suppressing lattice distortion.[239] To further improve the extreme performance of sodium superion conductor (NASICON) cathode materials, Sheng *et al.* developed a composite material of graphene-wrapped $Fe_2(MoO_4)_3$ nanoparticles (Fig. 19g). The 3D conductive network constructed by the microemulsion method combined with the annealing process greatly improved the electronic conductivity. In this work, the performance of the graphene-wrapped $Fe_2(MoO_4)_3$ nanoparticle composite material was evaluated with a cathode material mass loading of 1.5–3.0 mg cm^{-2} using 1 M $NaClO_4$ dissolved in a mixed solvent of ethylene carbonate and dimethyl carbonate as the electrolyte. The material maintained a practical capacity of 64.1 mAh g^{-1} at a high rate of 100C, and the capacity retention rate reached 76% after 100 cycles at 10C (Fig. 19h). This "conductive network wrapping–nanostructure regulation" synergistic strategy successfully overcomes the dual defects of NASICON materials: long ion diffusion paths and poor electronic conductivity.[240]

Turning to the multi-metal tungstate system in the field of layered oxide cathode interface engineering, Han *et al.* developed a one-step calcination grain boundary modification strategy to *in situ* construct a Na_2WO_4 network on nanomaterials (NM), and obtain micron-level spherical particles (NWO_5@NM) by adjusting the molar ratio of Na : Ni : Mn, which increased the volume density of the material by 18% (Fig. 20a). In this work, researchers evaluated a grain-bound-

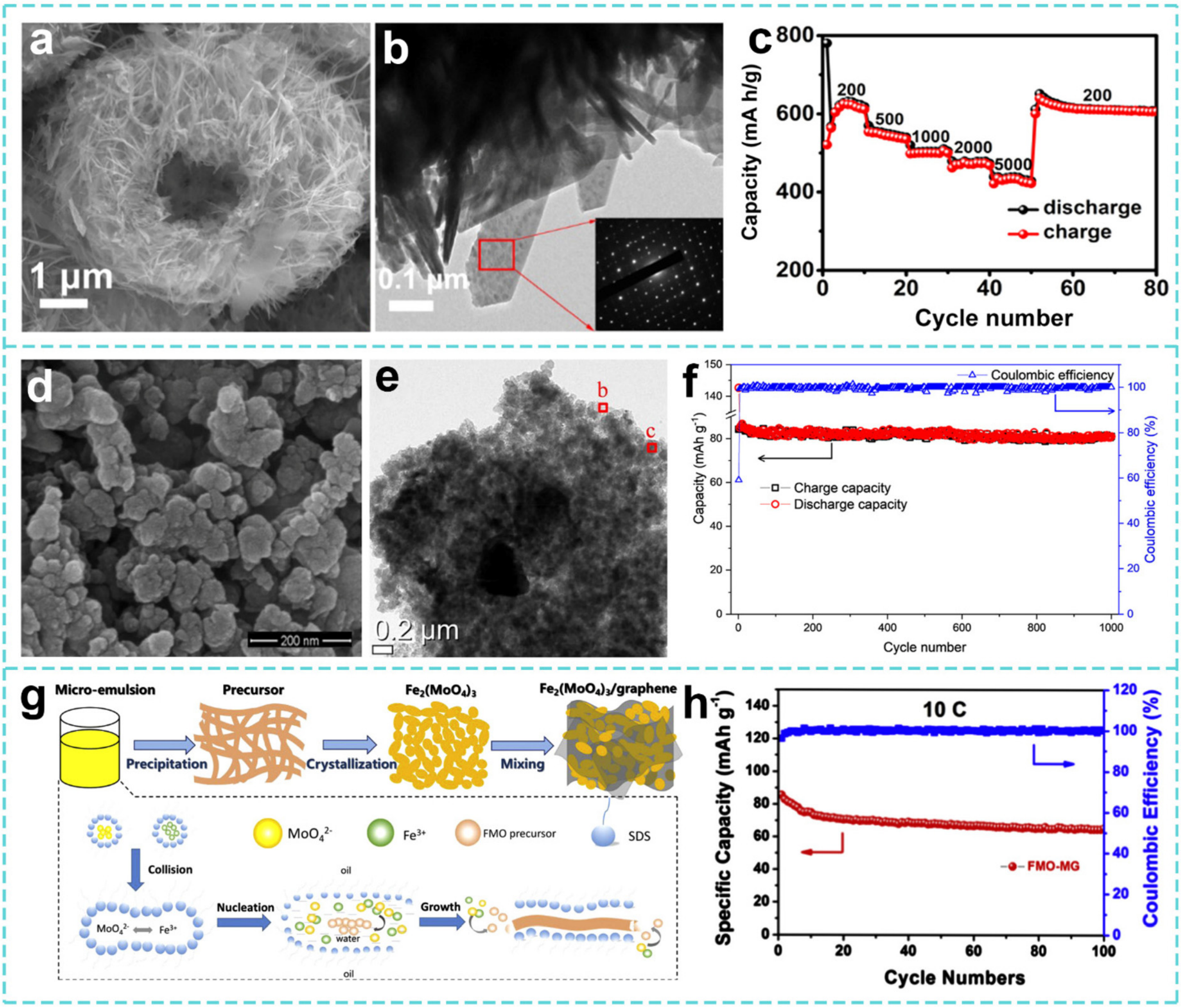

Fig. 19 (a) SEM image and (b) TEM image of Sb_2MoO_6 microspheres. (c) Rate performance of the Sb_2MoO_6 electrodes at 200 to 5000 mA g^{-1}. Reproduced with permission from ref. 237. Copyright 2019, Elsevier. (d) SEM image and (e) TEM image of carbon composite with Na_2MoO_4. (f) Cycling test of the composite electrode at 0.05C. Reproduced with permission from ref. 239. Copyright 2021, American Chemical Society. (g) Schematic illustration of the formation of the $Fe_2(MoO_4)_3$/graphene composite. (h) Cycling performance and coulombic efficiency of FMO-MG at a rate of 10C. Reproduced with permission from ref. 240. Copyright 2016, Elsevier.

ary-modified O3-type nickel-rich layered cathode material with added Na_2WO_4 under SIB conditions. The mass loading was approximately 2.8–3.2 mg cm^{-2}, and the electrolyte consisted of 1 M $NaClO_4$ dissolved in a mixed solvent of EC, PC, and DEC (volume ratio of 1 : 1 : 1), with the addition of 5 wt% FEC. The practical capacity of NWO_5@NM reached 126 mAh g^{-1} after 100 cycles at 1C (Fig. 20b). Mechanistic studies show that the Na_2WO_4 phase at the grain boundary has three functions: serving as a fast channel for Na^+, reducing the charge transfer barrier, and inhibiting electrolyte side reactions through physical barriers (Fig. 20c). This coating-free *in situ* grain boundary ion conductor implantation technology has achieved the leap from bulk doping to precise interface control of the layered cathode.[241] In response to the common problem of easy stacking of graphene composites, Wang *et al.* proposed an innovative solution: constructing a 3D $FeWO_4$/graphene mesoporous composite material through an *in situ* self-assembly hydrothermal method (Fig. 20d). As shown in Fig. 20e and f, the heterogeneous nucleation of $FeWO_4$ nanospheres and graphene forms an interpenetrating network structure, successfully expanding the interlayer spacing, and achieving a stable capacity of 377 mAh g^{-1} after 50 cycles at a current density of 20 mA g^{-1} for SIBs (Fig. 20g). This simple and scalable synthesis strategy provides a new idea for the development of universal energy storage materials compatible with multiple ions.[242]

These breakthroughs systematically solve the core problems of volume expansion, ion diffusion kinetics and interface stability of electrode materials through a precise synthesis methodology (microwave hydrothermal, low-temperature solid phase, ball milling composite, *etc.*) and multi-scale structural regulation (graded microspheres, core–shell nanosheets, grain boundary modification, *etc.*). The molybdate system has made significant progress in the design of self-buffered anodes and

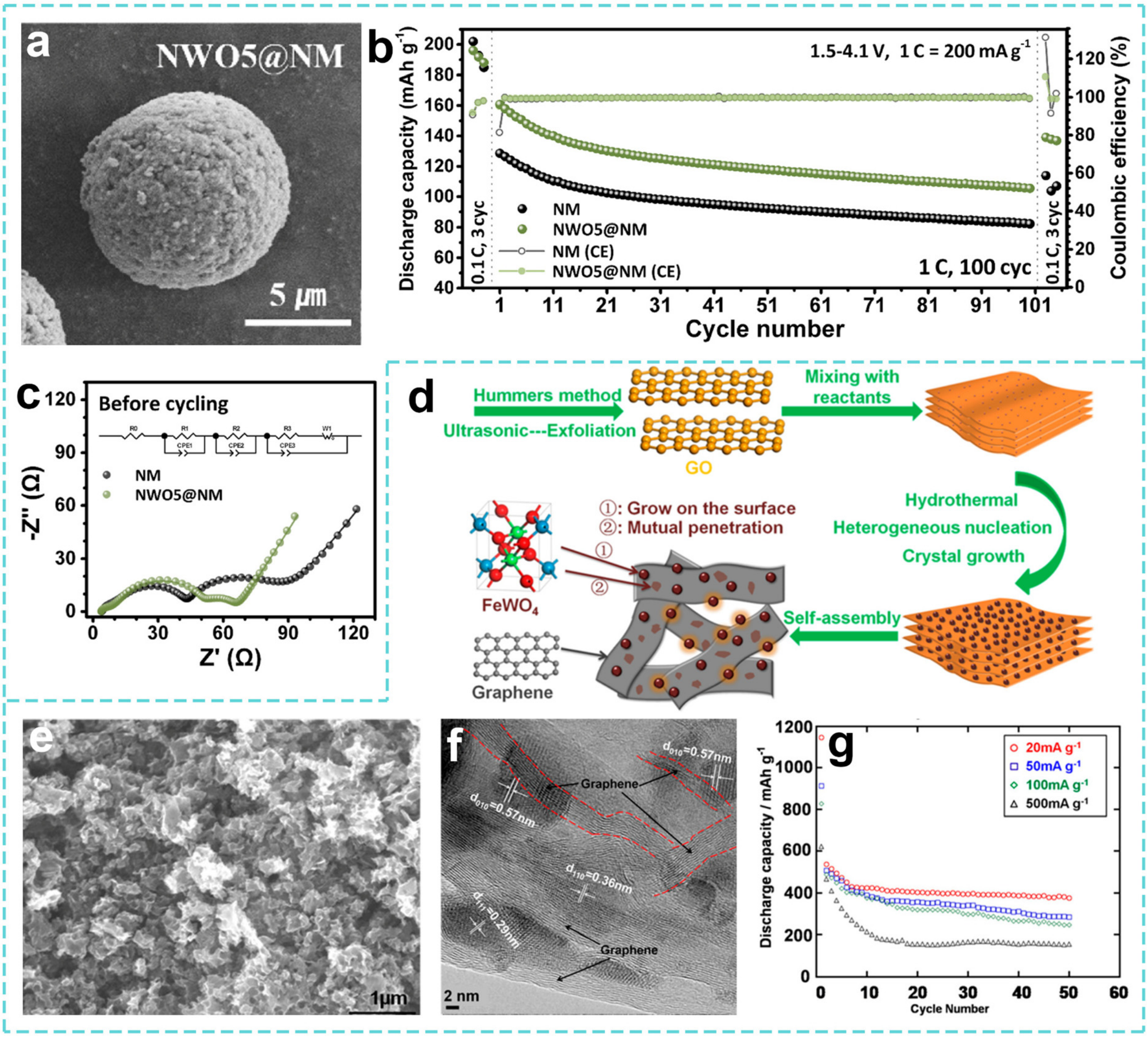

Fig. 20 (a) SEM image of $NaWO_5$@NM. (b) Capacity retention of NM and $NaWO_5$@NM. (c) EIS spectra of NM and $NaWO_5$@NM. Reproduced with permission from ref. 241. Copyright 2024, Elsevier. (d) Schematic illustration of the formation process of mesoporous $FeWO_4$/graphene composites. (e) SEM image and (f) TEM image of the $FeWO_4$/graphene nanosphere. (g) $FeWO_4$/graphene nanosphere for SIB under different current densities over 50 cycles. Reproduced with permission from ref. 242. Copyright 2014, American Chemical Society.

the development of high-rate positive electrodes, while the tungstate system has broadened the application boundaries through structural evolution analysis and interface engineering innovation, jointly promoting the movement of SIBs toward high energy density, long cycle life and all-climate adaptability.

Overall, significant progress has been made in research on Mo- and W-based materials as anodes for high-performance sodium-ion batteries. Mo-/W-based oxides (such as MoO_2, MoO_3, WO_3) typically provide a high theoretical capacity through conversion reactions, but their poor intrinsic conductivity and severe volume expansion lead to a poor rate performance and cycling stability. Mo-/W-based chalcogenides (such as MoS_2, WS_2, $MoSe_2$) possess open layered structures, which facilitate Na^+ intercalation and conversion reactions, exhibiting a high specific capacity and good rate potential; however, they are prone to interlayer stacking deactivation during cycling. To overcome these bottlenecks, Mo-/W-based carbon composites have become a research hotspot. Introducing a carbon matrix effectively improves the conductivity of the material and buffers volume changes, thereby significantly improving the cycle life and rate performance. In addition, multi-metallic molybdenum/tungsten compounds (such as molybdates) further optimize the sodium storage kinetics and structural stability through the synergistic effect between different metal components. Table 3 presents a comparison of the electrochemical properties of some Mo- and W-based materials that have been reported in recent years. In general, nanostructuring, composite materials, and structural design are key approaches for improving the electrochemical performance of such materials.

6. Summary and outlook

In recent years, Mo- and W-based materials have significantly improved the sodium storage performance in research on SIB anodes through structural optimization and multi-mechanism synergy. Single-atom catalysis and dynamic *in situ* characterization technology provide atomic-level theoretical support for performance breakthroughs, and green processes and resource recycling promote sustainable development. However, volume effects, insufficient conductivity, and interface stability are still key bottlenecks. In the future, we need to focus on multi-mechanism material design, sodium storage mechanism research, electrolyte matching and interface optimization, synthesis methods and process improvements, *etc*., to promote the development of high-energy, long-life, low-cost SIBs, and help large-scale energy storage and new energy applications.

With their multi-dimensional advantages, Mo- and W-based materials have shown broad and promising application prospects in the field of SIBs. Their high theoretical specific capacity characteristics provide core support for SIBs to achieve high energy density, and are expected to meet the needs of electric vehicles, energy storage power stations, *etc*. for large-capacity batteries. The unique sodium storage mechanism has opened a new path for performance improvement. With the in-depth study of the material structure and composition, its reversible specific capacity and cycling stability will be further optimized. In terms of structural design, nanosizing, porosity and composite strategies give the material flexible designability, which can not only improve the charging and discharging efficiency by increasing the specific surface area and optimizing the ion transmission path, but also effectively alleviate the volume changes, enhance the structural stability, and ensure the long-term stable operation of the battery. Good electrolyte compatibility enables Mo- and W-based materials to form a stable interface with ether-based electrolytes, reduces resistance, inhibits side reactions, and significantly improves the overall performance of the battery. In addition, thanks to abundant and cheap sodium resources and the relatively considerable reserves of Mo and W elements, this type of material has outstanding cost advantages in large-scale applications, which meet the urgent needs of large-scale energy storage, distributed energy and other fields for low-cost energy storage technology.

When comparing Mo- and W-based materials with more widely used anode materials such as hard carbon, alloy anodes (*e.g.*, Sn, Sb, P), and titanium (Ti)-based oxides, several factors should be considered, including cost, sustainability, safety, and scalability. Mo- and W-based materials generally have higher costs due to the need for specific processing methods and relatively expensive Mo and W resources. However, their potential for cost reduction through large-scale production and resource recycling, coupled with the abundance of sodium, make them competitive in the long term. In terms of sustainability, Mo- and W-based anodes are more environmentally friendly than lithium-based systems, benefiting from the availability of sodium and the ability to incorporate green synthesis methods. Safety is another strength, as Mo- and W-based materials offer strong structural stability, while alloy anodes face issues related to volume expansion and mechani-

Table 3 Comparison of the electrochemical performance of some Mo-/W-based materials in SIBs reported in recent years

Mo-/W-based materials	Cathode material	Half/full cells	Current density (A g^{-1})	Load mass (mg cm^{-2})	Capacity retention%/cycles	Ref.
VC-MoO_2	$Na_3V_2(PO_4)_3$	Full	0.3	1.02	96.5/1000	189
a/c-MoO_2	—	Half	1.0	—	86.0/3000	190
MoS_2/MoO_2	—	Half	5.0	—	100.0/400	191
DMcT-MoO_3	$Na_3V_2(PO_4)_2O_2F$	Full	0.2	—	99.2/100	196
MoO_3–MoS_2	$Na_3V_2(PO_4)_3$	Full	5.0	5.47	84.0/2300	198
HMF-MoS_2	—	Half	1.0	—	93.7/125	209
1T MoS_2	$Na_3V_2(PO_4)_3$	Full	1.0	—	94.0/200	210
$MoSe_2/MoO_3$	—	Half	10	—	55.4/200	217
$MoSe_2$	—	Half	0.5	2.00	86.7/100	219
Sn-$MoSe_2$	$Na_3V_2(PO_4)_2F_3$/C	Full	1.0	—	40.1/1600	220
ZnS@MoS_2/NCGO	$Na_3V_2(PO_4)_3$/C	Full	0.2	1.00	43.5/100	227
$MoSe_2$@HCNS	—	Half	10	1.10	99.5/1000	229
Sb_2MoO_6	$Na_3V_2(PO_4)_3$/C	Full	2.0	1.00	98.7/450	237
$Fe_2(MoO_4)_3$	MPC	Full	0.091	1.10	100.0/1000	238
Na_2MoO_4/C	—	Half	0.05	3.5–3.8	96.0/1000	239
$Fe_2(MoO_4)_3$	—	Half	9.1	1.5–3.0	76.0/100	240
WO_2/WS_2–rGO	PAC	Full	5.0	—	79.0/6000	192
WO_3	—	Half	0.25	—	100.0/300	199
WO_3	—	Half	0.5	—	74.0/100	200
WS_2–NaCl	$Na_3V_2(PO_4)_3$	Full	0.1	1.50	81.4/100	212
WS_2@MnS	$Na_3V_2(PO_4)_3$	Full	0.1	—	100.0/2000	213
WSe_2–rGO	—	Half	0.5	—	80.0/100	221
WO_2/WSe_2	MnSe/$MnSe_2$	Full	1.0	—	92.9/10 000	222
WS_2/hollow carbon	$Na_3V_2(PO_4)_3$/C	Full	0.1	—	57.5/200	231
$MoWSe_2/WO_2$/C	AC	Full	10.0	—	50.3/950	233
NWO_5@NM	$NaNi_{0.18}Mn_{0.12}O_2$	Full	0.2	2.8–3.2	65.6/100	241

cal stress during cycling. Although Ti-based oxides offer excellent stability, their lower theoretical capacity limits their energy density. While Mo- and W-based materials face challenges of synthesis complexity, they show great potential for scalability due to advancements in green manufacturing processes. In general, Mo- and W-based materials are a promising alternative for high-performance, long-life, and low-cost SIBs, especially as advancements in material design and manufacturing processes continue. In the future, the main research focuses of Mo- and W-based materials in SIB anodes are as follows:

(1) Material structure and performance optimization. Even though nanoparticles can shorten the diffusion process of Na^+, they still face the problem of agglomeration during the preparation process, and it is difficult to obtain an ideal structure. Therefore, researchers can try to prepare metal chalcogenide quantum dots to store sodium. The ultra-small size of quantum dots can significantly improve the utilization rate of electrode materials and increase active sites. Moreover, there are few studies in this area. Specifically, for Mo- and W-based anode materials, relevant research directions can be explored in the future. For example, quantum dots based on Mo/W compounds (*i.e.* MoS_2, WS_2) could be prepared through advanced synthesis techniques such as hydrothermal or solvothermal methods. The ultra-small size and high specific surface area of these quantum dots can enhance the sodium storage capacity and promote more efficient Na^+ intercalation and deintercalation. In addition, coupling Mo- and W-based materials with other materials (such as carbon or metal oxides) to construct heterostructures further improves the electronic conductivity and stabilizes the interface. These structures can alleviate aggregation problems and optimize charge transfer, which is crucial for high-performance SIBs. In the future, these advancements will not only improve the sodium storage performance but also address key challenges such as capacity decay and stability in Mo- and W-based anode materials.

(2) Electrolyte matching and interface optimization. For future research on electrolyte systems, specific focus should be placed on pairing Mo- and W-based anodes with low-viscosity ether/carbonate blends to enhance ion conductivity and reduce resistance. Another promising avenue is interface design for high-concentration electrolytes, which can significantly reduce side reactions and improve the overall stability of SIBs. Furthermore, there is a need for *operando* characterization techniques, such as XRD, X-ray absorption spectroscopy (XAS), and tomography, which are currently underutilized but essential for providing real-time insights into structural and electrochemical changes during cycling. These advancements could play a crucial role in addressing the challenges Mo- and W-based anodes face in SIBs. In addition, researchers can explore solid electrolytes, known for their excellent chemical stability, which could further enhance the interface effect in SIBs, reduce side reactions, and alleviate volume expansion. This may become a key breakthrough in the next generation of sodium storage technology.

(3) Improved synthesis methods and processes. Since the reaction conditions for traditional preparation methods are difficult to control, researchers could use spray pyrolysis in the future to synthesize nanoparticles with uniform size and good dispersion in one step, and regulate the components and construct porous-hollow structures, which could significantly shorten the Na^+ diffusion path and improve the specific capacity and rate performance of SIBs. Specifically, researchers can explore the optimization of precursor concentration and spray rate. By adjusting the precursor concentration and spray rate, the particle size distribution can be controlled, improving the uniformity of the nanoparticles. This will help improve dispersion and minimize aggregation, thus enhancing the electrochemical performance of Mo- and W-based materials. Furthermore, porous hollow structure design can be implemented. Spray pyrolysis can prepare porous and hollow nanostructures, which is beneficial for increasing the specific surface area and reducing the internal diffusion resistance of Na^+. These structures can also mitigate volume expansion during cycling, thereby improving the cycling stability of the material. At present, there are few studies using this method, the design of which is worth the attention of researchers.

Mo- and W-based materials show strong application potential in the field of SIBs. At present, researchers have been able to inject new impetus into the technological upgrading of SIBs through structural optimization and multi-mechanism synergistic innovations. However, the development of such materials is still in the exploratory stage, and there are many challenges to be explored and solved. With the in-depth application of cutting-edge technologies such as single-atom catalysis and *in situ* characterization, as well as the large-scale promotion of green manufacturing processes, Mo- and W-based materials are expected to make the leap from laboratory research to industrialized applications. This will not only promote the application of SIBs toward the goals of achieving high energy density, long cycle life and low cost, but also provide solid technical support for the global energy structure transition and sustainable development strategy.

Author contributions

All authors contributed to the discussion of contents and the editing of the manuscript prior to submission.

Conflicts of interest

There are no conflicts to declare.

Data availability

This study did not generate any new datasets. All data analyzed are from publicly available sources, as cited in the manuscript.

Acknowledgements

This work was financially supported by the National Natural Science Foundation of China (22269020 and 42167068) and the Key Project of the Natural Science Foundation of Gansu Province (25JRRA004).

References

1 S. Dutta and R. B. Choudhary, *Mater. Today Chem.*, 2025, **46**, 102711.
2 C. Hakim, N. Sabi and I. Saadoune, *J. Energy Chem.*, 2021, **61**, 47–60.
3 Z. Sun, H. Liu, W. Li, N. Zhang, S. Zhu, B. Chen, F. He, N. Zhao and C. He, *Prog. Mater. Sci.*, 2025, **149**, 101401.
4 S. Gandi, V. S. C. S. Vaddadi, S. S. S. Panda, N. K. Goona, S. R. Parne, M. Lakavat and A. Bhaumik, *J. Power Sources*, 2022, **521**, 230930.
5 Y. Zhang, G. Liu, Q. Sun, D. Qiao, J. Chen, L. Wen and M. Zhao, *J. Energy Storage*, 2024, **102**, 114279.
6 M. Li, Z. Du, M. A. Khaleel and I. Belharouak, *Energy Storage Mater.*, 2020, **25**, 520–536.
7 F. Wei, Q. Zhang, P. Zhang, W. Tian, K. Dai, L. Zhang, J. Mao and G. Shao, *J. Electrochem. Soc.*, 2021, **168**, 050524.
8 G. M. Tomboc, Y. Wang, H. Wang, J. Li and K. Lee, *Energy Storage Mater.*, 2021, **39**, 21–44.
9 Z. Zeng, Y. Mao, Z. Hu, K. Chen, Q. Huang, Y. Song, Z. Wu, P. Zhang, T. Chen and X. Guo, *Ind. Eng. Chem. Res.*, 2023, **62**, 15343–15359.
10 M. Chen, Z. Wang, Y. Wang, Y. Li and Q. Chen, *Appl. Mater. Today*, 2021, **23**, 100985.
11 L. Wang, H. Tian, X. Yao, Y. Cai, Z. Gao and Z. Su, *ChemElectroChem*, 2023, **11**, e202300414.
12 S. Dong, N. Lv, Y. Wu, Y. Zhang, G. Zhu and X. Dong, *Nano Today*, 2022, **42**, 101349.
13 B. Liu, Y. Cao, H. Zhang, S. Wang, Q. Geng, Y. Li and F. Dong, *Chem. Eng. J.*, 2022, **446**, 136918.
14 J. Liang, C. Wei, D. Huo and H. Li, *J. Energy Storage*, 2024, **85**, 111044.
15 M. Zhou, Y. Shen, J. Liu, L. Lv, X. Gao, Y. Zhang, X. Meng, X. Yang, Y. Zheng and Z. Zhou, *Vacuum*, 2022, **200**, 111054.
16 L. Wang, G. Yang, S. Peng, J. Wang, W. Yan and S. Ramakrishna, *Energy Storage Mater.*, 2020, **25**, 443–476.
17 M. He, S. Liu, J. Wu and J. Zhu, *Prog. Solid State Chem.*, 2024, **74**, 100452.
18 G. Sun, Z. Wei, N. Chen, G. Chen, C. Wang and F. Du, *Chem. Eng. J.*, 2020, **388**, 124305.
19 D. Choi, S. Lim and D. Han, *J. Energy Chem.*, 2021, **53**, 396–406.
20 S. Kumar, M. Singh, R. Mondal, M. Kumar, R. Prakash and P. Singh, *Energy Fuels*, 2022, **37**, 1288–1296.
21 Z. Qian, X. Wang, T. Liu, L. Zhang and J. Yu, *J. Energy Storage*, 2022, **51**, 104522.
22 C. Li, Q. Fu, K. Zhao, Y. Wang, H. Tang, H. Li, H. Jiang and L. Chen, *Carbon*, 2018, **139**, 1117–1125.
23 M. I. Jamesh and A. S. Prakash, *J. Power Sources*, 2018, **378**, 268–300.
24 C. Wang, S. Xue, X. Lei, J. Wen, X. Pan, F. Zhang, C. Zou and Y. Tang, *Chem. Eng. J.*, 2023, **470**, 144043.
25 X. He, X. Liu, Z. Yang, H. Zhang, L. Li, G. Xu, Y. Qiao, S. Chou and M. Wu, *Electrochem. Commun.*, 2021, **128**, 107067.
26 Q. Ruan, Y. Qian, M. Xue, L. Chen and Q. Zhang, *J. Energy Chem.*, 2024, **89**, 487–518.
27 J. Zhou, J. Chen, Y. Peng, Y. Zheng, A. Ze and X. Lin, *Coord. Chem. Rev.*, 2022, **472**, 214781.
28 Y. Jiang, J. Dong, S. Tan, Q. Wei, F. Xiong, W. Yang, Y. Shen, Q. Zhang, Z. Liu, Q. An and L. Mai, *J. Energy Chem.*, 2021, **55**, 295–303.
29 X. Yang, L. Gong, Y. Jin, T. Zheng, X. Wang, Q. Zhi, B. Yu, K. Wang and J. Jiang, *CCS Chem.*, 2025, **7**, 3063–3075.
30 Z. Liu, S. Tao, J. Han, Z. Gao, W. Xu, H. Min, X. Shen, H. Yang and J. Wang, *Mater. Today Energy*, 2023, **33**, 101256.
31 M. R. Panda, A. Raj K, A. Ghosh, A. Kumar, D. Muthuraj, S. Sau, W. Yu, Y. Zhang, A. K. Sinha, M. Weyland, Q. Bao and S. Mitra, *Nano Energy*, 2019, **64**, 103951.
32 Y. Wang, D. Wang, C. Bai, Y. Zhu, L. Xu, H. Xiao, Q. Shi, X. Li, X. Chen, H. Shao and G. Fang, *Inorg. Chem. Front.*, 2024, **63**, 15224–15235.
33 T. Song, N. Wu, X. Zheng, X. Zhang, S. Guo, Q. Yan, W. Yao and Y. Tang, *CCS Chem.*, 2025, **7**, 554–563.
34 J. Guo, J. Yang, J. Guan, X. Chen, Y. Zhu, H. Fu, Q. Liu, B. Wei and H. Geng, *Chem. Eng. J.*, 2022, **450**, 138007.
35 H. He, D. Sun, Y. Tang, H. Wang and M. Shao, *Energy Storage Mater.*, 2019, **23**, 233–251.
36 S. McArdle, F. Bauer, S. F. Granieri, M. Ast, F. Di Fonzo, A. T. Marshall and H. Radinger, *ChemElectroChem*, 2023, **11**, e202300512.
37 H. Zheng, W. Yan and J. Zhang, *Electrochem. Energy Rev.*, 2025, **8**, 2401457.
38 X. Man, X. Min, Y. Yan, H. Gong, Y. Dai, T. Li, P. Xiao, Y. Sun, L. Yin and R. Wang, *Energy Storage Mater.*, 2025, **75**, 104076.
39 S. Lin, H. Zhang, C. Shu, W. Hua, X. Wang, Y. Zhao, J. Luo, Z. Tang, Y. Wu and W. Tang, *Adv. Funct. Mater.*, 2024, **34**, 2409628.
40 Y. Li, X. Lu, X. Zhao, H. Wang and X. Hu, *Prog. Nat. Sci.: Mater. Int.*, 2023, **33**, 767–779.
41 L. Liu, Y. Gong, Y. Tong, H. Tian, X. Wang, Y. Hu, S. Huang, W. Huang, S. Sharma, J. Cui, Y. Jin, W. Gong and W. Zhang, *CCS Chem.*, 2024, **6**, 1255–1263.
42 X. Liu, Z. Pan, Y. Xu, H. Lu, B. Li, K. Yan, F. Tang, Q. Zhou and L. Kong, *J. Energy Storage*, 2025, **120**, 116429.
43 S. Khammuang, T. Kaewmaraya, T. Hussain and K. Kotmool, *J. Power Sources*, 2026, **661**, 238592.
44 Y. Jayamkondan, T. R. Penki and P. K. Nayak, *Mater. Today Energy*, 2023, **36**, 101360.
45 C. I. Azambou, O. O. Obiukwu, P. K. Tsobnang, I. T. Kenfack, E. E. Kalu and E. E. Oguzie, *J. Energy Storage*, 2024, **94**, 112506.

46 I. Ullah, T. R. Aldhafeeri, A. Haider, X. Wu, Z. Ullah, S. Chang, A. Innayat, N. Begum, M. A. Pope, F. Sher, H. U. Rehman and I. Hussain, *ACS Appl. Energy Mater.*, 2025, **8**, 1743–1751.

47 M. Ma, Y. Yao, Y. Wu and Y. Yu, *Adv. Fiber Mater.*, 2020, **2**, 314–337.

48 K. Xiong, T. Qi and X. Zhang, *Electroanalysis*, 2024, **37**, e202400318.

49 J. Wang, J. Cui, Z. Li, D. Zhang, H. Sun, H. Wang, Q. Wang, H. J. Woo, S. Ramesh and B. Wang, *Chem. Eng. J.*, 2023, **464**, 142764.

50 H. Alptekin, H. Au, A. C. S. Jensen, E. Olsson, M. Goktas, T. F. Headen, P. Adelhelm, Q. Cai, A. J. Drew and M. M. Titirici, *ACS Appl. Energy Mater.*, 2020, **3**, 9918–9927.

51 M. Kaur, P. Sharma, R. Mir, K. Kaur, R. K. Sharma and A. Kumar, *FlatChem*, 2025, **51**, 100866.

52 K. Wang, H. Zhuo, J. Wang, F. Poon, X. Sun and B. Xiao, *Adv. Funct. Mater.*, 2023, **33**, 2212607.

53 Q. Ni, Y. Bai, F. Wu and C. Wu, *Adv. Sci.*, 2017, **4**, 1600275.

54 J. Cai, C. Liu, S. Tao, Z. Cao, Z. Song, X. Xiao, W. Deng, H. Hou and X. Ji, *Coord. Chem. Rev.*, 2023, **479**, 214985.

55 Y. Chen, J. You, X. Zhao, M. Li, X. Han, H. Liu, H. Sun, X. Wang, H. Li, P. Wang and Z. Liu, *Sci. China Mater.*, 2024, **67**, 3637–3647.

56 F. Gao, D. Zhang, H. Zhang, C. Gao, G. Huang, Z. Zhang, Y. Liu, Y. Wang, M. Terrones and Y. Wang, *Carbon*, 2024, **229**, 119481.

57 Y. Lin, S. Luo, W. Zhao, Q. Sun, J. Cong, P. Li, P. Li and S. Yan, *J. Energy Chem.*, 2024, **98**, 441–471.

58 X. Tang, C. Liu, H. Wang, L.-P. Lv, W. Sun and Y. Wang, *Coord. Chem. Rev.*, 2023, **494**, 215361.

59 T. Or, S. W. D. Gourley, K. Kaliyappan, Y. Zheng, M. Li and Z. Chen, *Electrochem. Energy Rev.*, 2022, **5**, 1600943.

60 J. Shi, L. Ding, Y. Wan, L. Mi, L. Chen, D. Yang, Y. Hu and W. Chen, *J. Energy Chem.*, 2021, **57**, 650–655.

61 A. Raj K, M. R. Panda, D. P. Dutta and S. Mitra, *Carbon*, 2019, **143**, 402–412.

62 D. Alvira, D. Antorán and J. J. Manyà, *Chem. Eng. J.*, 2022, **447**, 137468.

63 J. Wu, X. Li, H. Chen, Z. Yuan, J. Huang, L. Tong, J. Long, M. Li, X. Chen and Y. Chen, *CCS Chem.*, 2025, **7**, 2742–2753.

64 J. H. Kim, M. J. Jung, M. J. Kim and Y. S. Lee, *J. Ind. Eng. Chem.*, 2018, **61**, 368–380.

65 K. Mathiyalagan, D. Shin and Y.-C. Lee, *J. Energy Chem.*, 2024, **90**, 40–57.

66 Y. Zhao, Q. Liu, X. Zhao, D. Mu, G. Tan, L. Li, R. Chen and F. Wu, *Mater. Today*, 2023, **62**, 271–295.

67 P. Ma, D. Fang, Y. Liu, Y. Shang, Y. Shi and H. Yang, *Adv. Sci.*, 2021, **8**, e2003185.

68 T. Huang, B. Tian, J. Guo, H. Shu, Y. Wang and J. Dai, *Mater. Sci. Semicond. Process.*, 2019, **89**, 250–255.

69 M. Liu, W. Li, F. Liu and W. Zhang, *Nano Lett.*, 2024, **24**, 7180–7187.

70 H. Liu and B. Dong, *Mater. Today Phys.*, 2021, **20**, 100469.

71 Y. Liu, C. Sun, Y. Li, H. Jin and Y. Zhao, *Energy Storage Mater.*, 2023, **57**, 69–80.

72 C. G. Real, E. H. N. S. Thaines, L. A. Pocrifka, R. G. Freitas, G. Singh and H. Zanin, *J. Energy Storage*, 2022, **52**, 104793.

73 Y. Lei, Z. Yan, W. Lai, S. Chou, Y. Wang, H. Liu and S. Dou, *Electrochem. Energy Rev.*, 2020, **3**, 766–792.

74 H. Yin, D. Han, X. Yu, M. Cao, Z. Hou, C. Li and M. Zhu, *ACS Appl. Energy Mater.*, 2023, **6**, 1155–1175.

75 M. Xiao, X. Dai and Y. Jiang, *J. Energy Storage*, 2025, **111**, 115411.

76 L. Rakhymbay, N. Bazybek, K. Kudaibergenov, S. T. Myung, Z. Bakenov and A. Konarov, *J. Power Sources*, 2024, **602**, 234347.

77 S. Nie, L. Liu, J. Liu, J. Xia, Y. Zhang, J. Xie, M. Li and X. Wang, *J. Alloys Compd.*, 2019, **772**, 314–323.

78 D. Zeng, J. Xie, K. Qi, F. Yang, S. Peng, L. Liu, L. Wu, Y. Chen, X. Xiong and Y. Qiu, *J. Energy Storage*, 2024, **80**, 110339.

79 X. Lu, S. Li, Y. Li, F. Wu, C. Wu and Y. Bai, *Adv. Mater.*, 2024, **36**, e2407359.

80 V. Palomares, N. Nieto and T. Rojo, *Curr. Opin. Electrochem.*, 2022, **31**, 100840.

81 Q. Cheng, X. Zhao, G. Yang, L. Mao, F. Liao, L. Chen, P. He, D. Pan and S. Chen, *Energy Storage Mater.*, 2021, **41**, 842–882.

82 J. Do, I. Kim, H. Kim and Y. Jung, *Energy Storage Mater.*, 2020, **25**, 62–69.

83 B. Ma, Y. Liang, X. Ma, W. Wang, C. Miao, G. Yu, Q. Wang, C. Xu and X. Cui, *J. Colloid Interface Sci.*, 2025, **696**, 137824.

84 X. Chen and Y. Zhang, *Int. J. Energy Res.*, 2021, **45**, 9753–9779.

85 J. Liang, L. Zhang, D. XiLi and J. Kang, *Rare Met.*, 2020, **39**, 1005–1018.

86 T. Qi, K. Xiong and X. Zhang, *J. Power Sources*, 2025, **626**, 235721.

87 V. S. More and M. D. Yadav, *Energy Fuels*, 2024, **38**, 20285–20313.

88 K. Mathiyalagan, R. Raja, D. Shin and Y. C. Lee, *Prog. Mater. Sci.*, 2025, **151**, 101425.

89 P. Zhang, Z. Wang, Z. He, D. Zhang, J. Wang and Y. Zhao, *Composites, Part B*, 2025, **303**, 112564.

90 A. Song, Y. Li, D. Yuan, J. Wu, H. Gu, G. Zhang, A. Wu and J. Xu, *Green Energy Environ.*, 2024, **38**, 17146–17160.

91 M. S. Balogun, Y. Luo, W. Qiu, P. Liu and Y. Tong, *Carbon*, 2016, **98**, 162–178.

92 Y. Tian, Y. Chen, Y. Liu, H. Li and Z. Dai, *Chem. Rec.*, 2022, **22**, e202200123.

93 G. Zhang, T. Xiong, L. He, M. Yan, K. Zhao, X. Xu and L. Mai, *J. Mater. Sci.*, 2017, **52**, 3697–3718.

94 Z. Zhang, Y. Chen, S. Sun, K. Sun, H. Sun, H. Li, Y. Yang, M. Zhang, W. Li, S. Chou, H. Liu and Y. Jiang, *J. Mater. Sci. Technol.*, 2022, **119**, 167–181.

95 H. Liao, H. Liu, Q. Gou, R. Zeng, D. Zhao, X. Yuan, F. Chen, G. Xie and Y. Hou, *J. Power Sources*, 2025, **625**, 235739.

96 X. Yang, D. Zhang, L. Zhao, C. Peng, K. Ren, C. Xu, P. Liu, Y. Zhou, Y. Lei, B. Yang, D. Xue and F. Liang, *Adv. Energy Mater.*, 2024, **14**, 2304365.

97 X. Lv, J. Song, Y. Lai, J. Fang, J. Li and Z. Zhang, *J. Energy Storage*, 2016, **8**, 205–211.

98 D. Zhou, C. Zeng, J. Xiang, T. Wang, Z. Gao, C. An and W. Huang, *Ionics*, 2022, **28**, 2029–2040.

99 T. Sharmin, N. Hossain, F. T. Mohsin, M. A. Haque, M. M. Mashfy, T. A. Alvy and M. Nasim, *Mater. Today Chem.*, 2024, **42**, 102407.

100 S. Qi, B. Xu, V. T. Tiong, J. Hu and J. Ma, *Chem. Eng. J.*, 2020, **379**, 122261.

101 S. Zheng, Y. Tian, Y. Liu, S. Wang, C. Hu, B. Wang and K. Wang, *Rare Met.*, 2020, **40**, 272–289.

102 W. Zhao, M. Wang, H. Lin, K. Kim, R. He, S. Feng and H. Liu, *Prog. Nat. Sci.: Mater. Int.*, 2024, **34**, 263–273.

103 M. A. U. Din, C. Li, L. Zhang, C. Han and B. Li, *Mater. Today Phys.*, 2021, **21**, 100486.

104 Y. Gong, Y. Li, Y. Li, M. Liu, Y. Bai and C. Wu, *Small*, 2023, **19**, e2206194.

105 Y. Jiang, Z. Zhang, H. Liao, Y. Zheng, X. Fu, J. Lu, S. Cheng and Y. Gao, *ACS Nano*, 2024, **18**, 7796–7824.

106 M. Lee, J. M. Kim, N. Lee, J. K. Park and S.-M. Paek, *Chem. Eng. J.*, 2025, **519**, 164931.

107 T. S. Tedla, N. W. Hlongwa, T. T. I. Nkambule and M. A. Kebede, *Energy Rep.*, 2025, **14**, 3175–3203.

108 M. Xiao, *J. Power Sources*, 2026, **661**, 238634.

109 L. Xu, Y. Li, Y. Xiang, C. Li, H. Zhu, C. Li, G. Zou, H. Hou and X. Ji, *ACS Nano*, 2025, **19**, 14627–14651.

110 Y. Zhou, L. Zhou, Z. You, C. Zhao, J. Yang, S. Huang, M. Wang, Q. Zhong and J. Xiao, *J. Energy Storage*, 2025, **138**, 118768.

111 J. Bai, L. Zhang, S. Li, H. Ren, Y. Liu and S. Guo, *Chem. Eng. J.*, 2023, **452**, 139111.

112 A. Cheng, H. Zhang, W. Zhong, Z. Li, Y. Tang and Z. Li, *J. Electroanal. Chem.*, 2019, **843**, 31–36.

113 J. Jiang, W. Yang, H. Wang, Y. Zhao, J. Guo, J. Zhao, M. Beidaghi and L. Gao, *Electrochim. Acta*, 2017, **240**, 379–387.

114 H. Wu, N. Xu, Z. Jiang, A. Zheng, Q. Shi, R. Lv, L. Ni, G. Diao and M. Chen, *Chem. Eng. J.*, 2022, **427**, 131002.

115 B. Ye, L. Xu, W. Wu, Y. Ye, Z. Yang, Y. Qiu, Z. Gong, Y. Zhou, Q. Huang, Z. Shen, Z. Hong, Z. Meng, Z. Zeng, Z. Cheng, S. Ye, H. Hong, Q. Lan, F. Li, T. Guo and S. Xu, *ACS Sustainable Chem. Eng.*, 2022, **10**, 3166–3179.

116 G. Tian, Y. Song, X. Luo, Z. Zhao, F. Han, J. Chen, H. Huang, N. Tang and S. Dsoke, *J. Alloys Compd.*, 2021, **877**, 160299.

117 Q. Li, W. Zhang, J. Peng, W. Zhang, Z. Liang, J. Wu, J. Feng, H. Li and S. Huang, *ACS Nano*, 2021, **15**, 15104–15113.

118 R. Wang, S. Wang, X. Peng, Y. Zhang, D. Jin, P. K. Chu and L. Zhang, *ACS Appl. Mater. Interfaces*, 2017, **9**, 32745–32755.

119 Z.-Y. Song, Y.-D. Cao, L.-L. Fan, J. Song, Y. Feng, H. Liu, C.-L. Lv and G.-G. Gao, *Rare Met.*, 2024, **44**, 195–208.

120 X. Xu, Y. Qiu, Z. Len, Z. Chen, W. Zhu, W. Zhao, Y. Dai, L. Cao and H. Geng, *J. Colloid Interface Sci.*, 2024, **656**, 252–261.

121 F. Zheng, W. Zhong, Q. Deng, Q. Pan, X. Ou, Y. Liu, X. Xiong, C. Yang, Y. Chen and M. Liu, *Chem. Eng. J.*, 2019, **357**, 226–236.

122 M. Liu, J. Zhang, S. Guo, B. Wang, Y. Shen, X. Ai, H. Yang and J. Qian, *ACS Appl. Mater. Interfaces*, 2020, **12**, 17620–17627.

123 C. Wu, S. X. Dou and Y. Yu, *Small*, 2018, **14**, e1703671.

124 J. Guo, Z. Gu, M. Du, X. Zhao, X. Wang and X. Wu, *Mater. Today*, 2023, **66**, 221–244.

125 G. Dong, Z. Yang, B. Gao, Z. Zhu, T. Zhou, L. Tao and W. Dong, *J. Colloid Interface Sci.*, 2025, **695**, 137722.

126 L. Wang, J. Światowska, S. Dai, M. Cao, Z. Zhong, Y. Shen and M. Wang, *Mater. Today Energy*, 2019, **11**, 46–60.

127 K. S. Hong, D. H. Nam, S. J. Lim, D. Sohn, T. H. Kim and H. Kwon, *ACS Appl. Mater. Interfaces*, 2015, **7**, 17264–17271.

128 M. Duan, Y. Meng, M. Xiao, W. H. Z. Ahmed, X. Wang, H. Gao, Y. Zhang and F. Zhu, *J. Electroanal. Chem.*, 2021, **899**, 115681.

129 X. Hu, M. Wang, R. Hu, L. Yang, Q. Li, Z. Yang, J. Yang, Q. Duan, J. Chen, B. Yu, B. Guo, Z. Ma, Y. Huang and X. Li, *J. Energy Storage*, 2024, **99**, 113245.

130 P. Wang, S. Sun, Y. Jiang, Q. Cai, Y. H. Zhang, L. Zhou, S. Fang, J. Liu and Y. Yu, *ACS Nano*, 2020, **14**, 15577–15586.

131 A. Roy, S. Dey and G. Singh, *ACS Omega*, 2024, **9**, 24933–24947.

132 C. Zhao, C. Yu, M. Zhang, H. Huang, S. Li, X. Han, Z. Liu, J. Yang, W. Xiao, J. Liang, X. Sun and J. Qiu, *Adv. Energy Mater.*, 2017, **7**, 201602880.

133 W. Han, G. Liu, W. Seo, H. Lee, H. Chu and W. Yang, *Carbon*, 2021, **184**, 534–543.

134 H. Liang, H. Zhang, L. Zhao, Z. Chen, C. Huang, C. Zhang, Z. Liang, Y. Wang, X. Wang, Q. Li, X. Guo and H. Li, *Chem. Eng. J.*, 2022, **427**, 131481.

135 Y. X. Wang, S. L. Chou, D. Wexler, H. K. Liu and S. X. Dou, *Chemistry*, 2014, **20**, 9607–9612.

136 J. Li, Y. Sun, X. Zhang, Y. Sun and J. Guo, *J. Energy Storage*, 2023, **73**, 108932.

137 C. Wang, Z. Wang, D. Zhao, J. Ren, S. Liu, H. Tang, P. Xu, F. Gao, X. Yue, H. Yang, C. Niu, W. Chu, D. Wang, X. Liu, Z. Wang, Y. Wu and Y. Zhang, *ACS Appl. Mater. Interfaces*, 2021, **13**, 55020–55028.

138 T. Yi, H. M. K. Sari, X. Li, F. Wang, Y. Zhu, J. Hu, J. Zhang and X. Li, *Nano Energy*, 2021, **85**, 105955.

139 T. Yao, H. Wang, Y. Qin, J.-W. Shi and Y. Cheng, *Composites, Part B*, 2023, **253**, 110557.

140 X. Hu, Y. Liu, J. Li, G. Wang, J. Chen, G. Zhong, H. Zhan and Z. Wen, *Adv. Funct. Mater.*, 2019, **30**, 201907677.

141 Y. F. Yuan, W. C. Zhao, D. Zhang, M. Zhu, S. M. Yin and S. Y. Guo, *J. Alloys Compd.*, 2022, **895**, 162681.

142 H. Lim, S. Yu, W. Choi and S. O. Kim, *ACS Nano*, 2021, **15**, 7409–7420.

143 F. Zeng, L. Yang, Y. Pan, M. Xu, H. Liu, M. Yu, M. Guo and C. Yuan, *Electrochim. Acta*, 2019, **325**, 134903.

144 B. Kang, Y. Wang, X. He, Y. Wu, X. Li, C. Lin, Q. Chen, L. Zeng, M. Wei and Q. Qian, *Dalton Trans.*, 2021, **50**, 14745–14752.

145 H. Zhang, J. Cheng, L. Qiu, W. Sun, Y. Bai, H. Y. Yang and C. M. Li, *Adv. Funct. Mater.*, 2025, **10**, 202425947.

146 N. Al-Ansi, A. Salah, Q. A. Drmosh, G. D. Yang, A. Hezam, A. Al-Salihy, J. Lin, X. L. Wu, L. Zhao, J. P. Zhang, S. L. Wang and H. Z. Sun, *Small*, 2023, **19**, e2304459.

147 Y. L. Bai, Y. S. Liu, C. Ma, K. X. Wang and J. S. Chen, *ACS Nano*, 2018, **12**, 11503–11510.

148 J. Hu, J. Yuan, L. Zhao, G. Li, D. Chen, W. Han, Y. Chu, X. Cui, C. Li and Y. Zhang, *J. Alloys Compd.*, 2022, **895**, 162514.

149 W. Yang, J. Wang, C. Si, Z. Peng and Z. Zhang, *Nano Res.*, 2017, **10**, 2584–2598.

150 Y. Wang, D. Kong, S. Huang, Y. Shi, M. Ding, Y. Von Lim, T. Xu, F. Chen, X. Li and H. Y. Yang, *J. Mater. Chem. A*, 2018, **6**, 10813–10824.

151 F. Li, K. Ren, M. Hou, M. Lin, X. Yang, Y. Zhou, S. Xiong and F. Liang, *ACS Energy Lett.*, 2024, **10**, 195–204.

152 M. Chen, S. Gu, J. Li, Y. Dai, Y. He, B. Sun, T. Gao, L. Xu and G. Zhou, *Adv. Sci.*, 2025, e09997.

153 Y. Hao, Y. Cui, J. Wang, J. Hu, Q. Tang and S. Yang, *Chem. Eng. J.*, 2025, **518**, 164840.

154 G. Li, S. Sun, C. Chi, G. Ma, Q. Zhang, J. Li, H. Jin, S. Zhao, S. Wang and X. Bo, *Chem. Eng. J.*, 2025, **519**, 165176.

155 J. Liu, J. Li, Z. Yang, X. Zhao, D. Tu, W. Yang, J. Xu and Y. Yang, *Chem. Eng. J.*, 2025, **512**, 162394.

156 Y. Song, H. Cui, Y. Gan and W. Gao, *Energy Storage Mater.*, 2025, **77**, 104178.

157 Z. Wei, P. Mao, C. Liu, G. Lan, M. Ahmad, R. Zheng, Z. Wang, H. Sun and Y. Liu, *ACS Appl. Mater. Interfaces*, 2021, **13**, 58652–58664.

158 X. Ma, J. Zhao, R. Jiao, M. A. Mudassir, X. Xu, Y. Gao, Y. Liu, W. He, J. Cui and X. Zhao, *Rare Met.*, 2025, **44**, 4801–4814.

159 Y. Cui, L. Zhang, Q. Huo, J. Feng, C. Guo, M. Guo, G. Li, K. Wang and H. Chen, *J. Energy Storage*, 2025, **113**, 115688.

160 D. Yang, Q. Guan, B. Wang, D. Zhang, K. Ren, H. Zhou, X. Li, Y. Zhou, Y. Cai, P. Liu, L. Zhao, M. Hou, B. Yang, D. Xue and F. Liang, *Adv. Funct. Mater.*, 2024, **35**, 2420014.

161 H. Yin, H. Chen, N. Sun, X. Jian, A. Chen, B. Guo, L. Ji, Z. Yang, Y. Liu and B. Xu, *Chin. Chem. Lett.*, 2025, **25**, 111590.

162 Y. Zheng, Z. Zhang, C. Liu, H. Liao, Z. Li, Y. Jiang, Y. Hou, L. Sun and Y. Gao, *Chem. Eng. J.*, 2025, **510**, 161745.

163 Y. Tan, M. Yi, Z. Zhu, X. Zhang, K. Qin, J. Zhang and Z. Rongshu, *Mater. Today Commun.*, 2022, **31**, 103740.

164 T. Lu, B. Liu, F. Zeng, G. Cheng, S. Chu, M. Xie, Z. Chen and Z. Hou, *J. Energy Chem.*, 2022, **74**, 332–340.

165 J. Wang, J. Liu, R. T. Subramaniam, D. Zhang, Z. Li, H. J. Woo and B. Wang, *J. Power Sources*, 2024, **614**, 234991.

166 S. Cai, D. Deng, Y. Yuan, J. Liang, Y. Ye, H. Huang, L. Jin, Y. Zeng, G. Li, J. Weng, X. Fan, Y. Li and Q. Wu, *J. Energy Storage*, 2025, **134**, 118239.

167 T. Wang, Z. Tian, X. Hu, Q. Liu, L. Wang, W. Liu, Y. Zhou, C. Ma, X. Li and R. Li, *J. Power Sources*, 2025, **648**, 237369.

168 D. Chen, B. He, S. Jiang, X. Wang, J. Song, H. Chen, D. Xiao, Q. Zhao, Y. Meng and Y. Wang, *Chem. Eng. J.*, 2025, **510**, 161676.

169 Y. Wei, Z. Wang, P. Gao, Y. Zhu and X. Li, *J. Power Sources*, 2025, **646**, 237285.

170 X. Xu, Y. Chu, Y. Mu, X. Wei, Q. Zhang, H. Rao, H. Gu, L. Pan, M. Han, Y. Wang, L. Zeng and L. Wei, *ACS Nano*, 2025, **19**, 31395–31406.

171 Z. Yu, Q. Wang, K. Zhu, G. Wang, D. Cao and J. Yan, *Appl. Surf. Sci.*, 2024, **652**, 159294.

172 P. Gao, Q. Ru, Z. Pan, J. Zhang, W. Xu, F. C. C. Ling and L. Wei, *J. Colloid Interface Sci.*, 2021, **599**, 730–740.

173 G. Dong, H. Yu, L. Li, R. Zhang, X. Yang, K. Zhu, G. Wang and D. Cao, *J. Colloid Interface Sci.*, 2023, **647**, 395–405.

174 L. Fu, C. Kang, W. Xiong, P. Tian, S. Cao, S. Wan, H. Chen, C. Zhou and Q. Liu, *J. Colloid Interface Sci.*, 2021, **595**, 59–68.

175 B. Kang, X. Chen, L. Zeng, F. Luo, X. Li, L. Xu, M. Q. Yang, Q. Chen, M. Wei and Q. Qian, *J. Colloid Interface Sci.*, 2020, **574**, 217–228.

176 Y. Liu, Z. Lei, R. Liu, X. Li, P. Xiong, Y. Luo, Q. Chen, M. Wei, L. Zeng and Q. Qian, *Rare Met.*, 2023, **42**, 1557–1569.

177 B. Xu, D. Zhang, C. Peng, F. Liang, H. Zhao, B. Yang, D. Xue and Y. Lei, *Adv. Energy Mater.*, 2023, **13**, 2302325.

178 Y. A. Fesseha, K. K. Kuchayita, W. N. Su, C. W. Chiu and C. Cheng, *Chem. Eng. J.*, 2025, **509**, 161501.

179 Y. Jiang, M. Lian, J. Ma, Y. Long, X. Guo, Y. Sun, J. Lao and Z. Ye, *Nano Lett.*, 2025, **25**, 7241–7248.

180 H. G. Oh, S. Jang, H. R. Kim, D. Shin, J. Cho, H. Jang, J. K. Kim, I. Nam and S. K. Park, *J. Energy Chem.*, 2025, **111**, 462–473.

181 J. Song, Y. Ye, S. Cai, D. Deng, G. Li, Y. Zeng, J. Weng, X. Fan, Y. Li and Q. Wu, *J. Power Sources*, 2025, **657**, 238221.

182 Q. Sun, W. Xie, B. Zheng, Y. Xu, F. Xie, T. Tian, J. Zhao, Y. Xiao, S. Lei and B. Cheng, *J. Mater. Sci. Technol.*, 2026, **243**, 181–191.

183 H. Peng, W. Miao, J. Zeng, Z. Wang, C. Yan, G. Ma and Z. Lei, *Adv. Sci.*, 2025, **12**, e2417288.

184 K. She, Y. Huang, W. Fan, M. Yu, J. Zhang and C. Chen, *J. Colloid Interface Sci.*, 2024, **656**, 270–279.

185 B. Zhao, G. Suo, R. Mu, C. Lin, J. Li, X. Hou, X. Ye, Y. Yang and L. Zhang, *J. Colloid Interface Sci.*, 2024, **668**, 565–574.

186 P. Liu, F. Li, K. Ren, M. Hou, D. Yang, X. Yang, X. Wang, Y. Lei and F. Liang, *Nano Energy*, 2026, **148**, 111637.

187 H. L. Andersen, O. K. Al Bahri, S. Tsarev, B. Johannessen, B. Schulz, J. Liu, H. E. A. Brand, M. Christensen and N. Sharma, *Dalton Trans.*, 2018, **47**, 1251–1260.

188 Z. Yin, Y. Bu, J. Ren, S. Chen, D. Zhao, Y. Zou, S. Shen and D. Yang, *Chem. Eng. J.*, 2018, **345**, 165–173.

189 W. Zhang, L. Xing, J. Chen, H. Zhou, S. Liang, W. Huang and W. Li, *J. Alloys Compd.*, 2020, **822**, 153530.

190 S. Li, W. Zhang, Y. Cui, J. Ma, H.-J. Peng, J. Li, X. Liu, D. H. L. Ng, X. Liu and J. Lian, *J. Energy Chem.*, 2023, **78**, 115–122.

191 J. Zhou, T. Ji, S. Xu, X. Wang, J. Wang, Y. Tang, Y. Li, W. Yin, H. Ji, S. Shi and G. Yang, *Chem. – Eur. J.*, 2025, **27**, 202500589.

192 J. Xu, H. Guo, K. Huo and Y. Li, *J. Electroanal. Chem.*, 2022, **920**, 116598.

193 J. Cai, Y. Li, Z. Zhang, A. Cui, Z. Cai, Q. Xie and J. Wang, *J. Power Sources*, 2025, **638**, 236572.

194 B. Pati, P. K. Samal, J. Panigrahy, S. Praharaj and D. Rout, *J. Energy Storage*, 2026, **141**, 119187.

195 Y. Zhang, X. Wang, C. Shi, B. Han, C. Zhou, G. Wang, J. Li, R. Sun and K. Amine, *ACS Nano*, 2025, **19**, 27270–27279.

196 B. Wang, E. H. Ang, Y. Yang, Y. Zhang, H. Geng, M. Ye and C. C. Li, *Adv. Funct. Mater.*, 2020, **30**, 202001708.

197 C. Yang, Q. Xiang, X. Li, Y. Xu, X. Wang, X. Xie, C. Li, H. Wang and L. Wang, *J. Mater. Sci.*, 2020, **55**, 12053–12064.

198 L. Yu, X. Tao, D. Sun, L. Zhang, C. Wei, L. Han, Z. Sun, Q. Zhao, H. Jin and G. Zhu, *Adv. Funct. Mater.*, 2024, **34**, 202311471.

199 F. J. García-García, J. Mosa, A. R. González-Elipe and M. Aparicio, *Electrochim. Acta*, 2019, **321**, 134669.

200 A. Zimmer, M. Tresse, N. Stein, D. Horwat and C. Boulanger, *Electrochim. Acta*, 2020, **360**, 136931.

201 Z. Zhang, X. Zhao and J. Li, *ChemNanoMat*, 2016, **2**, 196–200.

202 S. Li, H. Hou, Z. Huang, H. Liao, X. Qiu and X. Ji, *Electrochim. Acta*, 2017, **245**, 949–956.

203 S. Gao, Y. He, K. Zhu, H. Yin, Z. Yang, G. Yue, J. Bai, Z. Cui, N. Wang, Q. Zhang and Y. Zhao, *Chem. Eng. J.*, 2025, **523**, 168326.

204 H. Ge, J. Liu, W. Shi, Y. Zhang and X. Wang, *Chin. Chem. Lett.*, 2025, **25**, 111972.

205 C. Xiao, C. Wei, L. Qin, H. Cao, L. Yang, W. Deng, C. Qin, J. Wang and J. Guo, *J. Energy Storage*, 2025, **124**, 116836.

206 Y. Yang, W. Hu, F. Liu, A. Li, D. Huang and R. Zou, *Chem. Eng. J.*, 2025, **521**, 166766.

207 W. Tao, J. Chen, C. Xu, S. Liu, S. Fakudze, J. Wang and C. Wang, *Small*, 2023, **19**, 202207397.

208 B. Fan, H. Fan, X. Chen, X. Gao, S. Chen, Q. Tang, W. Luo, Y. Deng, A. Hu and W. Hu, *ACS Appl. Mater. Interfaces*, 2021, **13**, 19894–19903.

209 Y. Li, R. Zhang, W. Zhou, X. Wu, H. Zhang and J. Zhang, *ACS Nano*, 2019, **13**, 5533–5540.

210 D. Sun, D. Huang, H. Wang, G.-L. Xu, X. Zhang, R. Zhang, Y. Tang, D. Abd Ei-Hady, W. Alshitari, A. Saad Al-Bogami, K. Amine and M. Shao, *Nano Energy*, 2019, **61**, 361–369.

211 S. H. Choi and Y. C. Kang, *Nanoscale*, 2015, **7**, 3965–3970.

212 B. Zhang, X. Chen, H. Zhao, H. Xie and H. Yin, *Rare Met.*, 2023, **42**, 1227–1237.

213 X. Lin, Y. Li, Z. Dong and J. Xu, *J. Energy Storage*, 2024, **92**, 112212.

214 J. Han, W. Xu, Z. Liu, Z. Gao, S. Tao, H. Min, H. Yang and J. Wang, *J. Alloys Compd.*, 2023, **957**, 170282.

215 Y. Hu, Y. Bai, X. Wu, X. Wei, K. Wang and J. Chen, *J. Alloys Compd.*, 2019, **797**, 1126–1132.

216 M. B. Sreedhara, A. L. Santhosha, A. J. Bhattacharyya and C. N. R. Rao, *J. Mater. Chem. A*, 2016, **4**, 9466–9471.

217 W. Kang, Y. Wang, D. Cao, Z. Kang and D. Sun, *J. Alloys Compd.*, 2018, **743**, 410–418.

218 W. Liu, M. Wei, L. Ji, Y. Zhang, Y. Song, J. Liao and L. Zhang, *Chem. Phys. Lett.*, 2020, **741**, 137061.

219 N. Li, Q. Zhou, J. Lin, Y. Lu, Z. Hou and Y. Qian, *J. Alloys Compd.*, 2022, **922**, 166306.

220 X. Hu, R. Zhu, B. Wang, X. Liu and H. Wang, *Small*, 2022, **18**, e2200437.

221 J. S. Cho, S. K. Park, K. M. Jeon, Y. Piao and Y. C. Kang, *Appl. Surf. Sci.*, 2018, **459**, 309–317.

222 P. A. Shinde, V. Mahamiya, M. Safarkhani, N. R. Chodankar, M. Ishii, R. Ma, A. A. Ghaferi, L. K. Shrestha and K. Ariga, *Adv. Funct. Mater.*, 2024, **34**, 202406333.

223 H. Fan, Q. Zhang, Q. Gu, Y. Li, W. Luo and H. Liu, *J. Mater. Chem. A*, 2019, **7**, 13736–13742.

224 X. Yue, J. Wang, Z. Xie, A. M. Patil, T. Yu, X. Du, Z. Wang, X. Hao, A. Abudula and G. Guan, *J. Mater. Sci.*, 2020, **55**, 14389–14400.

225 K. Wu, J. Zhan, G. Xu, C. Zhang, D. Pan and M. Wu, *Nanoscale*, 2018, **10**, 16040–16049.

226 H. Wang, H. Jiang, Y. Hu, P. Saha, Q. Cheng and C. Li, *Chem. Eng. Sci.*, 2017, **174**, 104–111.

227 X. Luo, J. Shao, P. He, K. Li and W. Zhao, *Appl. Surf. Sci.*, 2023, **607**, 154821.

228 Q. Zhao, K. Yu, S. Wang and C. Liang, *J. Alloys Compd.*, 2022, **927**, 167004.

229 H. Liu, H. Guo, B. Liu, M. Liang, Z. Lv, K. R. Adair and X. Sun, *Adv. Funct. Mater.*, 2018, **28**, 201707480.

230 H. Zhang, Z. Han, X. Li, F. Kong, S. Tao and B. Qian, *Ceram. Int.*, 2021, **47**, 26839–26846.

231 Y. Liu, N. Wang, X. Zhao, Z. Fang, X. Zhang, Y. Liu, Z. Bai, S. Dou and G. Yu, *J. Mater. Chem. A*, 2020, **8**, 2843–2850.

232 X. Li, J. Zhang, Z. Liu, C. Fu and C. Niu, *J. Alloys Compd.*, 2018, **766**, 656–662.

233 J. Wang, Y. Shao, F. Yuan, H. Sun, D. Zhang, Z. Li, S. Ramesh, H. J. Woo and B. Wang, *J. Energy Chem.*, 2023, **80**, 291–301.

234 Z. Wei, Y. Zhang, M. Li, C. Shu and D. Deng, *J. Energy Storage*, 2024, **81**, 110115.

235 H. He, Y. Man, J. Yang, J. Xie and M. Xu, *R. Soc. Open Sci.*, 2017, **4**, 170892.

236 B. Chen, H. Lu, J. Zhou, C. Ye, C. Shi, N. Zhao and S. Z. Qiao, *Adv. Energy Mater.*, 2018, **8**, 201702909.

237 X. Lu, Z. Wang, K. Liu, J. Luo, P. Wang, C. Niu, H. Wang and W. Li, *Energy Storage Mater.*, 2019, **17**, 101–110.

238 H. T. Huu, N. S. M. Viswanath, N. H. Vu, J.-W. Lee and W. B. Im, *Nano Res.*, 2021, **14**, 3977–3987.

239 G. Ali, A. J. Kiani, F. J. Iftikhar, S. A. Abbas Kazmi, M. Akbar, A. Rauf and K. Y. Chung, *ACS Appl. Energy Mater.*, 2021, **4**, 4638–4645.

240 J. Sheng, H. Zang, C. Tang, Q. An, Q. Wei, G. Zhang, L. Chen, C. Peng and L. Mai, *Nano Energy*, 2016, **24**, 130–138.

241 S. Jeong, E. Cho and W. Choi, *J. Power Sources*, 2024, **617**, 235141.

242 W. Wang, L. Hu, J. Ge, Z. Hu, H. Sun, H. Sun, H. Zhang, H. Zhu and S. Jiao, *Chem. Mater.*, 2014, **26**, 3721–3730.